

COOPERATIVE CONTROL OF MULTIPLE UNTETHERED MAGNETIC
MICROBOTS FOR PRECISION MICROMANIPULATION

by

NAHUM A. TORRES

Presented to the Faculty of the Graduate School of
The University of Texas at Arlington in Partial Fulfillment
of the Requirements
for the Degree of

DOCTOR OF PHILOSOPHY

THE UNIVERSITY OF TEXAS AT ARLINGTON

May 2016

Copyright © by Nahum A. Torres 2016

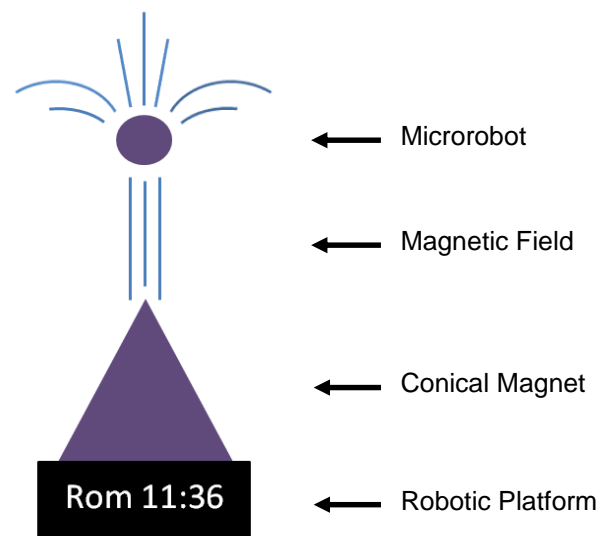
All Rights Reserved



To God "For everything comes from him and exists by his power and is intended for his glory. All glory to him forever! Amen." Romans 11:36

To my dear wife Miosotis and my kids Sebastian and Olivia

To my parents Graciela and Ignacio



Acknowledgments

I would like to thank my supervising professor Dr. Dan O. Popa for his guidance through the graduate program. I would also like to thank Dr. Frank L. Lewis, Dr. Aditya N. Das, Dr. Robert Magnusson and Dr. Kambiz Alavi for serving in my dissertation committee.

Special thanks to the University of Texas at Arlington (UTA) Department of Electrical Engineering for the opportunity to serve as a graduate teaching assistance and their administrative staff for their support, to the UTA Research Institute (UTARI) for allowing me to serve as a graduate research assistant, for providing all the tools necessary to continue my research and for supporting the microrobotics club, to Dr. Dan O. Popa, Dr. Samir Iqbal, Dr. Frank L. Lewis, Dr. Stephen Gibbs, Dr. George V. Kondraske, Dr. Kambiz Alavi, Dr. Jonathan Bredow and Dr. Carter Tiernan for their mentorship during my studies at UTA.

I am grateful to my parents and my beloved wife for the sacrifices they made and for their unconditional love and support to my success. It is to them that I dedicate my thesis.

April 8, 2016

Abstract

COOPERATIVE CONTROL OF MULTIPLE UNTETHERED MAGNETIC MICROBOTS FOR PRECISION MICROMANIPULATION

Nahum A. Torres, PhD

The University of Texas at Arlington, 2016

Supervising Professor: Dan O. Popa

The field of untethered microrobotics has emerged within the last two decades for its applications potential in military surveillance, micro and nano manufacturing, as well as in health care for minimal invasive surgery and drug delivery. Microrobots need to be fast and precise in order to be useful as a tool for manufacturing applications. It is well understood that at this size scale numerous challenges prevail such as stiction between microrobot and environment, providing power, locomotion control, and intelligence to microrobots and motion measurement. In order to accelerate the research in this field, I participated in the Mobile Microrobotics Challenge (MMC). MMC is an annual event organized by the Institute of Electrical and Electronics Engineers Robotics and Automation Society (IEEE RAS) since 2013 and designed to encourage researchers around the world to solve pressing challenges in microrobotics. The challenge is composed of three events: 1) the autonomous mobility and accuracy challenge, 2) the microassembly challenge and 3) the MMC showcase and poster session. These challenges simulate common tasks that are found in medical applications, involving high speed closed-loop positioning, and in microassembly applications involving precision motion control and the later and the showcase and poster challenge tests your communication skills.

This thesis investigates and provides methods to mitigate the problems of stiction, locomotion control, and motion measurement for microrobots. In addition, we discuss novel methods for providing cooperative behavior to multiple microrobots and to estimate and mitigate spatial uncertainty estimation for modular serial link robotic platforms. In this dissertation I describe novel methods to enhance the performance of magnetic microrobots, reduce environmental forces via inexpensive anti-friction coatings, and increase their velocities via novel mechanical amplifiers. Such methods generate swarming motions, with a leader and formation following behavior, and cooperative planar motions compatible with micromanipulation tasks such as grasping. Moreover, I provide a possible application scenario using such cooperative behavior to assemble optical elements.

The cooperative grasping behavior is produced by the magnetic field gradient controlled by a modular multi-degree of freedom serial link robot used to position the conical permanent magnet with respect to the robots' workspace. In the course of this research it was necessary to precisely characterize and compensate for the spatial uncertainty of the robot. Spatial uncertainty is an inherent feature of multiple-link robots due to misalignment of joints, link length, resolution of the actuator, the type of joint, the path of motion and the atmosphere of operation. Such uncertainties can be detrimental for robots used in assembly tasks where precision is essential. In order to overcome this fundamental challenge with flexible or modular assembly and packaging systems, I presents a novel precision evaluation and control technique to estimate and track the end-effector position errors in a robotic manipulation system resulting from the kinematic configuration as well as the dynamic parameters for each specific task; thereby, allowing the automation application to compensate for these errors in run-time.

Table of Contents

Acknowledgments	iv
Abstract	v
Chapter 1 INTRODUCTION.....	1
1.1 Motivation of Research.....	1
1.1.1 Mobile Microrobotics Challenge	2
1.1.2 Robots in Manufacturing	2
1.1.3 Trust-based Multi-Robot Control	4
1.2 Research Contributions	5
1.3 Publications	7
1.3.1 Journal Articles	7
1.3.2 Conference Articles	8
1.4 Thesis Organization.....	9
Chapter 2 BACKGROUND IN MICROROBOTICS.....	10
2.1 Micromanipulation Methods.....	10
2.2 Mobile Microrobots	12
2.3 Magnetic Mobile Microrobots using Electromagnetic Coil Actuation.....	15
2.4 Background in Manufacturing Robots	16
2.4.1 Manufacturing Robots	16
2.4.2 Spatial Uncertainty in Robotic Platforms.....	17
2.4.3 Multiple Robot Control.....	18
Chapter 3 UNTETHERED MICROROBOTS ACTUATED WITH FOCUSED PERMANENT MAGNET FIELD	19
3.1 Introduction	19
3.2 Description of Tasks	21

3.2.1 Autonomous Mobility Challenge	21
3.2.2 Microassembly Challenge	21
3.3 Description of Hardware and Software	22
3.3.1 Drive System Overview	22
3.3.2 Manipulation User Interfaces.....	23
3.3.3 Robotic Drive	24
3.3.4 Control Magnet and Magnetic Field Focusing Method	25
3.3.5 Arena Fabrication and Treatment.....	26
3.3.6 Microrobots	26
3.3.7 Vision System.....	27
3.4 Experimental Results.....	29
3.4.1 Experiment Description and Data Processing.....	29
3.4.2 Experimental Results	30
3.5 Discussion	35
3.5.1 Experimental Results	35
3.5.2 MMC 2013 Competition Results.....	36
3.6 Conclusion	37
Chapter 4 COOPERATIVE CONTROL OF MULTIPLE MICROROBOTS	38
4.1 Introduction	38
4.2 Theory of Operation.....	39
4.2.1 Artificial Potential Fields for Mobile Robots	39
4.2.2 Magnetic Field Relationship to Potential field	40
4.2.3 Potential Field Model of Conical Magnet.....	41
4.2.4 Dynamic Model.....	43
4.3 Description of Micromanipulation System	44

4.3.1 Robotic Manipulator	44
4.3.2 Microrobots and Workspace.....	46
4.4 Experimental Results.....	46
4.4.1 Conical Magnet Tilt Effect	47
4.4.2 3 Microrobot Grasping	49
4.4.3 Cooperative Micromanipulation.....	51
4.4.4 Swarm Control.....	52
4.5 Conclusion	53
Chapter 5 MICROROBOTS: MOBILITY, AUTOMATION AND COOPERATIVE	
MICROMANIPULATION	54
5.1 Introduction	54
5.2 Theory of Operation.....	56
5.3 Dynamic Model for Microrobots.....	57
5.3.1 Single Microrobot Magnetic Model	59
5.3.2 Multiple Microrobots Magnetic Model.....	60
5.4 Description of Micromanipulation System	62
5.4.1 Robotic Manipulator Overview	62
5.4.2 Microrobots and Workspace.....	64
5.5 Mobility and Path Planning	65
5.5.1.1 Single Microrobot Mobility.....	65
5.5.1.2 Single Microrobot Automated Path Detection.....	67
5.5.2 Multiple Microrobot Mobility.....	69
5.5.2.1 Multiple Microrobot Formation Orientation.....	69
5.5.2.2 Multiple Microrobot Mobility Control.....	70
5.5.2.3 Cooperative Micromanipulation	72

5.6 Micromanipulation Experimental Results	73
5.6.1 Micromanipulation with 3 cubical microrobots.....	73
5.6.2 Micromanipulation with 4 spherical microrobots	75
5.7 Conclusion	76
Chapter 6 SPATIAL UNCERTAINTY ESTIMATION FOR MODULAR SERIAL LINK ROBOTS	78
6.1 Introduction.....	78
6.2 Background.....	79
6.3 Robot Kinematics and Spatial Uncertainty Estimation	81
6.3.1 Robot Kinematics	81
6.3.2 Spatial Uncertainty Estimation	82
6.4 Spatial Uncertainty Estimation Software Tool	85
6.4.1 Software Features	85
6.4.2 Spatial Uncertainty Estimation Results	88
6.5 Experimental Results.....	93
6.5.1 Description of the Experimental Setup.....	94
6.5.2 Experimental Results	96
6.6 Discussion of Results	98
6.7 Conclusion	98
Chapter 7 CONCLUSION AND FUTURE WORK.....	100
7.1 Magnetic actuation of microrobots with focused magnetic field	100
7.2 Cooperative micromanipulation	100
7.3 Spatial Uncertainty Estimation.....	101
7.4 Future Work on Trust Based Multi-Robot Control	102
7.4.1 Introduction.....	102

7.4.2 Multiple Robot Control Background.....	103
7.4.3 Trust-Based Model for Cooperative Control.....	104
7.4.4 Trust Model for Robotic Manipulators	104
7.4.4.1 Self-Trust Model.....	105
7.4.4.2 Global Trust Model.....	106
7.4.4.3 Confidence Factor Model.....	106
7.4.5 Trust Estimation by Kalman Filter	106
7.4.6 Robot Model for Kalman Consensus.....	108
7.4.7 Conclusion.....	109
APPENDIX A IEEE RAS MOBILE MICRO/NANO-ROBOTICS CHALLENGE.....	110
A.1 Introduction.....	111
A.2 MMC 2013 Requirements	111
A.2.1 LabVIEW Interface.....	113
A.3 MMC 2014 Requirements	113
A.3.1 LabVIEW Interface.....	114
A.4 MMC 2015 Requirements	115
A.4.1 LabVIEW Interface.....	116
APPENDIX B MAGNETIC FIELD ANALYSIS WITH FEMM AND MATLAB	117
B.1 Introduction.....	118
B.2 Modeling Process within FEMM.....	118
B.3 Dynamic model MATLAB/FEMM	120
B.4 MATLAB Code for Dynamic Model	122
APPENDIX C SPATIAL UNCERTAINTY ESTIMATION LabVIEW INTERFACE.....	125
C.1 Block Diagram.....	126
C.2 Front Panel.....	128

References.....	129
Biographical Information	138

List of Illustrations

Figure 2-1. 2 mm long microrobot with a needle to puncture vasculature on a CAM [68].	11
Figure 2-2. (a) Nanofactory on a 4" wafer and (b) Nano-assembly module [4]	11
Figure 2-3. General microrobot system integration diagram	12
Figure 2-4. Mobile microrobots (a)magnetic [67], (b)magnetic piezoelectric [74], (c)magnetic resonance [75] ,(d)electromagnetic [76]	14
Figure 3-1. (a) Mobility arena and (b) assembly arena.....	21
Figure 3-2. System overview.	22
Figure 3-3. System operation block diagram	23
Figure 3-4. User interface data block diagram.....	23
Figure 3-5. Mechanical amplifier design.	24
Figure 3-6. (a) Conical magnet with 250 μm and 750 μm spheres on top of the magnet to enhance its magnetic field (b) close up of (a).	25
Figure 3-7. Magnetic field model of (a) conical magnet and (b) with stacked spheres. ...	26
Figure 3-8. (a) 250 μm Spherical microrobot and (b) 250 μm cubical microrobot.	27
Figure 3-9. (a) Arena dimensions for calibration, (b)microrobot template (c)microrobot tracking	28
Figure 3-10. Desired, motor and camera X-Y displacement (mm) vs time. Treated with PDMS and AF=1 (no mechanical amplifier).....	30
Figure 3-11. Desired, motor and camera X-Y step size (mm) vs sample #. Treated with PDMS and AF=1 (no mechanical amplifier).....	31
Figure 3-12. Motor and camera X-Y displacement trajectories (mm) vs time (mm:ss) treated with PDMS and AF=4.6	32

Figure 3-13. Motor and camera X-Y displacement step size (mm) vs sample # treated with PDMS and AF=4.6	33
Figure 3-14. Motor and camera Y displacement (mm) vs time (mm:ss) not treated with PDMS and AF=1 (no mechanical amplifier)	34
Figure 3-15. Motor and camera Y step size (mm) vs sample # not treated with PDMS and AF=1 (no mechanical amplifier)	35
Figure 4-1. (a) Conical magnet and (b) magnetic field gradient model	40
Figure 4-2. 3D Potential field and 3 microrobots model (a) and (c) and top view (b) and (d). (a) and (b) at D=0 and (c) and (d) at D=10	42
Figure 4-3. Conical magnet model (a) FEMM drawing of conical magnet and workspace and (b) FEMM output file	43
Figure 4-4. MATLAB plot of displacement trajectories of two microrobots, horizontal axis, per iteration, vertical axis	44
Figure 4-5. 5 DOF robotic manipulator (a) joint diagram and (b) actual implemented system with a 25.4 mm x 25.4 mm cone magnet	45
Figure 4-6. a) & b) Formations due to tilt, c) sides measured d) side used as base to determine the separation distance h.	48
Figure 4-7. Grasp Size for Spherical and Cubical Microrobots using 12.7mm Conical Magnet (Top) and 25.4 mm Conical Magnet (Bottom)	50
Figure 4-8. a) Micromanipulation using Spherical Microrobots, b) 500 μm and c) 250 μm Cubical Microrobots and 12.7 mm Conical Magnet	52
Figure 4-9. Swarm control of 500 μm a) spherical microrobots and b) cubical microrobots with 25.4 mm conical magnet c) swarm leader exchange	53
Figure 5-1. 25.4 mm x 25.4 mm conical magnet (a) actual magnet and (b) magnetic field density, $ B $ [T], FEMM model	56

Figure 5-2. Conical magnet enhancements FEMM magnetic field density $ B $ [T] of (a) stacked spheres (b) machined iron tip	57
Figure 5-3. FEMM model 500 μm chrome-steel spherical microrobot solution showing the magnetic field density $ B $ [T].....	59
Figure 5-4. Force of attraction of a 500 μm spherical microrobot in x-axis toward the conical magnet tip position located at 0 mm	60
Figure 5-5. FEMM model of Two 500 μm cubical microrobots with initial position at 3 mm from the center of the conical magnet	61
Figure 5-6. Two 500 μm cubical microrobots driving force as they move toward the conical magnet tip position located at 0 mm	61
Figure 5-7. Micromanipulation system block diagram	62
Figure 5-8. Modular robot manipulator (a) 3 DOF (Pz, Px, Py) configuration (b) 5 DOF (Pz, Px, Py, Rz, Ry) configuration.....	63
Figure 5-9. Four sets of double-stacked spherical microrobots grasping a 1 mm optical lens a) drawing and b) actual image	65
Figure 5-10. 250 μm spherical microrobot performing (a) “Figure 8” mobility task and (b) random path sequence 159863.....	66
Figure 5-11. Automation process (a) arena with different paths.....	68
Figure 5-12. Multiple microrobot formation orientation due to tilt	69
Figure 5-13. FEMM Model of 500 μm microrobots 1 and 2 leading and microrobot 3 trailing formation as seen from (a) x-z plane and (b) y-z plane	70
Figure 5-14. Normalized force of attraction vs distance of a 500 μm cubical microrobot in x-axis, F_x , and z-axis, F_z	71
Figure 5-15. Multiple microrobot mobility model (top view)	71
Figure 5-16. Micromanipulation grasp model (a) open grasp	72

Figure 5-17. Microassembly sequence of a 1mm optical lens with a 250 μm optical fiber using three 500 μm cubical microrobots.....	74
Figure 5-18. Optical lens trajectory during manipulation using three 500 μm cubical microrobots	74
Figure 5-19. Microassembly sequence of a 1mm optical lens with a 250 μm optical fiber using 4 sets of 2 spherical 500 μm microrobots stacked on top of each other	75
Figure 5-20. Optical lens trajectory during manipulation using four 500 μm spherical, double-stacked microrobots	76
Figure 6-1. Spatial uncertainty estimation block diagram	86
Figure 6-2. Spatial uncertainty estimation software front panel.....	87
Figure 6-3. 3 DOF robots results for translations 0 mm, 50 mm and 100 mm	89
Figure 6-4. Repeatability of a 3 DOF robot configurations vs motion.....	90
Figure 6-5. Accuracy of a 3 DOF robot configurations vs motion	90
Figure 6-6. Robot configurations: (a) (Pz,Px,Py,Rz,Ry), (b) (Px,Py,Pz,Rz,Ry), (c) (Py,Px,Pz,Rz,Ry) and (d) (Rz,Pz,Px,Py,Ry).....	91
Figure 6-7. Repeatability of a 5 DOF robot configurations vs motion	92
Figure 6-8. Accuracy of a 5 DOF robot configurations vs motion	92
Figure 6-9. 5 DOF robotic manipulation system.....	93
Figure 6-10. 500 μm cube (a) mounted at the tip of a conical endeffector and (b) 500 μm cube top view.....	94
Figure 6-11. Robot configurations used for simulation (a) (Pz,Rz,Px,Py,Ry) and (b) (Pz,Px,Py,Rz,Ry)	96
Figure 6-12. Robot configurations used for experiment (a) (Pz,Rz,Px,Py,Ry) and (b) (Pz,Px,Py,Rz,Ry)	97

Figure 7-1. Automation method a) conventional and b) trust-based 103

Figure 7-2. Cooperative task of two robotic manipulators to assemble
part "P" with end-effector "EE" 105

List of Tables

Table 3-1. Correlation of desired, motor and camera feedback with PDMS treated arena	32
Table 3-2. Correlation of desired, motor and camera feedback with mechanical amplifier with PDMS treated arena.	33
Table 3-3. Overall velocity amplification results.....	34
Table 3-4. Correlation between desired, motor and camera feedback with arena not treated with PDMS	35
Table 3-5. MMC 2013 Mobility challenge results	36
Table 3-6. MMC 2013 Assembly challenge results	37
Table 4-1. Cone tilt effect on 2 microrobots	48
Table 4-2. Conical tilt effect on 3 microrobots	49
Table 5-1. MATLAB/FEMM software interface algorithm	58
Table 5-2. Random path sequence algorithm.....	67
Table 5-3. Automated path detection algorithm.....	68
Table 6-1. Actuation mechanisms in robotics	80
Table 6-2. Types of joining mechanisms used in manipulators	80
Table 6-3. Types of manipulators kinematic configurations.....	81
Table 6-4. Database file of modules' precision specifications (mm & degrees)	88
Table 6-5. Precision specifics of the assortment of positioners used in the manipulation system.....	95
Table 6-6. Repeatability and accuracy of simulated robot.....	96
Table 6-7. Repeatability and accuracy of actual robot.....	98

Chapter 1

INTRODUCTION

1.1 Motivation of Research

The field of Microrobotics has emerged within the last two decades for its applications potential in military surveillance, micro and nano manufacturing of small industrial components, and biological samples for medical applications [1-9]. After many years of research, there is now a vast list of potential applications and high demand of microrobotics in industry and in research labs [10]. This research was focused on the industrial application of microrobots in manufacturing via assembly through micro/nano manipulation with multiple microrobots. Micro/nano manipulation refers to the physical interaction with an object at the micro or nano scales, resulting in its controlled change in position.

In prior work, researchers have proposed several methods to perform micro/nano manipulation such as:

- 1) optical tweezing where light is used to control the microrobots and/or the sample [11-14],
- 2) magnetic untethered microrobots actuated by electromagnetic coils [3, 15-21] or permanent magnets [22,23],
- 3) probe manipulators which use push, pull, or grasp using a single or multiple needles [24-27];
- 4) mechanical manipulators with two-fingered gripper capable of sensing applied force [28-30];
- 5) magnetic nano particles [8] and bacteria used as drug carriers and/or encapsulated into microrobots and actuated with magnetic resonance [7,31].

However, all the micro/nano manipulation methods aforementioned are often designed for a specific purpose and are subject to specific constraints and limitations. It is well understood that at these size scales several challenges still prevail [32,33]. The challenges to reduce stiction and provide power, locomotion control and intelligence to microrobots need to be addressed in order to achieve the level of precision beyond what the human hand can achieve and use manipulation methods effectively as a tool for manufacturing.

1.1.1 Mobile Microrobotics Challenge

In order to accelerate the research in this field, I participated in the Mobile Microrobotics Challenge (MMC). It is an annual event organized by the Institute of Electrical and Electronics Engineers Robotics and Automation Society (IEEE RAS) since 2013 designed to encourage researchers around the world to solve the current challenges in the microrobots field. The MMC consists of three events: 1) the autonomous mobility and accuracy challenge, 2) the microassembly challenge and 3) the MMC showcase and poster session. These challenges simulate common tasks that are found in medical applications, involving high speed closed-loop positioning, and in microassembly applications involving precision motion control and the later and the showcase and poster challenge tests your communication skills. Currently, the majority of successful untethered microrobots in the MMC are magnetically actuated via electromagnetic coils [15-21].

1.1.2 Robots in Manufacturing

Robots and other robotic processes are continuously transforming manufacturing and its infrastructure by aiming to improve production throughput, workspace safety and the quality of products [34, 35]. In microscale, some of the important uses of robots are in micro fabrication and assembly [10]. Recently, these technologies have been explored

using untethered mobile microrobots as seen in [36]. As these robots grow smarter, faster and more dexterous, they take on more tasks of human capabilities. One example is manufacturing microchips in which the product is complex and requires high quality production. As the concept of miniaturization of electronics continues, in this example, and the life span of products continue to shrink, manufacturing processes and its infrastructure are forced to change [37]. The short life span of products pushes robots to be adaptable to different tasks than what they were originally designed for. Such circumstances demand a flexible manufacturing infrastructure and flexible robotic systems in order for manufacturing to be able to keep up with the rate of change in production to make full use of the workspace and the robot [35].

Modular robots provide the manufacturing infrastructure with further flexibility to adapt to different production tasks [38]. A modular robotic system is a set of joints and links that can be configured by the user and can be modified to meet the current trend of assembly operation [39]. For example, a different configuration of a set of joints may be required to perform general manipulation tasks, additive manufacturing processes and even a self-reproducing platform [40-42]. However, robots experience spatial uncertainty due to misalignment of joints, link lengths, actuator resolution, controller's performance, the path of motion and operation environment.

From a control system point of view, robotic systems in micro-scale are a lot more challenging. Errors that were typically negligible in macro-scale manufacturing can no longer be ignored. In addition, integrating sensors and at micro-scale is quite challenging. Commonly, vision feedback is used as a sensor and in some cases tactile force sensing, but the resolution of such sensors may not be compatible with the precision requirements [43]. In addition, robotics at micro-scale are subject to physical interactions that are significantly different than at macro-scale. As objects become increasingly small,

surface-based forces, such as: van der Waals and electrostatic forces become more dominant, this is widely known as the scaling effect [44]. Moreover, environmental factors such as humidity and temperature can also affect the robot precision and translate into manipulation failure, especially in the case of repeated or stacked assemblies. All these factors generate a level of uncertainty in the robotic system that can be detrimental to the objective. For example, manufacturing at micro or nano scale [25,27,28,45,46] and medical surgery require very high precision for safe and effective manipulation on which the life of humans depends [47].

Researchers have studied spatial uncertainty propagation for several decades using least squares method, compounding and merging method, probability functions, joint clearances and other methods [40, 48-54]. Researchers have also proposed methods for mitigation such as probability density functions propagated using Monte Carlo simulation, interval analysis, fuzzy logic, product of exponentials, linear-quadratic Gaussian motion planning, assembly zones, and other methods that require closed-loop feedback, to estimate the nominal position, the expected error of serial link robots and the optimal path for manipulation [55-64]. However, most methods are intricate and difficult to implement thereby only using examples or simulation to illustrate the proposed method and or are designed for a specific robotic platform. In general, robot applications require a great amount of time and effort by engineers to make a robot achieve the performance that yields the desired results to manufacture a product which is affected by how the components of the robot are put together [35].

1.1.3 Trust-based Multi-Robot Control

Robotic manipulators are usually automated through the use of active feedback, typically vision, to ensure the precision needed for the implemented task. Closed-loop control methods are computationally demanding due to the amount of data being

processed and become increasingly complex as multiple robotic manipulators are working together. Cooperative control of multiple robots in traditional applications assumes that all robots are equally “trustworthy” with respect to their precision. However, this assumption can lead to large errors during manufacturing at micro and nano scale. Hence, there is need for a solution for the consensus problem of multi-robot control with trust parameters based on precision.

In this thesis, a trust-driven multi-robot control method in conjunction with a Kalman filter are used to generate a path-dependent global trust to determine the yield probability based on the goal tolerance. The method presented tracks and compensates for the spatial uncertainty of each robotic manipulator intermittently to reduce continuous visual feedback data processing.

1.2 Research Contributions

In this thesis, we describe a unique micromanipulation system, in particular its sensing and control methodology, providing methods to mitigate the problems of stiction, power, locomotion control, motion measurement, cooperative behavior to multiple microrobots and spatial uncertainty estimation for modular serial link robotic platforms. The micromanipulation system utilizes specially shaped, actuated permanent magnetic fields as the driving principle for microrobots coupled with an inexpensive coating method to control stiction, so there is less need to actuate microrobots in liquid or levitate them. This provides increased controllability over the achievable motions of the microrobots at the expense of a slight decrease in actuation speed.

However, unlike many electromagnetic coil or laser energy power transfer schemes, our system is exposed to the actuation energy through only one side or plane of the virtual cube and does not interfere with the line of sight to the microrobot. This

gives it the potential to be applied in the biomedical field for *in vivo* subcutaneous operations and in manufacturing applications at micro scale in the future.

In addition, the micromanipulation system can be used to actuate multiple such untethered microrobots simultaneously. Such method generates swarming motions, with a leader and formation following behaviors, as well as cooperative planar motions compatible with micromanipulation tasks such as grasping. We have studied a possible application scenario using such cooperative behavior to assemble optical elements to form part of an optical circuit. The cooperative grasping behavior is produced by the magnetic field gradient controlled by a modular multi-degree of freedom serial link robot used to position the conical permanent magnet with respect to the robots' workspace.

The precision achievable by our microrobots is strongly influenced by the spatial uncertainty of the robot carrying the focused magnetic field force. In order to overcome this fundamental challenge in modular robots, we present a novel precision evaluation and control technique to estimate the robot's spatial uncertainty.

Our research contributions are as follows:

1. We proposed and studied actuation of microrobots based on focused magnetic field and developed algorithms for cooperative operation of multiple of such agents with application in microassembly. The resulting manipulation system was demonstrated and validated experimentally and has the following desirable characteristics:
 - a. It is flexible and highly controllable via a multi-DOF modular robotic arm
 - b. Has high force output and manipulation precision
 - c. Is capable of creating grasping and swarming behaviors with spherical and cubical microrobots.

2. In this work, we developed algorithms to estimate the robot's spatial uncertainty. These methods are quite general, and can be extended to other robots using computationally robust libraries created. Our method was developed specifically for predicting kinematic uncertainties in serial link modular robots by expanding on the pioneering work of A.N. Das [59]. In this thesis, we completed the proof for estimating uncertainty based on approximation of the manipulator product of exponentials kinematic models and extended it to both serial and revolute joints. In addition, we validated this algorithm experimentally and in simulation. In addition, we encapsulated the spatial uncertainty in a software tool to predict positional uncertainty of a robot arm, and used these predictive models to improve the precision and control of modular robotic manipulators.
3. We expanded the uncertainty models to study the trust-based control of multiple robot manipulators collaborating to accomplish a precision manufacturing task. Our contribution was in translating a dynamic trust-based algorithm for cooperative control [65] and multi-agent Kalman consensus [66] to the problem of resource allocation in a multi-robot manufacturing cell. The algorithm uses a Kalman Filter and our uncertainty models to coordinate operation among multiple precision robots.

1.3 Publications

During the course of this research, we have authored and co-authored the following articles.

1.3.1 Journal Articles

1. N. A. Torres, A. N. Das, D. O. Popa, "Spatial Uncertainty Estimation for Modular Serial Link Robot," Submitted to *Journal of Mechanisms and Robotics*, 2015.

2. N. A. Torres and D. O. Popa, "Microrobots: Mobility, Automation and Collaborative Micromanipulation," Submitted to the *International Journal of Advanced Robotic Systems*, 2015.
3. N. A. Torres and A. N. Das, Dan Popa, F. L. Lewis "Trust-Based Multi-Robot Control," in preparation (50%) for *Transactions on Automation, Science and Engineering (T-ASE)* or *Transactions on Robotics (T-RO)*.

1.3.2 Conference Articles

1. N. A. Torres and D. O. Popa, "Cooperative Control of Multiple Untethered Magnetic Microrobots Using a Single Magnetic Field Source," in *IEEE Conference on Automation Science and Engineering*, 2015.
2. N. A. Torres, S. Ruggeri and D. O. Popa, "Untethered Microrobots actuated with Focused Permanent Magnet Field," in *ASME 2014 International Conference Design Engineering Technical Conferences and Computers and Information in Engineering Conference*, 2014.
3. N. A. Torres, et al., "Implementation of Interactive Arm Playback Behaviors of Social Robot Zeno For Autism Spectrum Disorder Therapy," in *The 5th International Conference on Pervasive Technologies Related to Assistive Environments*, 2012
4. A. N. Das, N. A. Torres, D. O. Popa, "A Flexible Manufacturing System Architecture for On-demand, Rate-independent Production," in *ASME 2015 International Mechanical engineering Congress & Exposition*, 2015.
5. D. O. Popa, N. A. Torres, and C. Lundberg, "Bringing MEMS technology Closer to Undergraduate Education via the Mobile Microrobotics Challenge," in *2013 ASEE Gulf-Southwest Annual Conference*, 2013.

6. I. Ranatunga, N. A. Torres, et al., "RoDiCA: A human-robot interaction system for treatment of childhood autism spectrum disorders," in *The 5th International Conference on Pervasive Technologies Related to Assistive Environments*, 2012.
7. N. Bugnariu, C. Young, K. Rockenbach, R. M. Patterson, C. Garver, I. Ranatunga, M. Beltran, N. A. Torres, D. Popa, "Human-robot interaction as a tool to evaluate and quantify motor imitation behavior in children with Autism Spectrum Disorders," in *The International Conference on Virtual Rehabilitation*, 2013

This work was supported in part by the NSF grant #IIS1341984, by the UT Arlington Research Institute, by a gift from L3 Communications, Ron and Lucinda Cross Foundation, The Office of Naval Research (ONR) grant N00014-06-1-1150, grant N00014-13-1-0562, grant N00014-14-1-0718 and grant N00014-11-C-0391, and by the Walmart U.S. Manufacturing Innovation Fund.

1.4 Thesis Organization

The following chapter covers the background in microrobotics systems, their application and the spatial uncertainty of robotic manipulators. Chapter 3 covers the method used to actuate microrobots for mobility and micromanipulation by pushing objects. Chapter 4 describes the method used to perform micromanipulation by grasping the object. Chapter 5 describes the mobility, automation and cooperative behavior application in microassembly of optical components. Chapter 6 describes the method to estimate the spatial uncertainty of serial link manipulators. Finally, Chapter 7 is the conclusion of the research and future work discussing the current work on trust-based control of robots using the Kalman filter as an intermittent observer to reduce the load of continuous vision feedback.

Chapter 2

BACKGROUND IN MICROROBOTICS

2.1 Micromanipulation Methods

The microrobotics field is an area of interest to research for its potential to be used in micro and nano manufacturing, as well as in health care, such as in minimal invasive surgery [1-3], biological specimen manipulation [6, 9] and drug delivery carriers for cancer treatment [7, 8], in manufacturing processes sort components before assembly [67], or in manufacturing of 3D structures [36, 45, 68-70]. After thirty years of research there is now a vast list of potential applications and high demand of microrobotics in industry and in research labs [10].

Micro/nano manipulation refers to the physical interaction with an object at the micro or nano scales, resulting in its controlled change in position. For the last 3 decades, researchers have proposed several methods to perform micro/nano manipulation such as: 1) optical tweezing where light is used to control microrobots and/or sample [11-14]; 2) magnetic untethered microrobots actuated by electromagnetic coils [3, 15-21] or permanent magnets [22, 23], 3) probe manipulators which use push, pull, or grasp using a single or multiple needles [24-27]; 4) mechanical manipulators with two-fingered gripper capable of sensing applied force [28-30]; 5) magnetic nano particles [7], and 6) bacteria used as drug carriers and/or actuated with magnetic resonance [8].

Several groups have developed systems that can perform micro/nano manipulation in 3-dimensional space (3D). The Multi-scale Robotics Lab at the Institute of Robotics and Intelligent Systems, Zurich, proposed a microrobot control system in vivo application of treatments such as eye surgery (Figure 2-1) [3]. Figure 2-1 illustrates the application on a chick choriocallantoic membrane (CAM) which serves as a viable model tissue for surgical retinal research and simulation [71].



Figure 2-1. 2 mm long microrobot with a needle to puncture vasculature on a CAM [71].

At the University of Texas at Arlington, R. Murthy and D. Popa developed a system consisting of multiple nanomanipulation modules which connected parts that were transferred mobile robots known as, ARRIPede microcrawlers, toward developing a nanofactory at wafer scale as illustrated in Figure 2-2 [4].

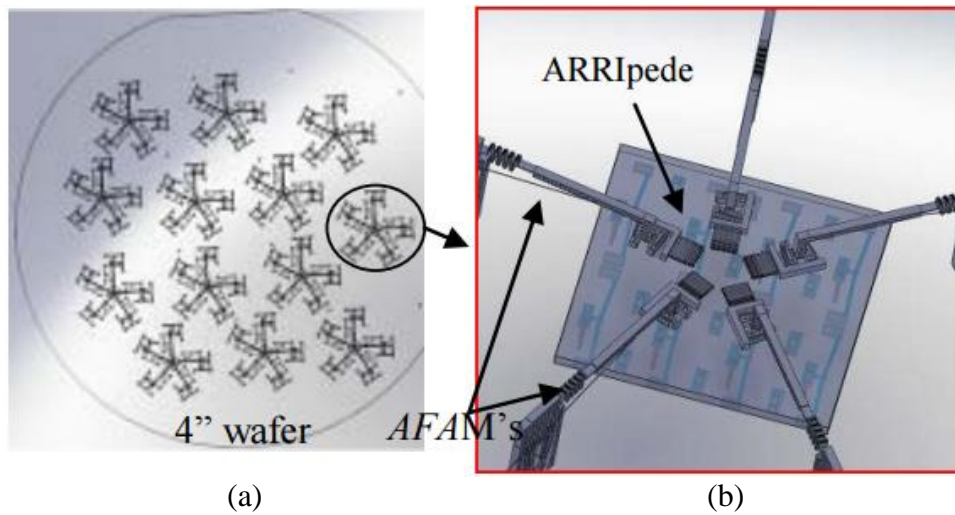


Figure 2-2. (a) Nanofactory on a 4" wafer and (b) Nano-assembly module [4]

2.2 Mobile Microrobots

Researchers around the world are working to advance the field in untethered mobile microrobots for biological cell manipulation [6], micro/nano parts transport and sorting [72]. However, this endeavor still poses many challenges that need to be overcome in order to effectively perform micromanipulation. Due to the size of the microrobots, it is difficult to embed power, control equipment and sensors. Therefore, all these requirements must be provided wirelessly. Generally, a microrobotic system is made up of several components such as: operator interface, computer, actuators, camera with microscope, sensors and data acquisition units. These components must be integrated into a platform as illustrated in Figure 2-3.

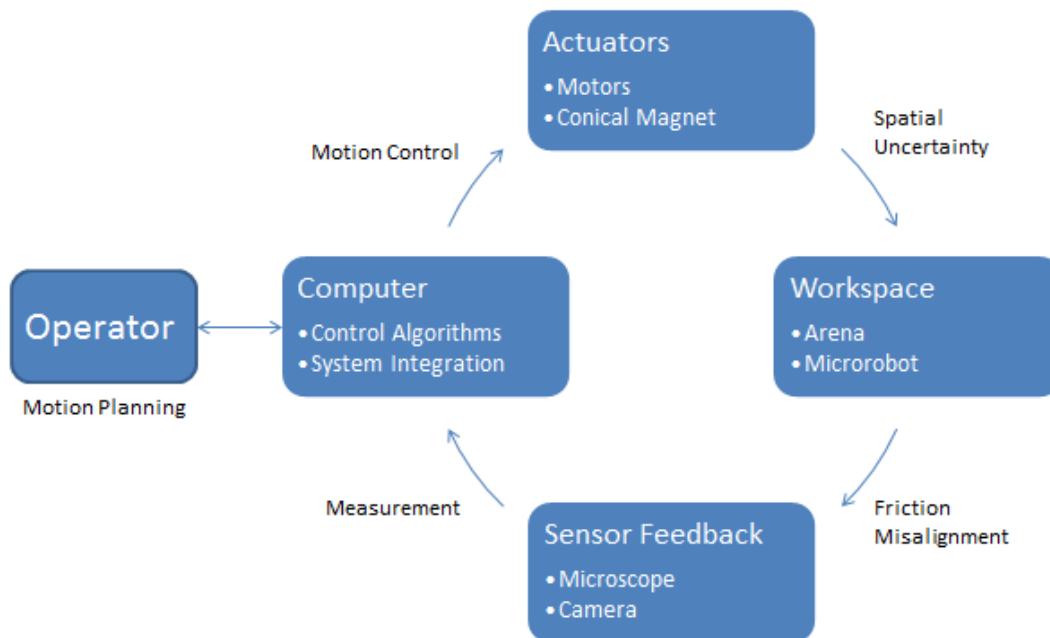


Figure 2-3. General microrobot system integration diagram

The role of the operator varies depending on the application of the system, whether it is operated in manual mode, with the operating assuming full control via an interface, in autonomous mode, in which automation is accomplished by closing the

feedback loops, or in semi-autonomous mode in which some system control algorithms assist the operator to perform the task.

In either case, a system integrator needs to be able to master all aspects of the system in order to be able to further refine and develop this technology. For every subsystem in Figure 2-3, there are challenges to overcome such as: motion control in which the operator intent needs to be transferred to the actuators of the robot, compensating for the robot's spatial uncertainty, designing the workspace to reduce misalignment and other physical interactions such as friction, and selecting appropriate sensor feedback to reduce measurements errors that pertain to its resolution and noise.

Recent advances in this technology have proposed miniature microrobots measuring approximately 2.5 mm x 2.5 mm, equipped with a micro force sensing probe measuring approximately 1.5 mm x 1.25 mm, and uses external vision to sense the force applied by the microrobot [73]. In addition to the system integration challenges, mobile microrobotics still poses difficult challenges to achieve motion resolutions in microscale and nanoscale. It is well understood that at these size scale stiction problems still prevail [32, 33]. Numerous techniques have been investigated to mitigate stiction such as tumbling locomotion, surface texturing, and special coatings [17, 32, 33, 74, 75].

Although, there are still many challenges in microrobotics, due to the promising applications of microrobotics, the National Institute of Standards and Technology (NIST) organized the microrobotics challenge in 2007 in order to accelerate the research in this field. In 2013, the IEEE Robotics and Automation Society took responsibility of the event, that continued through 2016. The MMC autonomous mobility challenge and the microassembly challenge simulate common tasks that are found in medical applications, involving high speed closed-loop positioning, and in microassembly applications involving precision motion control [76]. Since the beginning of the MMC, the event's task continue

to evolve to make the task more difficult and motivate researchers to push the envelope of microrobotics. Some of the early contestants of MMC developed mobile microrobots of different shapes as illustrated in Figure 2-4.

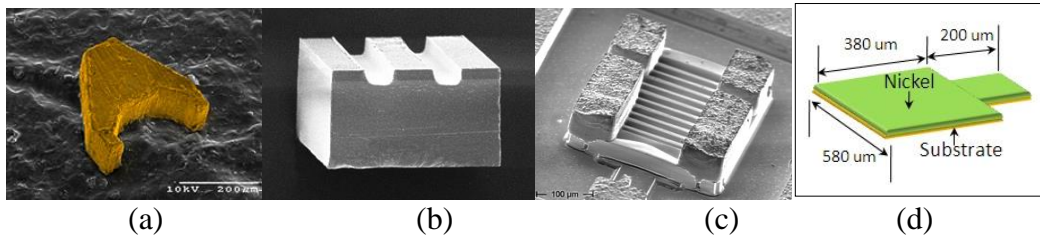


Figure 2-4. Mobile microrobots (a) magnetic [20], (b) magnetic piezoelectric [77], (c) magnetic resonance [78] ,(d) electromagnetic [21]

Untethered microrobot actuation and locomotion has been well studied by researchers that have proposed many methods such as 1) laser actuated microrobots [79], 2) magnetic microrobots actuated by electromagnetic coils [3, 15-21], 3) magnetic microrobots actuated by permanent magnets [22, 23, 46], 4) magnetic microrobots actuated with magnetic resonance [78], 5) magnetic piezoelectric [77] and 6) bacteria encapsulated into microrobots actuated with magnetic resonance [31].

The actuation methods aforementioned are frequently aimed for a specific purpose. In addition, the most successful way to actuate microrobots is through the use of electromagnetic coils which main limitation is the accessibility to the workspace. A recent survey in [80] shows considerable interest in controlling multiple microrobots for manufacturing applications. One of the problems in using multiple microrobots is that they cannot exhibit complex motion such as cooperative behavior, ideal for manufacturing, or obstacle avoidance [80]. Cooperative behavior in multiple microrobot control is important in order to achieve tasks not achievable by an individual microrobot, such as grasping, choreographed behavior in swarms and most importantly avoid collisions within themselves [81].

2.3 Magnetic Mobile Microrobots using Electromagnetic Coil Actuation

Magnetically actuated mobile microrobots using electromagnetic coils, have demonstrated to be a very successful method. Although recently, other methods of wireless powering through piezo-actuators [82], thermal [14], electrokinetic actuation [31], or laser energy [79] have emerged. A common limitation of electromagnetic coil drives is the small work space which is confined by surrounding electromagnets forming a virtual cube, while another is thermal dissipation problems due to high currents necessary to generate the magnetic field [3]. Moreover, in order for the microrobotic system to be able to be a useful tool in manufacturing, the system needs to be flexible to the different tasks and its workspace needs to be accessible in order to integrate it in the manufacturing process.

Common actuation systems for magnetic microrobots are magnetically actuated with electromagnetic coils [3, 15-21]. Such systems are usually governed by well-known expressions (1) and (2) in which the actuation force, F in (2.1), is a function of the magnetic field, B , and the magnetic dipole moment of a particle m . According to Biot-Savart Law (2.2) where μ_0 is the permeability constant, the magnetic field strength, at the point, r , is directly proportional to the current flow, I , through the coil loop, C , for each segment, dl .

$$F = \nabla(mB) \quad (2.1)$$

$$B = \frac{\mu_0}{4\pi} \int_C \frac{dl \times r}{|r|^3} \quad (2.2)$$

In order for a microrobot to perform a linear motion, it must experience a thrust force generated by a magnetic field where its gradient must occur in the plane of motion. The thrust force experienced by the microrobot also depends on the size of the robot, as the size of the robot gets smaller, the higher the magnetic field gradient required for

actuation. In turn the coils require higher power consumption which leads heating and growth of system components and complexity as seen in [19]. Furthermore electromagnetic coil systems run the risk of microrobots snapping together when controlling multiple of them if they get too close to each other [17]. Such systems can also require detailed path planning for a specific task beforehand which can be very time consuming [5]. Hence, the need for robust flexible systems that do not involve electromagnetic coils for actuation, yet comparable in performance.

2.4 Background in Manufacturing Robots

2.4.1 Manufacturing Robots

Robots and other robotic processes are continuously transforming manufacturing and its infrastructure by aiming to improve production throughput, workspace safety and the quality of products [34, 35]. As these robots grow smarter, faster and more dexterous, they take on more tasks of human capabilities forcing the manufacturing process and infrastructure to change, and to continuously shrink the life span of products [37]. The short life span of products pushes robots to be adaptable to different tasks than what they were originally designed for. Such circumstances demand for a flexible manufacturing infrastructure and flexible robotic systems in order for manufacturing to be able to keep up with the rate of change in production to make full use of the workspace and the robot [35].

Modular robots provide the manufacturing infrastructure with further flexibility to adapt to different production tasks [38]. A modular robotic system is a set of joints and links that can be configured by the user and can be modified to meet the current trend of assembly operation [39]. For example, a different configuration of a set of joints may be required to perform general manipulation tasks, additive manufacturing processes, and even a self-reproducing platform [40-42]. However, robots experience spatial uncertainty

due to misalignment of joints, link lengths, actuator resolution, controller performance, the path of motion and operation environment. Environmental factors such as humidity and temperature can also affect the robot precision and translate into manipulation failure, especially in the case of repeated or stacked assemblies. For example, manufacturing at micro or nano scale [45, 46, 83-85] and medical surgery require very high precision for safe and effective manipulation on which the life of humans depends [47].

2.4.2 Spatial Uncertainty in Robotic Platforms

The success of assembly robots depends on the precision of the mechanisms, feedback sensors used to form the robot. The precision becomes more significant when performing assembly at micro and nano scales since errors at large scale can no longer be ignored. Robot precision is generally defined by three metrics: resolution, repeatability and accuracy (RRA) [86]. Robots are systems that are composed of individual components, such as joints, links, motors, and sensors with each of these elements introducing an error in the overall manipulation task. In a fixed serial link robot the spatial uncertainty is the overall result of all the components of the robotic system.

Researchers have studied spatial uncertainty propagation for several decades using least squares method, compounding and merging method, probability functions and other methods [40, 48-53]. Researchers have also proposed methods for uncertainty mitigation such as probability density functions propagated using Monte Carlo simulation, interval analysis, fuzzy logic, linear-quadratic Gaussian motion planning and other methods that require closed-loop feedback, to estimate the nominal position, the expected error of serial link robots and the optimal path for manipulation [55-63]. However, most of these methods lack generality, and are difficult to implement. Many are validated with specific examples or simulation only, or target a specific robotic platform.

2.4.3 Multiple Robot Control

Game theory has been used in manufacturing engineering using cooperative and competitive strategies to control multiple robots [87]. In [88], game theory is used to design hybrid controllers for complex systems ideally suited for multi-agent systems. Others have used game theory to make their robots smarter due to the similarity between game theory and the independent decisions of multiple robots [89, 90].

Other methods used to control multiple robots related to trust are through the “Auction-bid” method in which each robot attempts to perform a given task, this is termed as bid. The robots that do not participate or contribute to the bid, are alienated from the team and become the untrusted members [91]. This is important since all robots do not have the same reliability or trustworthiness. However, this approach eliminates robots from being implemented. Another trust method, “Trust spreading,” is used in [92, 93]. The method deals with the trust based on the neighboring robots. However all robots are considered equal and trust themselves whereas in the trust-based control method presented in this thesis, each robot has its own spatial uncertainties, or self-trust.

Moreover, our trust-based method for multi-robot control computes the cumulative spatial uncertainty due to the robot kinematic chain configuration and joint motion precision specifications. The robots’ trust is dynamically updated using RobotTrust [65] and a Kalman consensus filter [66] is used to build a path-dependent global trust that determines the yield probability based on the designed goal tolerances. The proposed approach improves the automation throughput of complex manipulation tasks and offers a holistic manufacturing framework enabling rapid optimization of the product and production process.

Chapter 3

UNTETHERED MICROROBOTS ACTUATED WITH FOCUSED PERMANENT MAGNET FIELD

3.1 Introduction

The field of untethered Microrobotics has emerged within the last two decades for its applications potential in micro and nano manufacturing, as well as in health care, such as in minimal invasive surgery and drug delivery [1, 2]. Swimming microrobots have been proposed for in vivo treatments such as eye surgery [3], and for nanomanipulation with silicon based components [4]. It is well understood that at these size scale stiction problems still prevail [32, 33]. Numerous techniques have been investigated to mitigate stiction such as tumbling locomotion, surface texturing, and special coatings [17, 32, 33, 74, 75].

Providing power, locomotion control and intelligence to microrobots still pose many challenges. Currently, the majority of microrobots are magnetically actuated electromagnetic coils, although recently other methods of wireless powering through vibration, thermal, or laser energy have emerged [14, 31, 76, 82]. A common limitation of electromagnetic coil drives is the small work space which is confined by surrounding electromagnets forming a virtual cube, while another is thermal dissipation problems due to high currents [3].

The Mobile Microrobotics Challenge (MMC) is an annual event organized by the IEEE Robotics and Automation Society. Initially sponsored by the US NIST starting in 2007 [76, 94], the MMC is now a recurring event. The MMC consists of three events: the autonomous mobility challenge, the microassembly challenge and the MMC showcase and poster session. The automation and microassembly challenges simulate common tasks that are found in medical applications, involving high speed closed-loop positioning,

and in microassembly applications, involving precision motion control. Teams must furnish their own microrobots, which must fit within a virtual cube that is 500 μm on a side, and bring their own millimeter sized competition arenas and equipment to operate microrobots.

In this chapter we describe our unique competition system, in particular its sensing and control methodology, and present experimental results quantifying motion performance. The research contribution of our work is to utilize specially shaped, actuated permanent magnetic fields as the driving principle for our microrobots. This provides increased controllability over the achievable motions of the microrobot at the expense of a slight decrease in actuation speed. Competition results show that our system outperformed many electromagnetic coil systems in dexterity and precision, and made it intuitive to teleoperate through the interfaces provided. Furthermore, unlike many electromagnetic coil or laser energy power transfer schemes, our system is exposed to the actuation energy through only one side or plane of the virtual cube and does not require line of sight to the microrobot. In a similar fashion to the Octomag [3], this gives it the potential to be applied to in vivo subcutaneous applications in the future, but without special EM-coils. In addition, we have used a novel inexpensive coating method to control stiction, so there is less need to actuate microrobots in liquid or levitate them.

This chapter is organized as follows: in section 3.2 we describe the tasks of MMC competition, in section 3.3 we describe the system operation and all the components to include our method of enhancing the magnetic field, the mechanical amplifier used to increase speed, and the anti-stiction coatings, in section 3.4 we present experimental results quantifying the microrobot performance. Finally, section 3.5 discusses conclusions.

3.2 Description of Tasks

3.2.1 Autonomous Mobility Challenge

The mobility challenge is aimed to challenge researchers to come up with methods to provide microrobot motion control and dexterity. The arena for the autonomous challenge consists of a prescribed course that measures 2 mm x 3.5 mm and contains two walls with gates as illustrated in Figure 3-1a. Participants must place their microrobot so that the entire body rests on the left most region near gate #1, then follow a prescribed “figure 8” course autonomously. In addition, the driving and control system for the microrobot must fit under the designated competition microscope which provides a 200 mm x 200 mm x 300 mm workspace. At the 2013 event, teams were scored according to their completion time .

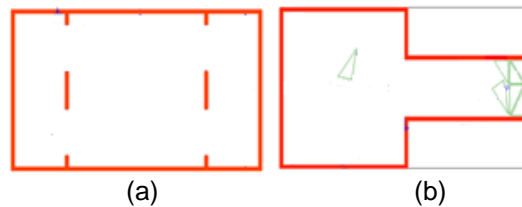


Figure 3-1. (a) Mobility arena and (b) assembly arena.

3.2.2 Microassembly Challenge

The microassembly challenge requires that the microrobot be endowed with artificial intelligence or human teleoperation for planning, locomotion, and power transmission. The arena for the Microassembly Challenge consists of a 1.5 mm x 2 mm starting region, connected to a narrow channel having dimensions of 2 mm x 0.75 mm as illustrated in Figure 3-1b. A set of triangular microfabricated components is placed on the starting region with the microrobot, and must be assembled into the far end of the channel. Triangular components must be densely packed, so that no gap between components, or between components and the channel wall, is larger than 50 μm . At the

2013 event, teams were scored according to the number of assembled triangles completed in two minutes.

3.3 Description of Hardware and Software

3.3.1 Drive System Overview

UT Arlington Microrobotics Team's competition system shown in Figure 3-2 consists of user interfaces, computer, the robotic positioning platform, and microrobots.

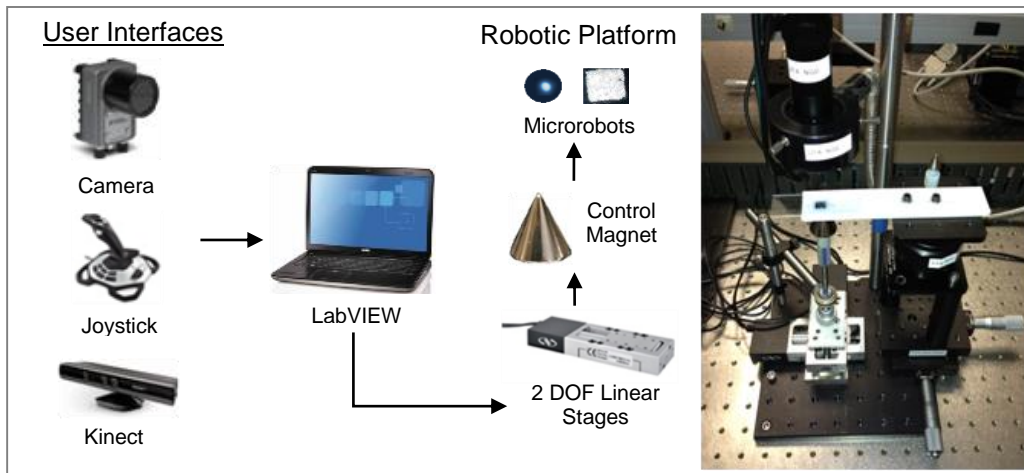


Figure 3-2. System overview.

Motion is attained via a 2 DOF robotic positioner, composed of two linear stages from Newport Corporation, model MFA-CC series, with a maximum velocity of 2.5 mm/sec. The stages control the position of a conical Neodymium permanent magnet wand attached to a pendulum. This pendulum is used as a mechanical amplifier to exceed the maximum velocity of the linear stages. The permanent magnet then provides the actuation force for microrobots placed on an arena under the microscope.

A block diagram of the system is shown in Figure 3-3, and the control software was integrated using National Instruments LabVIEW. The user can select to operate in manipulation mode where the joystick or Kinect are used for manipulation or in automated mode where a predefined path can be programmed.

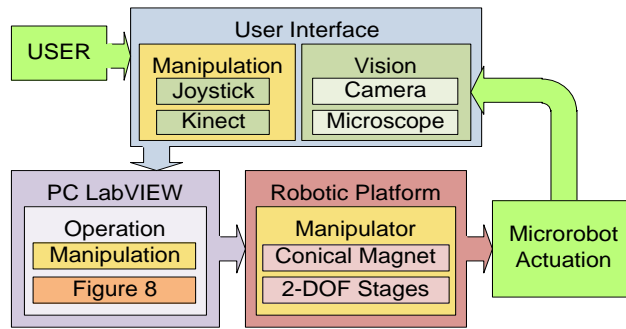


Figure 3-3. System operation block diagram

An Ethernet NI-1772C camera from National Instruments, with pixel resolution of 640x480, was combined with a suitable lens VZM 450 from Edmund Optics with a 0.35x-2.25x magnification and a working distance range of 35 mm to 175 mm. An optical fiber ring light illuminator provides diffuse illumination of the scene and cancels the effect of the environmental light.

3.3.2 Manipulation User Interfaces

The user can choose the interface to manipulate the microrobot during the microassembly challenge. The joystick or Kinect provide a step size for the relative motion of the linear stages as in Figure 3-3. The step size is scaled between 0 and 1 mm with the velocity set by the joystick displacement distance for intuitively control of the speed of the microrobot. The Kinect captures the user's position in 3D and provides the Cartesian coordinates of the body joints (Figure 3-4). The position of the wrist/hand is tracked and its (x,y) position is scaled to produce a step size to actuate the microrobot.

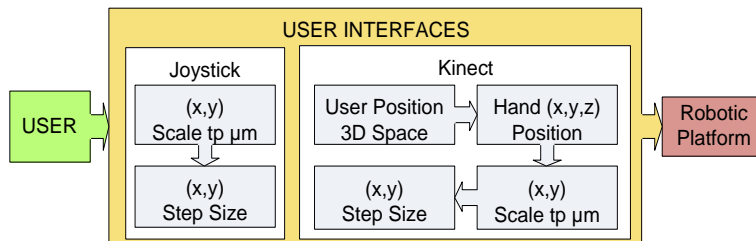


Figure 3-4. User interface data block diagram.

3.3.3 Robotic Drive

The robotic drive for microrobots consists of the competition arena suspended within 5 mm above the tip of a conical shaped permanent magnet wand, the two linear stages, and a mechanical amplifier as an inverted pendulum that is used to increase the velocity of the wand are illustrated in Figure 3-5.

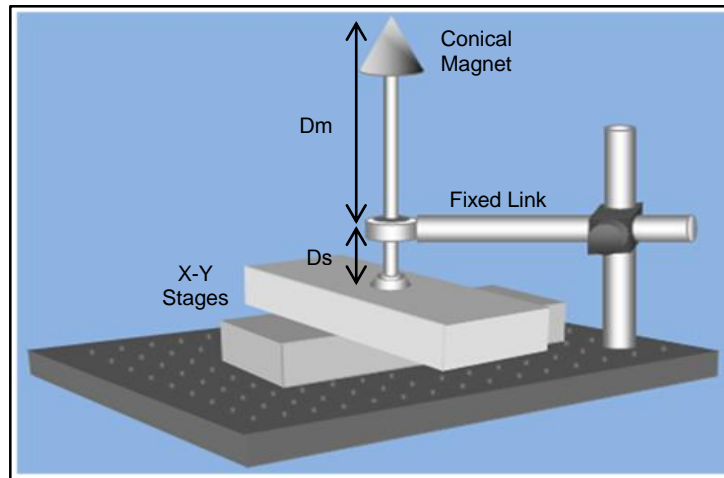


Figure 3-5. Mechanical amplifier design.

The mechanical amplifier consists of an inverted pendulum structure attached to the linear stages at the base and fixed to a ball joint. The ratio of the link placement on the pendulum allows the user to set the desired amplification and increase motion speed. For a 1:1 amplification the link is placed at the center of the pendulum. As the distance of the link to the stages decreases, the amplification constant increases. However, the amplification does not always provide a linear tip velocity increase because, at short stage displacements, the maximum velocity of the stages cannot be achieved. During experiments, we have used a maximum amplification factor (AF) of 4.6 as a result of the distance ratio between D_m the length of the pendulum link to magnetic wand tip, and D_s , the length of the pendulum link to stage:

$$AF = D_m/D_s, \quad (3.1)$$

3.3.4 Control Magnet and Magnetic Field Focusing Method

The control magnet commercially obtained from SuperMagnetMan, Inc., has a cone shape and measures 2.54 cm height x 2.54 cm diameter base with a tip size of approximately 1.5 mm. The conical shape of the magnet focuses the magnetic field at the tip of the magnet as illustrated by Yu Gu in [95]. We then use the focused magnetic field as the actuation force for the microrobot. The magnet and size create a magnetic flux density that exceeds 6000 gauss readings within 5 mm of the tip of the magnet.

Due to the brittle material of the permanent magnet, it is difficult to control the tip diameter size during manufacturing. Therefore, we proposed a clever method to sharpen the tip size by placing metallic spheres of the desired diameter on top of the magnet and subsequently a smaller sphere on top of the larger sphere as shown in Figure 3-6. This arrangement has the effect of focusing the magnetic field of the drive as shown in Figure 3-7b, while ball-bearing spheres can be commonly obtained in decreasing diameters. For best motion control results, we observed that the tip diameter size needs to be approximately the same size as the microrobot.

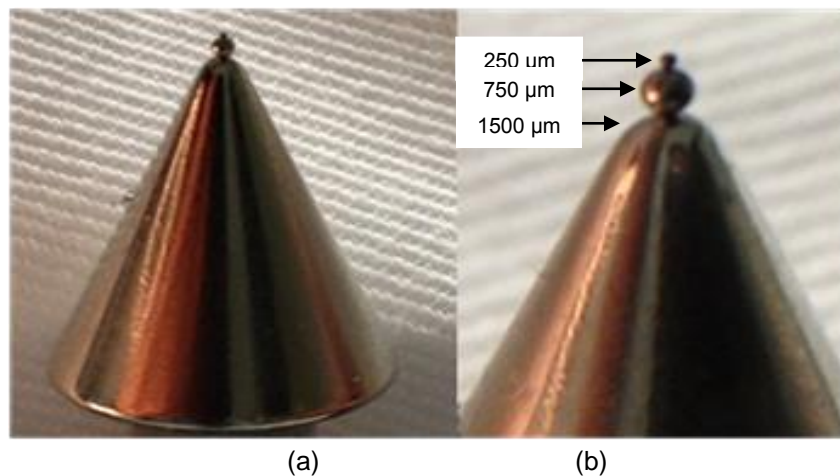


Figure 3-6. (a) Conical magnet with 250 μm and 750 μm spheres on top of the magnet to enhance its magnetic field (b) close up of (a).

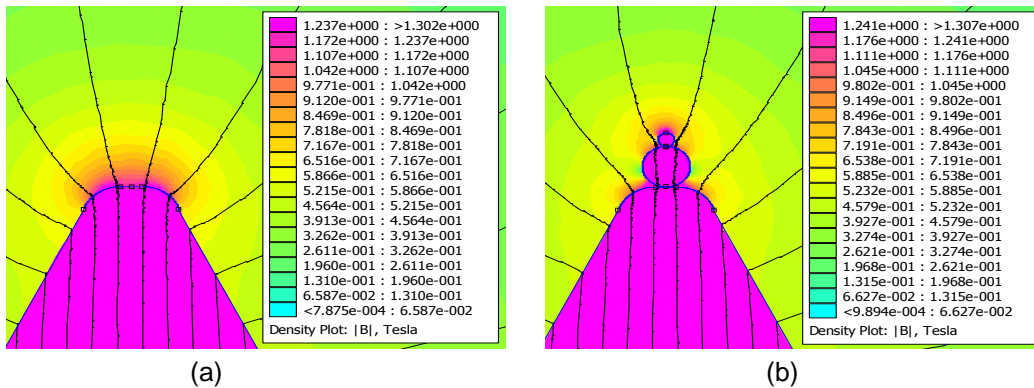


Figure 3-7. Magnetic field model of (a) conical magnet and (b) with stacked spheres.

3.3.5 Arena Fabrication and Treatment

The arenas and competition triangles are fabricated on silicon on insulator (SOI) wafers and processed with deep reactive ion etching (DRIE) to achieve a 100 μm arena depth. In order to reduce stiction between the arena and the microrobot, we spray coat it with a hydrophobic solution, known widely as Rain-X, with the primary active ingredient that consists of a hydroxy-terminated polydimethylsiloxane (PDMS) (3.2) where n is the number of the repeating monomer $\text{Si}(\text{CH}_3)_2$ [96].



The microrobots are left to dry while the arenas are dried by blowing with compressed air. After blow drying, the solution leaves behind a very thin film of PDMS not visible to the naked eye. The coating application method that we employ does not require controlled environments, is portable and inexpensive.

3.3.6 Microrobots

The microrobots used for the mobility challenge were 250 μm spheres made of chrome-steel purchased from Bal-Tec, Micro Surface Engineering Inc. illustrated in Figure 3-8a. The spherical shape was used to minimize surface contact with the arena to reduce stiction further, but Rain-X treatment of the arena was still needed. A cubical

microrobot was used for the assembly challenge. The material of this robot is Neodymium permanent magnet with an average size of 250 μm illustrated in Figure 3-8b. The approach is to have a flat surface to push an object with. The sphere could not serve the same purpose since it would roll on top of the microfabricated triangles. The drawback of the cube is that it would rotate to match the magnetic field poles to the magnetic field of the control magnet. However this was controlled by allowing the microrobot to travel some distance before engaging a microfabricated triangle leading to self-aligning to the direction of stage motion.

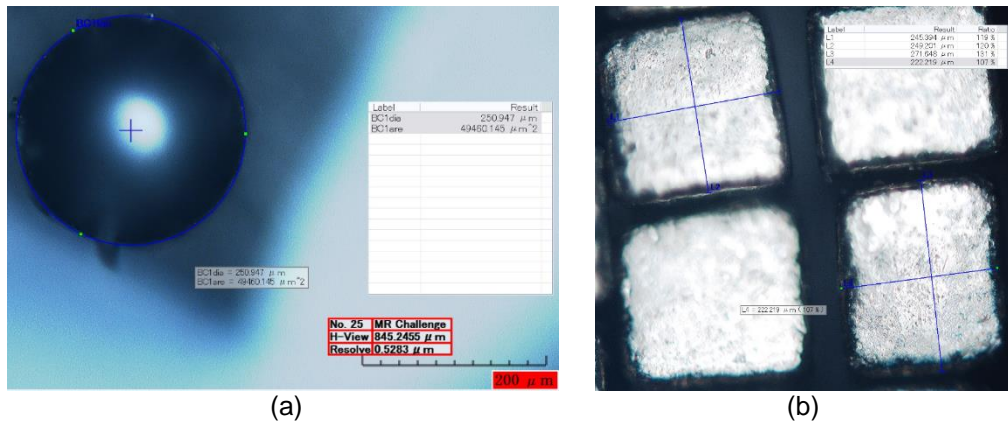


Figure 3-8. (a) 250 μm Spherical microrobot and (b) 250 μm cubical microrobot.

3.3.7 Vision System

Our system is equipped with a camera-microscope system to provide a top view of the arena and the microrobot and allow the user to close the control loop. When the adjustable FOV of the camera encloses the competition arena, a 6 $\mu\text{m}/\text{pixel}$ resolution is obtained.

A set of LabVIEW virtual instruments were conceived, developed and tested to accomplish: 2D camera calibration, continuous searching and matching of the microrobot in the arena, and the computation of the (x, y) position of the barycenter of the microrobot. The camera calibration was necessary to compute image pixel to real-world

unit (e.g. millimeters) transformation. The 2D calibration consists in acquiring a picture of a known object and comparing the planar position of some of its features measured in pixels with their known actual position expressed in real-world units. In the current setup, the highly-accurate knowledge of the dimensions of the arena obtained by microscope measurements (Figure 3-9a) made the arena a suitable calibration object. A vision algorithm able to automatically identify the borders and the corners of the arena and provide the mapping between pixels and millimeters was developed exploiting the NI LabVIEW Vision Development module.

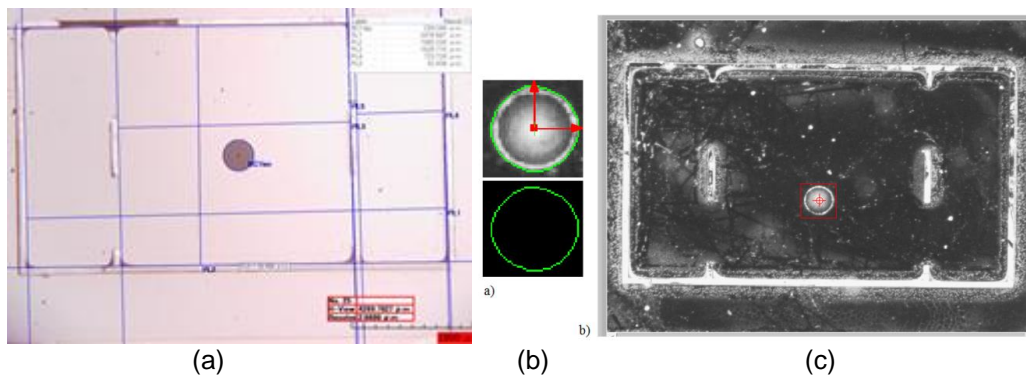


Figure 3-9. (a) Arena dimensions for calibration, (b) microrobot template
(c) microrobot tracking

Moreover, searching and matching the image of the microrobot moving on the arena were essential to provide the feedback position for the motion characterization. The adopted microrobots have a well-defined geometrical shape, therefore a geometric matching algorithm was chosen and implemented. It is based on the generalized Hough transform and searches for specific geometric features present in a template image of the target object (Figure 3-9b), even when rotated, scaled or occluded, in the current inspection image [97]. For our purpose, we created a template image of the microrobot containing specific features information. Figure 3-9b shows the template image for the spherical microrobot: in this case, the circular curve representing the projection on the

plane of the microrobot contour will be searched in the acquired image and matched. The position of the barycenter of the microrobot is extracted from the image and, thanks to the upstream calibration, recorded in millimeters. This operation runs continuously during the microrobot motion at 46 fps. In Figure 3-9c, the success of the matching operation is visually highlighted by a red bounding box and a cross overlaid on the detected barycenter of the microrobot.

3.4 Experimental Results

In this section we describe experimental results to quantify the motion performance of spherical microrobots for the Mobility Challenge. For these experiments, we command the 2 DOF stages to move in steps, and observe the effects on the microrobot camera motion. Dash stage motion increments (desired - D, and measured through the encoder - M) ΔX_M , ΔY_M , are amplified to the pendulum wand tip through the amplification factor AF, which then influences the motion of the robot in camera view creating increments ΔX_C , ΔY_C . For small, unidirectional travelling distances, the relationship between these displacements can be described by a linear image Jacobian transformation:

$$\begin{pmatrix} \Delta X_C \\ \Delta Y_C \end{pmatrix} = \begin{pmatrix} J_{11} & J_{12} \\ J_{21} & J_{22} \end{pmatrix} \begin{pmatrix} \Delta X_M \\ \Delta Y_M \end{pmatrix} \quad (3.3)$$

For larger and bi-directional motions, we expected that Equation (3.3) will no longer hold due to stiction, motion stage backlash, and nonlinearities in the wand magnetic field.

3.4.1 Experiment Description and Data Processing

Two separate tests to characterize the 100 micron dash motion of the spherical microrobot (Figure 3-8) were conducted; one with pendulum and one without pendulum, both on PDMS treated arenas. In each test we placed metallic spheres at the tip of the magnet to enhance the focused magnetic field.

An additional experiment was done on an arena without PDMS treatment to show the friction effects without PDMS coating. Similarly, the tip of the magnet was modified with different tip sizes to characterize the effect on each.

In order to compare the position of the microrobot to that of the desired position, Pearson Correlation was implemented on two sequences generated by the data acquisition algorithm. The Pearson Correlation coefficient is a measure of how well the data in your samples is linearly related. The closer to 1 or -1 the value of the samples are, the greater the linear correlation and 0 means there is no correlation [98].

3.4.2 Experimental Results

The desired position “D”, the position of the linear stages (motor) “M” and the position of the microrobot from the camera feedback “C”, were recorded and plotted over for comparison of their trajectories in 100 and 50 μm increments. Figure 3-10 is an example of the 100 μm step results and illustrates the trajectories for the x-axis and y-axis motion.

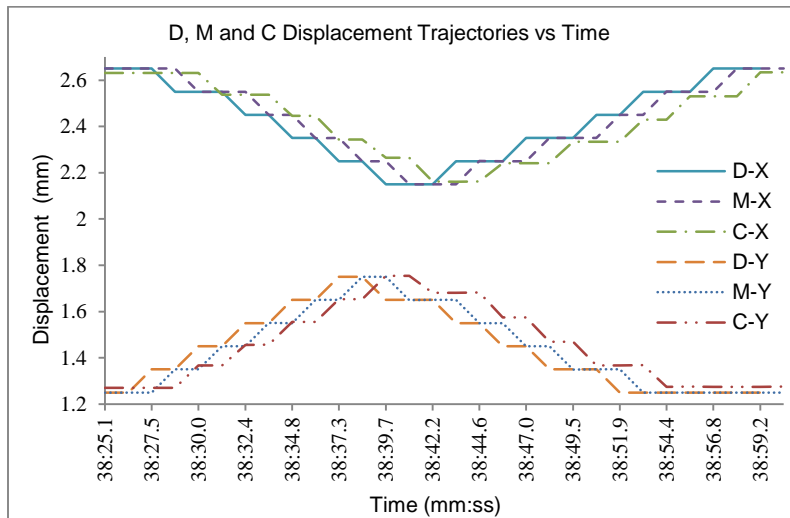


Figure 3-10. Desired, motor and camera X-Y displacement (mm) vs time. Treated with PDMS and AF=1 (no mechanical amplifier).

It is evident that the camera and the encoder signals are highly correlated when using PDMS coating. Unidirectional repeatability is especially consistent, the errors associated with image processing are not significant, and time differences are due to time delays in data acquisition and network performance within the system.

Figure 3-11 illustrates the distance travelled for each step, relative to its starting position, from Figure 3-10 for the Y axis with peak values showing the maximum distance in millimeters. The zero point indicates that the position has not changed, a position other than 0, indicates the new position's step size from previous. In Figure 3-11 the motor's and camera's feedback step size appear to be overlapping, which is a desired result. This shows that the motion of both is nearly the same.

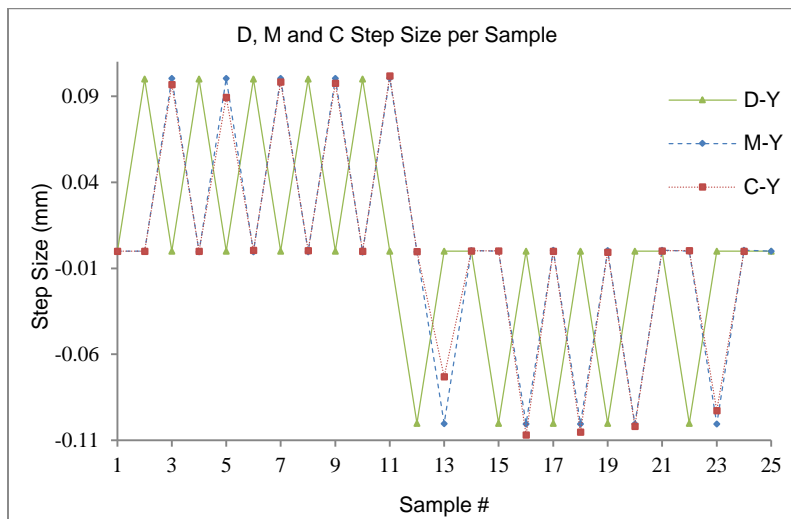


Figure 3-11. Desired, motor and camera X-Y step size (mm) vs sample #. Treated with PDMS and AF=1 (no mechanical amplifier).

The Pearson Correlation was calculated for various tip sizes of the conical magnet as well as different step sizes. The values were recorded in Table 3-1 which indicates that for higher precision, the tip of the magnet needs to be the same size as the microrobot and precision starts to fall at steps smaller than 100 μm .

Table 3-1. Correlation of desire, motor and camera feedback with PDMS treated arena

Tip Size	Step Size	Desired vs Motor		Motor vs Camera	
		X	Y	X	Y
250 μm	50 μm	0.99999	0.99998	0.96248	0.9489
250 μm	100 μm	0.99999	0.99999	0.99513	0.9953
750 μm	100 μm	0.99999	0.99999	0.99314	0.9903
1.5 mm	100 μm	0.99999	0.99999	0.90404	0.8919

The same experiment was performed with the mechanical amplifier, as shown in Figure 3-12. The motion of the tracked microrobot by the camera is smooth when using PDMS coating.

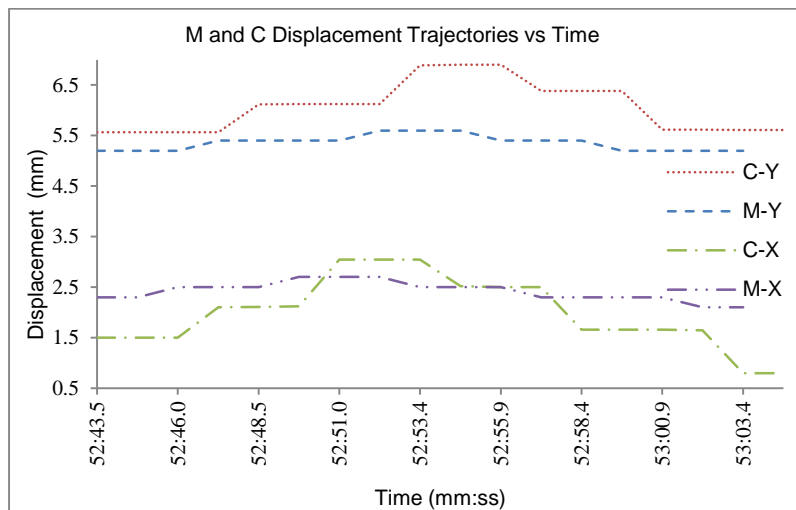


Figure 3-12. Motor and camera X-Y displacement trajectories (mm) vs time (mm:ss) treated with PDMS and AF=4.6

Figure 3-13 shows the amplification for each step from Figure 3-12 and demonstrates that the velocity amplification is around three times of the desired step size of 100 μm . Also, a non-linear amplification is observed when changing direction of motion, and travelling multiple steps.

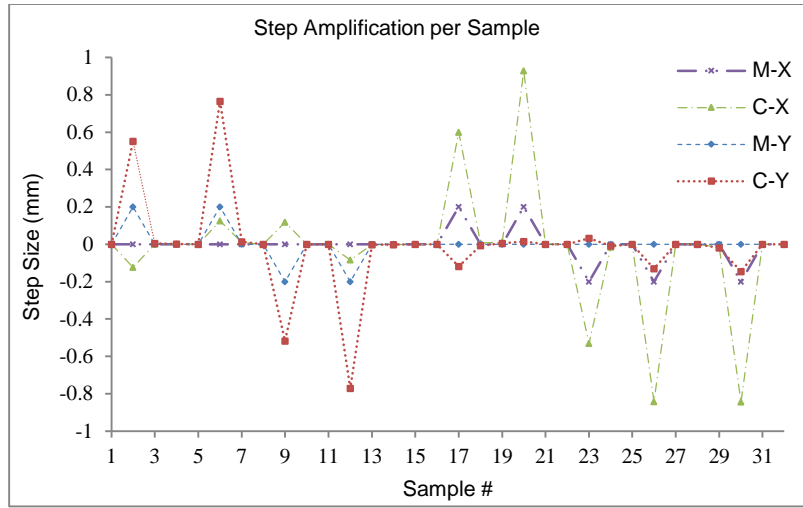


Figure 3-13. Motor and camera X-Y displacement step size (mm)
vs sample # treated with PDMS and AF=4.6

Again, the Pearson Correlation was calculated for various tip sizes of the conical magnet using the mechanical amplifier and a step size of 100 μm . The values were recorded in Table 3-2 which indicates that precision decreases when using the mechanical amplifier.

Table 3-2. Correlation of desired, motor and camera feedback
with mechanical amplifier with PDMS treated arena.

Tip Size	Step Size	Desired vs Motor		Motor vs Camera	
		X	Y	X	Y
250 μm	100 μm	0.99999	1.0000	0.94249	0.97918
750 μm	100 μm	1.00000	1.0000	0.97894	0.98409
1.5 mm	100 μm	1.00000	1.0000	0.27394	0.97141

Table 3-3 illustrates the overall velocity amplification for each motor and the camera feedback. It also shows that the 250 μm sphere has the closest VAF to the AF value of device (d). The velocity amplification factor (VAF) was calculated as in:

$$\text{VAF} = \text{Average} (\Delta\text{DC} / \Delta\text{DM}),$$

$$\Delta D_d^2 = \Delta X_d^2 + \Delta Y_d^2 \quad d = \text{C, M.} \quad (3.4)$$

Table 3-3. Overall velocity amplification results

Tip Size	Step Size	Motor & Camera		VAF
		ΔD_M	ΔD_C	
250 μm	100 μm	0.04169	0.19944	4.78303
750 μm	100 μm	0.05625	0.20392	3.62491
1500 μm	100 μm	0.04286	0.21447	5.0041

A third experiment was conducted using an arena that had not been coated with PDMS. We found that the motion of the robot is greatly hindered by stiction and can be clearly seen in Figure 3-14 where the longer steps indicate that the microrobot is moving more erratically. We can also see that the trajectory of the camera feedback is not as smooth as the previous experiments.

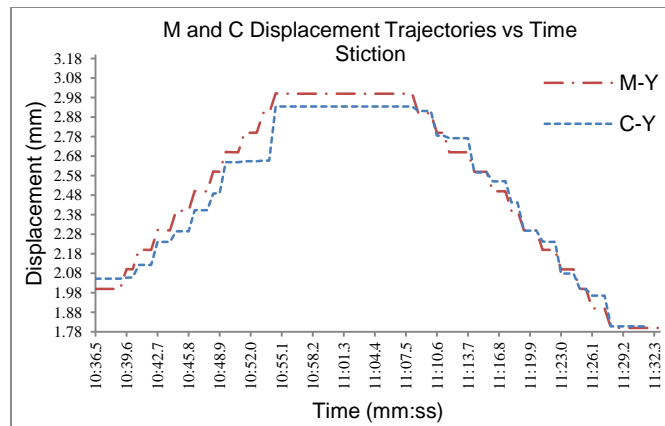


Figure 3-14. Motor and camera Y displacement (mm) vs time (mm:ss) not treated with PDMS and AF=1 (no mechanical amplifier)

In Figure 3-15, the square peaks show the motion after stiction has been overcome by the microrobot. It is desired that the motor and camera peaks overlap on top of each other as in Figure 3-11 indicating more precision in motion due to less stiction. Figure 3-15 shows that the motors move (diamond peaks), but the microrobot (square peaks) does not move by the same step size and skips some steps, therefore the samples do not overlap.

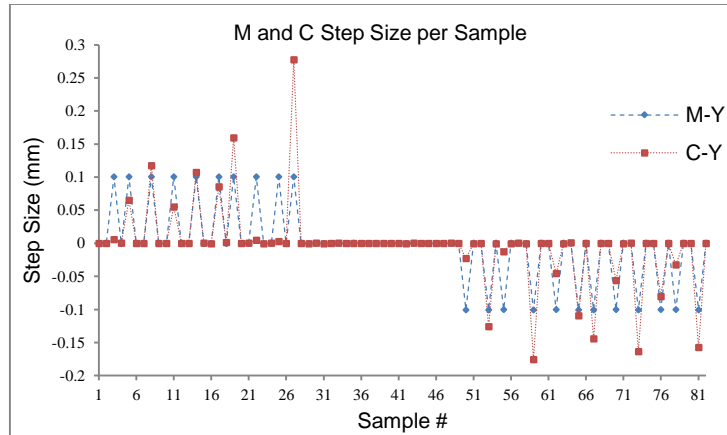


Figure 3-15. Motor and camera Y step size (mm) vs sample # not treated with PDMS and AF=1 (no mechanical amplifier)

Table 3-4 provides the correlation results from the experiments with the arena that had not been coated with PDMS. The experiment was done for different tip sizes of the control magnet. In addition it provides the percent difference compared to the results of the PDMS coated arena. The percent difference can be seen as a percent gained in precision when using PDMS.

Table 3-4. Correlation between desired, motor and camera feedback with arena not treated with PDMS

Tip Size	Step Size	D. vs M. Y	M. vs C. Y	Percent Difference
250 μm	100 μm	0.99999	0.94767	4.79%
750 μm	100 μm	1.00000	0.78354	20.88%
1500 μm	100 μm	0.99999	0.50917	42.92%

3.5 Discussion

3.5.1 Experimental Results

Table 3-1 results indicate that best precision motion in the linear regime of Equation (3.3) is achieved when the wand tip is sharpest, e.g. when the control magnet tip is approximately the same size of the microrobot. It also shows that for the 250 μm tip,

motion precision drops when the motion steps are smaller than 100 μm . Table 3-2 results indicate that precision is reduced when velocity increases via the mechanical amplifier, and some nonlinear effects are present. Table 3-3 results show that the motion of the microrobot is amplified at least by a factor of 3. Since our stages have a maximum velocity of 2.5 mm/sec, the microrobot can achieve velocities in excess of 7 mm/sec with the mechanical amplifier.

Table 3-4 results indicate that by using our method of coating the arena with PDMS, the microrobot motion precision increases significantly. For the 250 μm tip, we get a 4.78% reduction in stiction, for the 750 μm tip 20.88% and for 1500 μm tip a 42.92%. The difference in percentage is due to the difference in magnetic field flux densities at different tip sizes, creating different normal forces of the robot with the arena surface.

3.5.2 MMC 2013 Competition Results

The official competition results for the top teams are shown below. Table 3-5 shows that while our system is not as fast as some of the electromagnetic drives of other teams, it was both reliable and repeatable. The distance traveled around the “figure 8” track was about 7.5 mm and was completed in 1.338 sec, indicating that the microrobot achieved a speed of 5.6 mm/sec.

Table 3-5. MMC 2013 Mobility challenge results

Final Rank	Team	Run1 (sec)	Run2 (sec)	Run3 (sec)	RMS Score
1	U. of Waterloo, Canada	0.338	0.323	0.338	0.33
1	CMU, USA	0.338	0.354	0.369	0.35
3	UT Arlington, USA	1.385	1.338	1.338	1.35
4	LPN-CNRS, France	0.462	0.477	120	69.28

Table 3-6 shows the results of the Microassembly challenge, in which we took advantage of our microrobot controllability at the smallest AF, which matters more than speed in this event. The results show that this event is still difficult for most teams to complete.

Table 3-6. MMC 2013 Assembly challenge results

Final Rank	Team	Run 1	Run2	Run3	Score
1	LPN-CNRS France	1	2	0	1
2	Univ. of Texas Arlington, USA	0	1	1	0.6666667
3	Univ. of Alberta, Canada	0	0	1	0.3333333
3	Stevens Inst. of Technology, USA	1	0	0	0.3333333

3.6 Conclusion

In this chapter we discussed a novel method to increase the actuation precision of magnetic microrobots by focusing the magnetic field via metallic spheres placed on top of a conical permanent magnet. Precision was further enhanced by the use of a simple method to coat the work space of the microrobot with a thin film of PDMS which significantly reduces stiction. We presented experimental results demonstrating that microrobot motion is linear and repeatable at moderate speeds, and can be exploited in future automation applications. Table 3-3 results show that the use of our mechanical amplifier provides a novel solution to increase micromanipulation speed, while introducing motion nonlinearities. Results from MMC 2013 event shows that results with 2D microrobot motion are comparable with EM coil actuators, however, the drive system we employ is less complex and more intuitive to operate. Future work includes the automatic closure of the control loop on the visual feedback trajectory, microrobot motion planning, evaluation of other magnetic tip and microrobot designs, and extensions of the microrobot control in 3D.

Chapter 4

COOPERATIVE CONTROL OF MULTIPLE MICROROBOTS

4.1 Introduction

In this chapter we describe a novel magnetic untethered microrobot system and control method for multiple untethered microrobots and present experimental results to illustrate their behavior. In the previous chapter, we proposed a unique method to drive a single microrobot using a conical permanent magnet to drive microrobots measuring 250 μm . The research contribution to utilize the single conical shaped permanent magnet to actuate multiple untethered microrobots for cooperative micromanipulation and microrobot swarm control. The focused magnet is actuated by a 5 DOF robot and used as a potential field to drive the microrobots and generate cooperative behavior during swarming and micromanipulation. Due to the symmetry of the conical shaped magnet, two of the magnetic field components, (x,y) , are equal and create a circular gradient. The gradient increases (attractive potential) toward the tip of magnet and decreases away from it. Such symmetry allows control of multiple magnets without the risk of them getting too close to each other. Grasping and swarming behaviors with spherical and cubical microrobots is demonstrated and validated experimentally.

The chapter is organized as follows: in section 4.2 we describe the theory of operation of the magnetic manipulation system, in section 4.3 we describe the micromanipulation system used to experimentally validate our concepts, in section 4.4 we present experimental results illustrating the microrobots micromanipulation and swarm behavior. Finally, section 4.5 discusses conclusions.

4.2 Theory of Operation

4.2.1 Artificial Potential Fields for Mobile Robots

Artificial potential field is a concept for robot path planning which assigns a potential to every point in the workspace where the target has attractive potentials and obstacles have repulsive potentials. This concept allows the robot to navigate by following the negative gradient of the potential field containing the net force, $F(r)$, generated by the sum of the forces of the target location, $\vec{F}_{target}(r)$, and the forces of the obstacles in its path, $\vec{F}_{obs}(r)$, as in (3) where r is the distance to the target [99]:

$$\vec{F}(\vec{r}) = \vec{F}_{target}(r) + \sum_{i=1}^n \vec{F}_{obs}(r) = -\nabla V(\vec{r}) \quad (4.3)$$

For mobile robot applications with a planar workspace, the potential field and force gradient have x and y components given by [99]:

$$\nabla V(\vec{r}) = \left[\frac{\partial V}{\partial x} \quad \frac{\partial V}{\partial y} \right]^T = [F_x \quad F_y]^T \in R^2 \quad (4.4)$$

$$F_x = -\frac{\partial V(x,y)}{\partial x} \quad \text{and} \quad F_y = -\frac{\partial V(x,y)}{\partial y} \quad (4.5)$$

Mobile robots continuously create and update their trajectory in the (x,y) plane by following the trajectory of the lower potential (x_{goal}, y_{goal}) with respect to its current location where the linear attractive potential is as in (4.6) and the linear repulsive potential is as in (4.7) in which k is a gain set by the user [99].

$$V_{att}(\vec{r}) = kr = k \sqrt{(x - x_{goal})^2 + (y - y_{goal})^2} \quad (4.6)$$

$$V_{rep}(\vec{r}) = k/r = k / \sqrt{(x - x_{goal})^2 + (y - y_{goal})^2} \quad (4.7)$$

4.2.2 Magnetic Field Relationship to Potential field

A magnetic field with x,y,z components, $B(x,y,z)$ exerts a force on a particle given by (1), where the gradient is similar to the potential field in (4.4) and can be written as:

$$F = \nabla (mB(x, y, z)) \quad (4.8)$$

The magnetic flux lines of a dipole are curved in nature as shown in Figure 4-1b. This curvature creates weak, virtually absent, attractive field lines at the center and away from the tip which is an advantage for our system where we use such absence as the repulsive potential. For this application, a conical magnet was used which generates a focused magnetic field at the tip Figure 4-1a where the magnetic field is strongest within 5 mm distance from the tip. Over a certain distance the field lines begin to diverge from the center and create a gap, weak field lines, which are used as repulsive forces Figure 4-1 b. The field lines were obtained using the Finite Element Method Magnetics (FEMM) software which models magnetic objects in 2D with their respective properties [100].

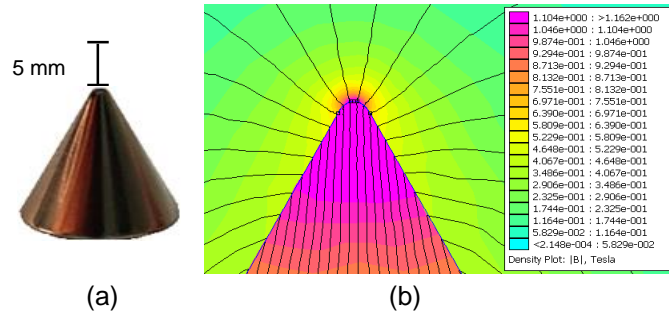


Figure 4-1. (a) Conical magnet and (b) magnetic field gradient model

The attractive potential of the conical magnet is represented as in (4.9) where x and y are the coordinate location of the robot with respect to the location of the tip of the magnet. The gradient of the magnetic field is approximated by the volume of the cone (4.10) therefore the attractive potential of the magnet is modified into (4.11). The repulsive potential is the absence of a magnetic field which is a function of the distance,

D, from tip of the magnet to the workspace of the robots (4.12). The net potential is the sum of both attractive and repulsive potentials (4.13).

$$V_{att}(\vec{r}) = kr = k \sqrt{(x - x_{tip})^2 + (y - y_{tip})^2} \quad (4.9)$$

$$Vol = \pi r^2 \frac{h_{cone}}{3} \quad (4.10)$$

$$V_{att}(\vec{r}) = kr = D\pi[(x - x_{tip})^2 + (y - y_{tip})^2] \frac{h_{cone}}{3} \quad (4.11)$$

$$V_{rep}(\vec{r}) = k/r = D/\sqrt{(x - x_{tip})^2 + (y - y_{tip})^2} \quad (4.12)$$

$$V(\vec{r}) = V_{att}(\vec{r}) + V_{rep}(\vec{r}) \quad (4.13)$$

In our case the potential field is the magnetic field of the permanent magnet and the gain k, is the distance, D, which results in the following equations

$$V(\vec{r}) = kr \leftrightarrow B(\vec{r}) = Dr \quad (4.14)$$

Therefore by controlling the distance, D, of the cone magnet normal to the workspace, we can control the magnetic field gradient which will allow us to actuate multiple microrobots for cooperative micromanipulation, grasping, and swarming.

4.2.3 Potential Field Model of Conical Magnet

The potential field was modeled by implementing Equations (4.9-4.13) using MATLAB®. The algorithm searches the minimum value of the potential field and plots a circle at that position representing our simulated robots (Figure 4-2). Since the magnet used is a cone, the potential field gradient will be circular in nature. This causes the potential field to have minimum values at different points in the (x,y) plane forming a circle around the magnet. Therefore, the initial position of the microrobots will be random. For modeling purposes, the algorithm finds the first occurrence of the minimum value, lowest potential, and places three robots equally spaced around the magnet from the location of lowest potential.

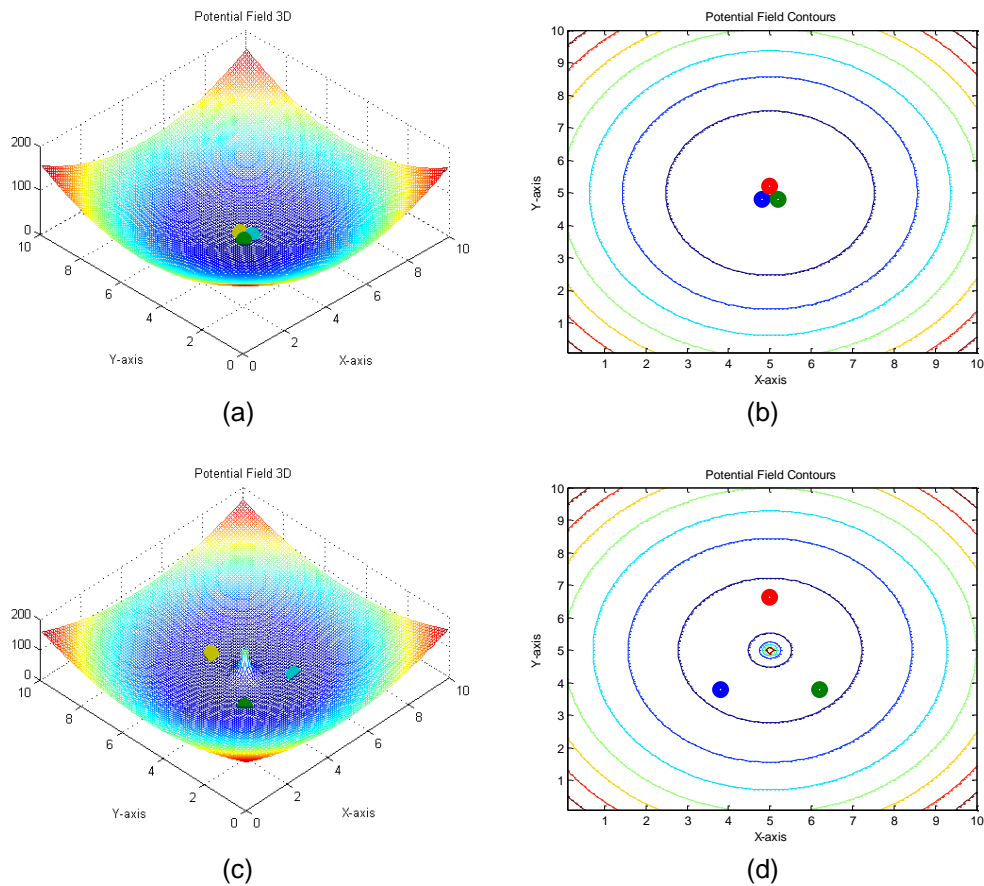


Figure 4-2. 3D Potential field and 3 microrobots model (a) and (c) and top view (b) and (d). (a) and (b) at $D=0$ and (c) and (d) at $D=10$

The conical magnet model was tested at different distance, D , values 0-10 (Figure 4-2 a-d). As the distance of the conical magnet increases, the microrobots spread apart from each other due to the absence of magnetic field creating our repulsive force at the center. When $D=0$, the three microrobots come together due to the lowest potential being the tip of the magnet. Once the object is grasped, it can be translated to a new location. These formations obtained with three microrobots will be confirmed experimentally in the next section and form the basis for a microgripper.

4.2.4 Dynamic Model

We further developed a dynamic model using MATLAB in conjunction with FEMM to solve for the position and velocity of two microrobots when exposed to a magnetic field. This model allows us to study the behavior of multiple microrobots to scale and extract the interactive forces between multiple microrobots.

We create a file in FEMM (Figure 4-3a) which contains the conical magnet and our workspace for the microrobots. A MATLAB script then opens the file and draws the initial position of the microrobots, directs FEMM to analyze the current drawing, load the solution containing the component force F_x (Figure 4-b).

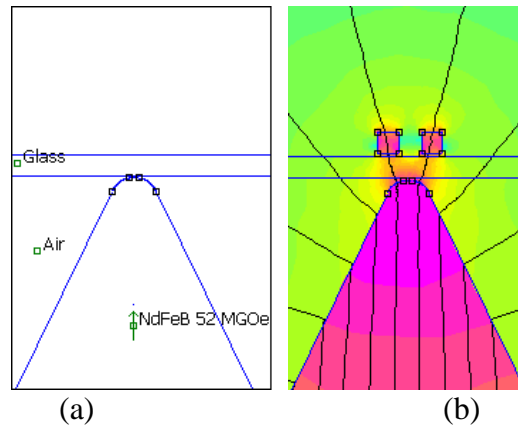


Figure 4-3. Conical magnet model (a) FEMM drawing of conical magnet and workspace and (b) FEMM output file

We then solve the dynamic Equation (4.15) in state space form (4.16) using ODE23 in MATLAB, where m is the mass of the microrobot, b is the damping coefficient and F_x is the force in the x-axis. Changing variables $x_1 = x$ and $x_2 = \dot{x}$, gives a state space model in Equation (4.15) and (4.16).

$$m\ddot{x} + b\dot{x} = F_x \quad (4.15)$$

$$\begin{bmatrix} \dot{x}_1 \\ \dot{x}_2 \end{bmatrix} = \begin{bmatrix} 0 & 1 \\ 0 & -\frac{b}{m} \end{bmatrix} \begin{bmatrix} x_1 \\ x_2 \end{bmatrix} + \begin{bmatrix} 0 \\ \frac{1}{m} \end{bmatrix} F_x \quad (4.16)$$

ODE23 provides the resultant position \dot{x}_1 and the velocity \dot{x}_2 , due to the force F_x for the next iteration. We perform sufficient iterations until the microrobots motion stops (Figure 4-4). Thus, this dynamic model allows us to predict the minimum distance that two or more microrobots can achieve in a linear formation. This result will be confirmed experimentally with formations of microrobots in the following section.

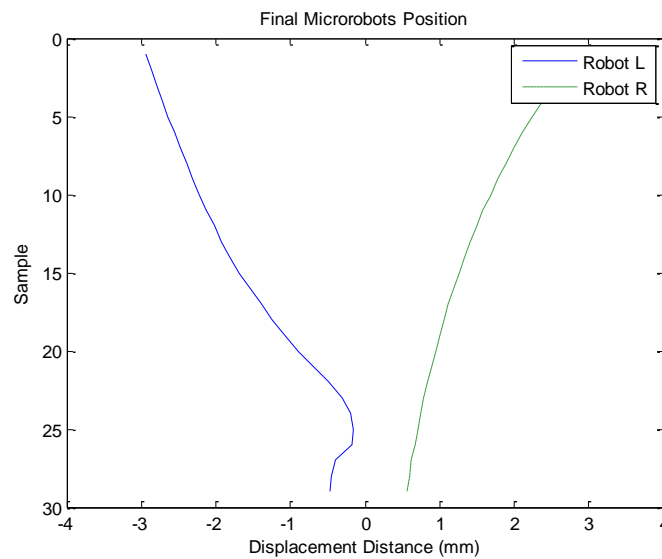


Figure 4-4. MATLAB plot of displacement trajectories of two microrobots, horizontal axis, per iteration, vertical axis

4.3 Description of Micromanipulation System

The system components include a computer with National Instruments' LabVIEW® as the user interface, a robotic manipulator, a conical magnet, a microscope and camera, microrobots and a suspended glass slide as the workspace.

4.3.1 Robotic Manipulator

The 5 DOF robotic manipulator (Figure 4-5) is composed of three prismatic joints (x, y, z) and two revolute joints (θ, ϕ) with the conical magnet as the end-effector. Two linear Zaber stages T-LSM series provide (x, y) 25 mm range of motion, a customized

linear positioner motorized with a Dynamixel MX-28 to provide the motion in z-axis at 0.5 mm per revolution. The other two revolute joints are also Dynamixel MX-28 servo motors with a 0.088° resolution which are used to control the orientation of the conical magnet which in turn controls the orientation of multiple microrobots.

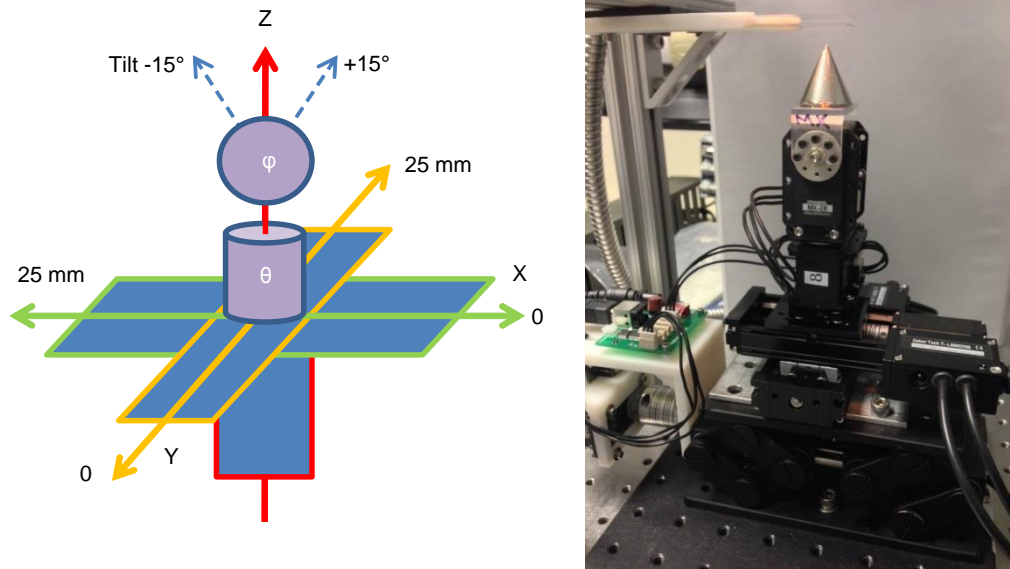


Figure 4-5. 5 DOF robotic manipulator (a) joint diagram and (b) actual implemented system with a 25.4 mm x 25.4 mm cone magnet

The conical magnets used are commercially obtained and have the following dimensions 1) 12.7 mm height x 12.7 mm diameter base with a tip size of approximately 1 mm and 2) 25.4 mm height and 25.4 mm diameter base with a tip size of about 1.5 mm. conical shape of the magnet focuses the magnetic field at the tip of the magnet which actuates the microrobots (Figure 4-3). The magnet is Neodymium of grade N50 and it can create a magnetic flux density that exceeds 6000 gauss readings within 5 mm of the tip of the magnet according to the manufacturer, Super Magnet Man.

4.3.2 *Microrobots and Workspace*

The microrobots used are 500 μm spheres made of chrome-steel purchased from Bal-Tec, Micro Surface Engineering Inc. and Cubical microrobot, Neodymium permanent magnets, measuring 250 μm and 500 μm .

The workspace is a microscope glass slide suspended above the robotic manipulator. The microrobots are then placed one at a time. The microrobots do not attract each other because their magnetic dipole orientation is oriented naturally by the conical magnet. Hence all microrobots have their magnetic dipole parallel with respect to each causing repulsion forces between them. Once the microrobots are in place we observe the workspace with an Edmund Optics camera model EO-0413M which can operate at a maximum of 87 fps with pixel resolution of 752 x 480.

4.4 Experimental Results

In this section we describe the experimental procedure to validate the potential field theory to control multiple microrobots to achieve cooperative micromanipulation and swarm behaviors. Microscope camera data was gathered using uEye Cockpit software provided by Edmund Optics which contains measurement tools. The camera image and measuring tool was calibrated using a Nomarski microscope calibration slide with 500 μm slits. The conversion factor for our experiments is 12.6761 $\mu\text{m}/\text{pixel}$. We performed system characterization using two different sizes for the conical magnet a 12.7 mm cone and a 25.4 mm cone. We used 500 μm spherical robots, 500 μm cubical robots and 250 μm cubical robots.

Specifically, we characterized the tilt effect on two and three microrobots formation and the grasp size vs. conical magnet distance from the workspace and tested the stability of the formation. The stability of the formation depends on the force of attraction experienced by each microrobot. Hence, the leader must experience a greater

force of attraction than the follower. Since the magnetic field is circular, tilting the conical magnet will expose the microrobots to different potentials and force the microrobots to form a formation along the contour of the potential field.

4.4.1 Conical Magnet Tilt Effect

First, we varied the tilt angle, ϕ , on the conical magnet from 0 to 15 degrees in increments of 5 degrees from the z-axis (Figure 4-5) and measured the separation distance. The separation distance for two microrobots is simply the distance between them and for a three microrobot formation the separation distance is h from (4.19) and illustrated in Figure 4-6d. Table I shows the separation distance of two microrobots, leader and follower due to the tilt angle of the conical magnet. Table II shows the separation distance of the formation using three microrobots. For this section of the experiment, we measured the distance center-to-center of each microrobot forming a triangle as in Figure 4-6c. Then we used well known equations to find the area and altitude, h , of a triangle. Heron's equation (4.18) is to determine the area of the triangle of sides a , b and c formed by the microrobots (Figure 4-6c). The area is used to find h (4.19), which the separation distance of the follower from the leader and the base is the perpendicular side from h (Figure 4-6d).

$$s = (a + b + c)/2 \quad (4.17)$$

$$A = \sqrt{s(s - a)(s - b)(s - c)} \quad (4.18)$$

$$h = 2A/base \quad (4.19)$$

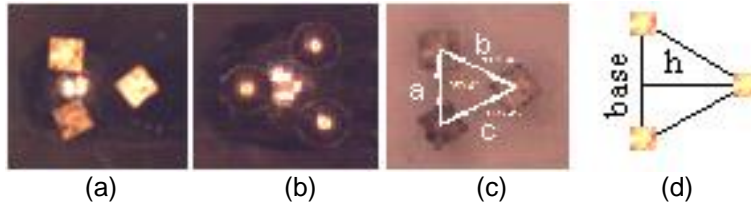


Figure 4-6. a) & b) Formations due to tilt, c) sides measured d) side used as base to determine the separation distance h .

The results on Table 4-1 show that the separation distance increases from 0-5 degrees, then decreases from 5-10 degrees for the cubical microrobots, this occurs because the conical magnet focuses the magnetic field at the tip as in Figure 4-1. Placing a microrobot on the side of the conical magnet near the tip will cause the microrobot to move towards the tip. The spherical microrobots do not experience this nonlinearity because they are not magnets; hence, the force of attraction is less than that of the cubical microrobots.

Table 4-1. Cone tilt effect on 2 microrobots

Separation Distance of 2 Microrobots (μm)			
Tilt Angle	<i>12.7 mm Cone</i>		
	500 μm Sphere	500 μm Cube	250 μm Cube
0	265.83	456.52	368.48
5	278.32	495.02	406.43
10	285.92	507.68	299.17
15	338.16	545.22	320.68
<i>25.4 mm Cone</i>			
0	287.14	418.5	304.75
5	305.01	405.64	382.18
10	311.37	380.49	317.16
15	324.04	400.85	329.82

The stability of the formation was tested by moving in the direction of the orientation of the conical magnet and back. It was observed that the spherical microrobot formation is unstable at 0° which causes the microrobots to rotate around the tip since they are exposed to the same magnetic field strength of the conical magnet. Thus friction

and dust particles cause the microrobots to rotate in the same orbit. The formation is stable for 5° and 10° only in the direction of the orientation of the conical magnet and stable in both directions at 15°. For the 250 µm and 500 µm cubical microrobots the formation is stable in both directions at 0° -10° and unstable at 15°.

The results on Table 4-2 show that both the spherical and cubical microrobots have a nonlinear separation distance as mentioned previously. The formation of three microrobots forms a triangle, when tilting the conical magnet, the formation is oriented and the stability and orientation of the formation depends on the shape of the microrobot.

Table 4-2. Conical tilt effect on 3 microrobots

Separation Distance of 3 Microrobots (µm)			
Tilt Angle	<i>12.7 mm Cone</i>		
	500µm Sphere	500µm Cube	250µm Cube
0	739.40	953.51	652.94
5	697.42	965.18	580.67
10	738.13	987.98	688.54
15	729.27	1014.04	667.13
<i>25.4 mm Cone</i>			
0	731.17	901.55	581.05
5	796.04	1044.20	554.06
10	796.06	977.00	526.13
15	791.18	1077.81	583.16

Spherical microrobots make a triangular formation where one microrobot leads the other two (Figure 4-6b). The formation is stable at 10° and 15°. The formation is unstable, rotates around the tip, at 0° and 5°. Cubical Microrobots make a triangular formation where two microrobots take the lead leaving one following (Figure 4-6a). Based on our findings, the formation is unstable at 0° and 5°. At 10° the formation is stable in both directions and at 15° the formation is only stable in the orientation of the magnet.

4.4.2 3 Microrobot Grasping

For this experiment we varied the distance, D, of the conical magnet from the workspace where D=0 the conical magnet touches the workspace and where D=10 the

magnet is 10 mm away from the workspace. We measured the three sides formed by the three microrobots from center-to-center (Figure 4-6c). Since grasping is done without tilting the magnet, the triangular formation is an equilateral triangle (Figure 4-2d). However, due to friction, all sides of the triangle vary slightly. Therefore, the grasp size is the average of all three sides.

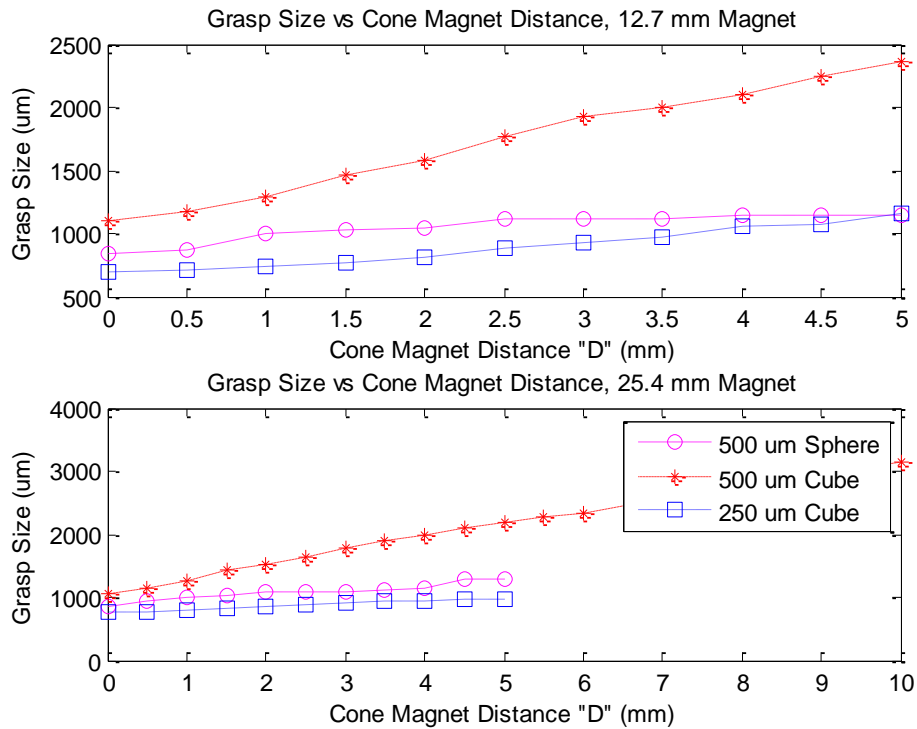


Figure 4-7. Grasp Size for Spherical and Cubical Microrobots using 12.7mm Conical Magnet (Top) and 25.4 mm Conical Magnet (Bottom)

Figure 4-7 shows the results of the grasp size using two sizes for the conical magnet and both spherical and cubical microrobots. These results show the minimum grasp size at $D=0$ and the maximum grasp size for each set of microrobots. Since the measurements were done center-to-center, the minimum grasp size is one size of the microrobot larger. From Figure 4-7 we can conclude that the optimal size of the

microrobots needed for micromanipulation is 500 μm cubical and spherical microrobots for both sizes of the conical magnet. However, the 250 μm microrobots have a better grasp using the 12.7 mm conical magnet. The reason is that using the 25.4 mm magnet increases the force of attraction downward increasing friction between the microrobot and the substrate. In addition we can observe that the 500 μm cubical robots are more responsive to the change in D.

The grasp size characterization allows us to determine the minimum (4.20) and maximum (4.21) size of the object, O , that can be successfully manipulated using the following expressions where G_0 is the grasp size at $D=0$, S is the size of the microrobots used, and G_m is the maximum achievable grasp size.

$$O_{min} = G_0 - S \quad (4.20)$$

$$O_{max} = O_{min} + G_m \quad (4.21)$$

For example the 500 μm spherical microrobot using the 12.7 mm conical magnet, the minimum size for the object of manipulation needs to be 335.97 μm and the maximum size that it can be is 642 μm .

4.4.3 Cooperative Micromanipulation

Cooperative micromanipulation (Figure 4-8) was performed using three microrobots to move a triangular object from one place to another using the following approach: opening the grasp to approach the object, closing the grasp to secure the object, tilt conical magnet for orientation, translating to move the object to the desired location, tilt back to open the grasp and move away. Once the object is placed, the microrobots release the object and move away from it. From our system characterization results, we concluded the when using cubical microrobots, the optimal tilt angle is 10° and translation velocity less than 3 mm/sec which produces a stable formation while

translating from one point to the other. However, in order to turn, a translation must occur to break away from static friction, to maintain a stable formation and hold a grip on the object.

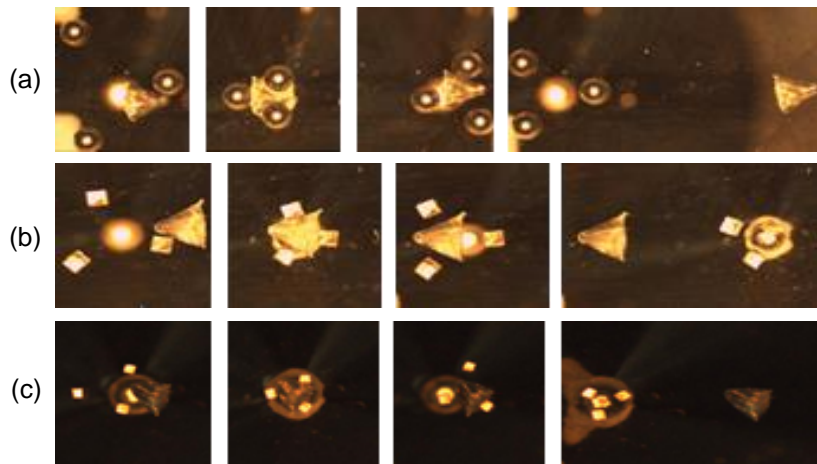


Figure 4-8. a) Micromanipulation using Spherical Microrobots, b) 500 μm and c) 250 μm

Cubical Microrobots and 12.7 mm Conical Magnet

4.4.4 Swarm Control

For the swarm control experiment we used 14 spherical microrobots and 12 cubical microrobots and varied the distance of the conical magnet, D , from 0 mm to 7 mm to illustrate the expansion and contraction of the swarm of microrobots and we also translated the swarm from left to right and vice versa to show that the using multiple microrobots hold the formation without collapsing with each other (Figure 4-9). In addition by modifying/sharpening the tip of the magnet we can select the leader of the swarm and can exchange leadership with any other microrobot (Figure 4-9c) by expanding the formation until minimal motion is noticed, we place the tip of the conical magnet under the desired microrobot, close the formation and the rest of the microrobots will surround the new leader of the formation as depicted in Figure 4-9c Left to right.

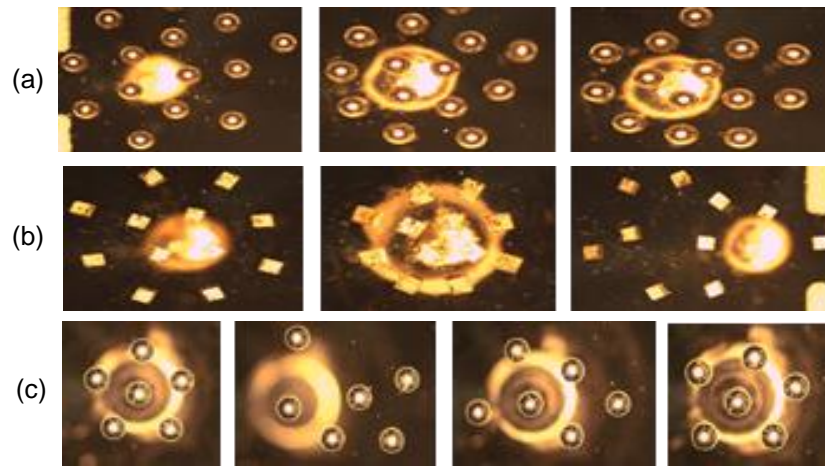


Figure 4-9. Swarm control of 500 μm a) spherical microrobots and b) cubical microrobots with 25.4 mm conical magnet c) swarm leader exchange

4.5 Conclusion

In this chapter we introduced a novel method to control multiple microrobots for cooperative micromanipulation using the potential field which is similar to the magnetic field generated by the conical magnet. We have presented different simulation models used to study the behavior of microrobot and predict stable formations.

A 5 DOF robotic manipulator was set up to study the optimal tilt angle of the conical magnet to achieve a stable formations for micromanipulation as well as to characterize the size range of the objects that can be manipulated with the system. Results show that it is possible to grasp microscopic objects, move them and release them using a “gripper” composed of three spherical and cubic microrobots. The potential for controlled swarming behavior of microrobots using our system was also validated experimentally.

Chapter 5

MICROROBOTS: MOBILITY, AUTOMATION AND COOPERATIVE MICROMANIPULATION

5.1 Introduction

Robots and robotic processes in manufacturing are essential to improve production throughput, quality of products and safe work environment [34, 35]. In microscale, some of the important uses of robots are in micro fabrication and assembly [10]. Recently, these technologies have been explored using untethered mobile microrobots as seen in [36]. The field of untethered microrobotics has been explored to perform manipulation at micro scale. However, it still poses many challenges in order to effectively perform micromanipulation for manufacturing. The most popular actuation modality for microrobots is through the use of electromagnetic coils, due to compatibility with biological environments. However, a challenge arising in implementation of this method is the limited accessibility to the microrobot workspace. Likewise for manufacturing applications, the microrobot system needs to be flexible to the different tasks and its workspace needs to be accessible for part handling and process tooling. Single microrobot actuation has been done by others using electromagnetic coils. In [15] the electromagnetic coils are placed on the x-axis and y-axis to perform planar motions of a microrobot inside a microfluidic enclosure. In [18] the system uses two pairs of Helmholtz coils using the uniform magnetic field to control a 4 mm long magnetic robot planar motion. In [19] the system contains eight electromagnetic coils surrounding the microfluidic workspace to control a single microrobot.

A recent survey in [80] shows considerable interest in controlling multiple microrobots for manufacturing applications. Such applications require microrobots to exhibit complex motions such as cooperative caging behaviors and obstacle avoidance.

Cooperative behavior is also important in order to achieve tasks such as grasping, choreographed behavior in swarms and avoid collisions with themselves [81].

Several techniques have been studied to control multiple microrobots using electromagnetic coils. The system in [68] uses a specialized workspace with a grid of MEMS-fabricated planar electromagnetic coils to generate the potential field. In [16] multiple microrobots are controlled by a global magnetic field generated by electromagnetic coils surrounding the non-specialized workspace. Control of multiple microrobots is achieved by designing each to have a unique response to the global magnetic field [16]. The work in [17] uses electromagnetic coils in conjunction with a specialized workspace with integrated electrodes to anchor microrobots electrostatically.

In this chapter discuss control of microrobots of two sizes 250 μm and 500 μm , driven by a single focused magnetic field source. The advantage of our driving system is its compact design, workspace accessibility and ease of deployment. By placing the field source on a 5 degree of freedom (DOF) robot, we expand on our previous work on single microrobot control covered in Chapter 3 and on multiple microrobot control performing cooperative behavior and swarming covered in Chapter 4. We present simulation and experimental results demonstrating mobility, automated path following and cooperative grasping and alignment of optical ball lenses with fibers, a typical micromanufacturing application.

The chapter is organized as follows, section 5.2 covers the theory of operation to control magnetic microrobots, section 5.3 covers the dynamic models, section 5.4 covers the description of the micromanipulation system, section 5.5 covers the mobility and path planning, and section 5.6 covers the experimental results of the system in microassembly of an optical lens with an optical fiber. Lastly, section 5.7 covers the conclusion.

5.2 Theory of Operation

The microrobot actuation method described in this paper is through a focused magnetic field provided by a single conical Neodymium magnet. Examples of conical magnets that will be described here include two different geometric sizes, 12.7 mm x 12.7 mm or 25.4 mm x 25.4 mm cones. The cone shape of the control magnet with vertical polarization (Figure 5-1a) focuses the magnetic field at its tip as illustrated in Figure 1 (b) visualized by a Finite Element Method Magnetics model (FEMM), a magnetic modeling software [100]. The magnetic field focused at the tip allows us to precisely control a single microrobot by simply moving the magnetic tip. However, Neodymium magnets are difficult to sharpen due to the material being brittle, resulting in a “dead zone” for microrobot motion equal to the tip radius.

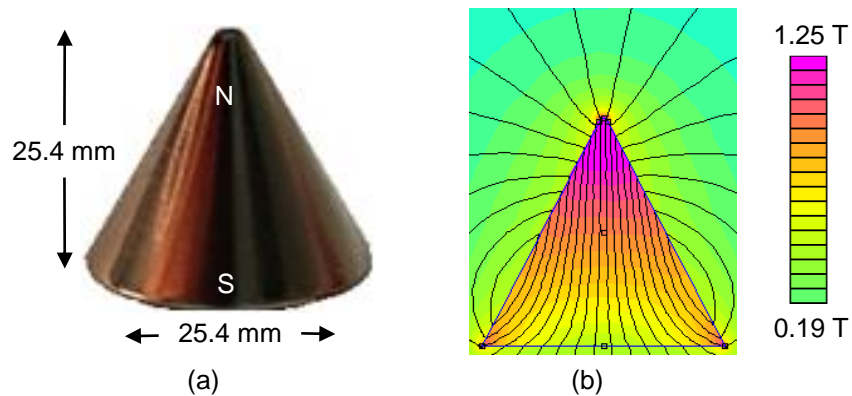


Figure 5-1. 25.4 mm x 25.4 mm conical magnet (a) actual magnet and (b) magnetic field density, $|B|$ [T], FEMM model

In Chapter 3, chrome-steel spheres were placed at the tip of the conical magnet to enhance the microrobot precision (Figure 5-2 a). The results reported in Chapter 3 showed that the positional accuracy of the microrobot improved as the sharpness of the tip of the conical magnet reached similar dimensions to the microrobot. Accuracy improved from 90% to 99.5% of motion distances of 100 μm . By contrast, in this chapter

we machined a sharp iron tip (tip size approximately 150 μm) and placed it on the conical magnet (Figure 5-2 b) to avoid having to assemble and secure spheres on the tip.

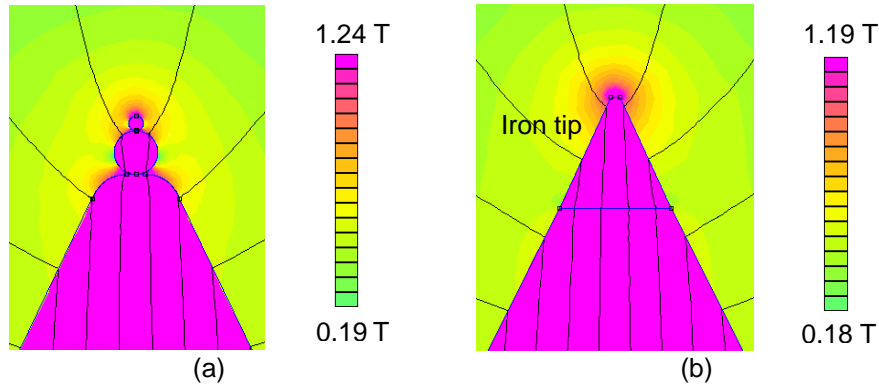


Figure 5-2. Conical magnet enhancements FEMM magnetic field density $|B|$ [T] of (a) stacked spheres (b) machined iron tip

5.3 Dynamic Model for Microrobots

In order to investigate and predict quasi-static equilibrium configurations, microrobot motion in the presence of magnetic field was approximated by a mass-damper from chapter 4. This second order system relies on the microrobot mass m , and damping coefficient b . In general m is known from the geometry and material choices, while b is unknown and depends on friction and drag coefficients in the environment. The choice of damping coefficient does not affect the static equilibrium configurations, but it will affect the microrobot transient response. In our simulations, damping coefficients were approximated to obtain stable and illustrative trajectories for microrobots.

The state space model in chapter 4 was expanded to include forces from by other microrobots which applies to multiple microrobot operations. The motion of microrobot moving along a scalar coordinate direction, can be written as in Equation (5.1), where the force of attraction, F_d , is the force of the microrobot in the x-plane, and $F_d = b \frac{dx}{dt}$ is the drag force experienced by the microrobot, F_{other} denotes the force

induced by other microrobot magnetic dipoles and F_t is the total magnetic driving force in Equation (5.2). For single microrobot operation $F_{other} = 0$.

$$m \frac{d^2x}{dt^2} = F_a + F_{other} - F_d \quad (5.1)$$

$$F_t = F_a + F_{other} \quad (5.2)$$

The state space model was numerically implemented in conjunction with MATLAB script which invokes the FEMM solver for the magnetic field source, in to study the dynamic behavior of single or multiple microrobots when exposed to the global magnetic field. The algorithm to perform the MATLAB/FEMM dynamic models of different scenarios is presented in pseudocode in Table 5-1.

Table 5-1. MATLAB/FEMM software interface algorithm

MATLAB/FEMM Interface Algorithm
1. Open FEMM software
2. Open FEMM file
3. $p0=(x,z); v0=0; \quad \% \text{ initial position and velocity}$
4. for n=1:samples
5. <i>draw microrobot</i>
6. <i>add material of microrobot</i>
7. <i>analyze in FEMM</i>
8. <i>load solution of FEMM</i>
9. <i>select area for analysis</i>
10. <i>Extract force component F_t</i>
11. <i>Reset steps 5 through 10</i>
12. $T=0.058 \text{ seconds}; IC=[p0, v0, F_t];$ <i>% Solve state space model using function Magdyn</i>
13. $[T,X]=ode23(@Magdyn,[T],IC)$
14. $P0=X(n,1); V0=X(n,2); \quad \% \text{ new position and vel.}$
15. END
16. $Plot(X(:,3)) \quad \% F_t$
1. function X = Magdyn(T, IC)
2. $b=\text{damping coefficient}; \% \text{friction}$
3. $m=\text{mass of microrobot};$
4. Solve Equation (7) % state space
5. return X = $[\dot{x}_1; \dot{x}_2; F_t];$

5.3.1 Single Microrobot Magnetic Model

A dynamic model in FEMM was set up to simulate the experimental conditions with a 500 μm chrome-steel spherical microrobot, a 500 μm thick glass slide and a 25.4 mm x 25.4 mm conical neodymium magnet as illustrated in Figure 5-3. We approximated its mass to be 4.121 mg using the density of iron of 7.87 g/cm^3 . The damping coefficient, b , was set to 0.17 in our simulation to eliminate microrobot oscillation. Figure 5-4 illustrates the microrobot's force of attraction, F_a , vs its position as it travels from its initial position, 3 mm away from the tip on the glass surface along the x-axis, to the tip of the conical magnet located at the 0 mm mark.

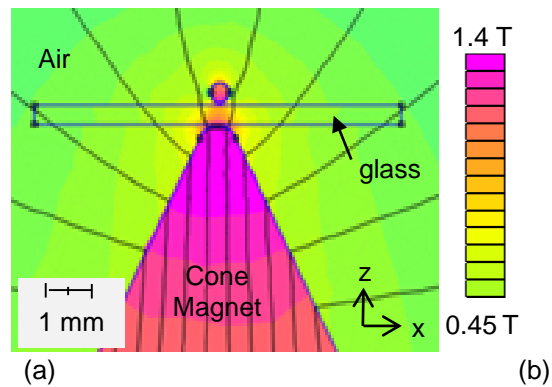


Figure 5-3. FEMM model 500 μm chrome-steel spherical microrobot solution showing the magnetic field density $|B|$ [T]

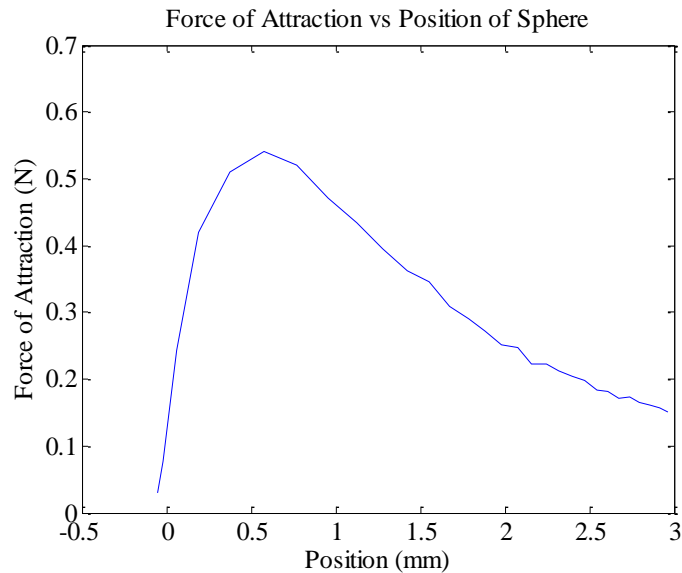


Figure 5-4. Force of attraction of a 500 μm spherical microrobot in x-axis toward the conical magnet tip position located at 0 mm

5.3.2 Multiple Microrobots Magnetic Model

A similar procedure is performed when using two cubical microrobots. The state space model is solved for each microrobot to determine their final position. In addition, F_{other} for each microrobot is calculated by FEMM depending on the position of the other microrobot. A simple dynamic model in FEMM was set up to simulate the experimental conditions with two 500 μm neodymium cubical microrobots, a 500 μm thick glass slide and a 25.4 mm x 25.4 mm conical neodymium magnet as illustrated in Figure 5-5. We approximated its mass to be 0.925 mg using the density of neodymium of 7.4 g/cm^3 . The damping coefficient, b , to 0.41 in our simulation.

We ran the dynamic model to estimate the equilibrium distance of two microrobots in the vicinity of the conical magnet tip as shown in Figure 5-5. In future sections, this type of model will help to determine if the object to be manipulated can be grasped.

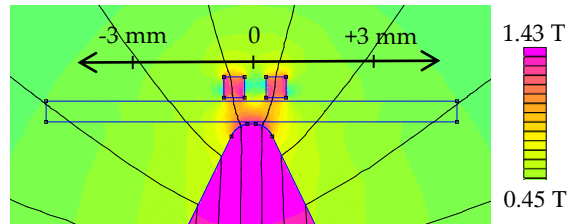


Figure 5-5. FEMM model of Two 500 μm cubical microrobots with initial position at 3 mm from the center of the conical magnet

In this scenario we are interested in observing the motion behavior to illustrate how the microrobots behave when in close proximity of each other (Figure 5-6). Figure 5-6 illustrates the magnetic driving force F_t of two microrobots as both travel towards the tip of the conical magnet when placed 3 mm from the tip. The microrobot on the left side starts at -3 mm mark and the microrobot on the right side starts at +3 mm from the tip of the conical magnet located at 0 (Figure 5-5).

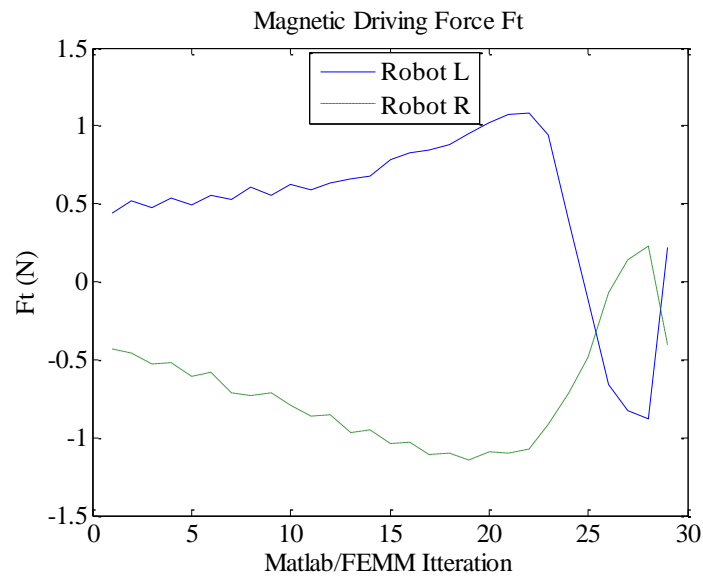


Figure 5-6. Two 500 μm cubical microrobots driving force as they move toward the conical magnet tip position located at 0 mm

5.4 Description of Micromanipulation System

The micromanipulation system (Figure 5-7) is composed of the following: a computer running National Instruments LabVIEW® as the integration and control software, modular prismatic and revolute stages that make up the multi-DOF robotic manipulator with the 25.4 mm x 25 mm conical magnet as its end-effector. The workspace was a silicon wafer fabricated arena or a glass slide suspended above the robotic manipulator and viewed through a microscope with a camera. In order to control the position and orientation of the magnetic cone field source, it is placed on a 5-axis robotic system described in this section. The user can command the robotic manipulator through a joystick user interface, as illustrated in Figures 5-7.

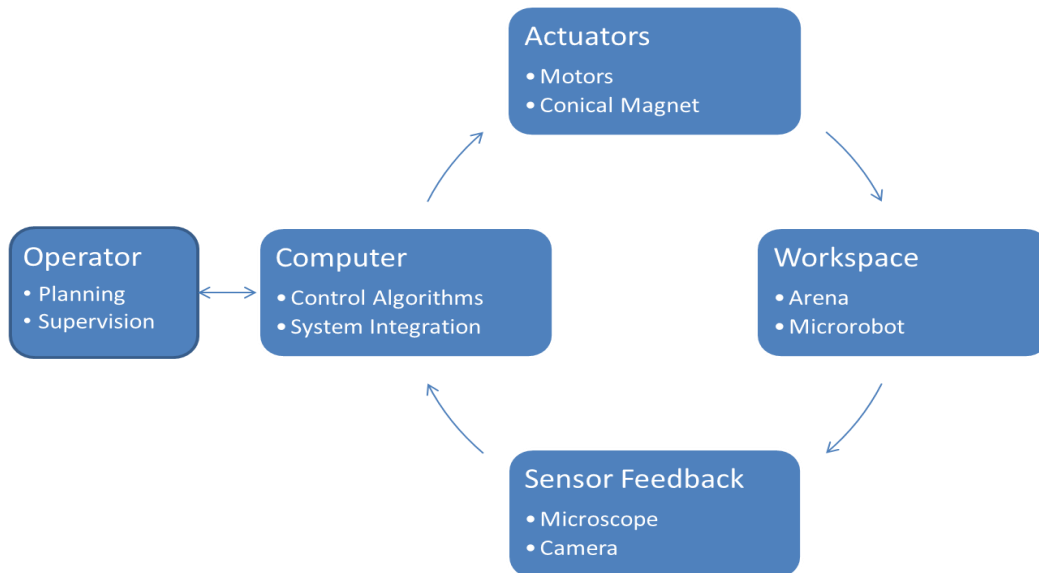


Figure 5-7. Micromanipulation system block diagram

5.4.1 Robotic Manipulator Overview

The multi-DOF robotic manipulator is modular and can be reconfigured to adapt to the manipulation task desired (Figure 5-8). The manipulator's DOF are composed of prismatic joints, P_x , P_y , P_z , in x-axis, y-axis and z-axis respectively, and two revolute

joints, R_z and R_y , in z-axis and y-axis respectively. The conical magnet is mounted on the multi-DOF robotic manipulator as the end-effector as illustrated in Figure 5-8 (c). In this paper we use a 3 DOF (P_z , P_x , P_y) configuration as illustrated in Figure 5-8 (a) to perform task that require a single microrobot such as the scenarios in section 4.1. For the cooperative manipulation task we use a 5 DOF (P_z , P_x , P_y , R_z , R_y) configuration in order to be able to control the orientation of the microrobots formation (Figure 5-8 b).

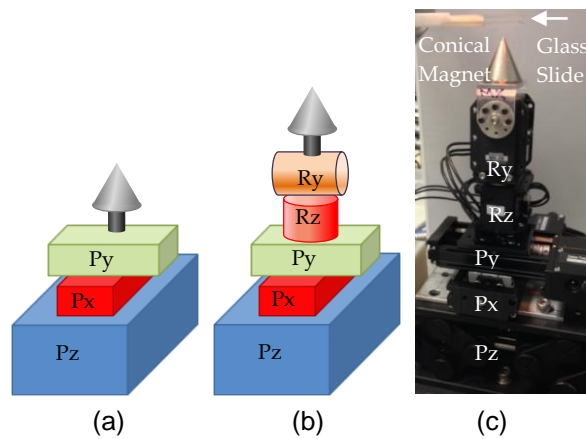


Figure 5-8. Modular robot manipulator (a) 3 DOF (P_z , P_x , P_y) configuration
 (b) 5 DOF (P_z , P_x , P_y , R_z , R_y) configuration
 (c) Actual 5 DOF (P_z , P_x , P_y , R_z , R_y) manipulator

The z-axis is operated by a custom stage motorized with a Dynamixel MX-28 with a 10 mm range of motion at 0.5 mm per revolution. The x-axis and y-axis are operated by a Zaber prismatic stage model T-LSM with a range of motion of 25.4 mm. The revolute joints on the y-axis and the z-axis are also MX-28 with an angular resolution of 0.088° . The workspace is supervised with an Edmund Optics camera, EO-0413M, directly above the workspace with a 87 fps shutter speed and resolution of 752 x 480 pixels.

5.4.2 Microrobots and Workspace

The microrobots in this work measure 250 μm and 500 μm in all three dimensions. We use two different shapes as microrobots, spherical and cubical. The spheres are chrome-steel ball-bearings and the cubical microrobots are Neodymium permanent magnets. Both are commercially available from *Bal – TechTM* and *SuperMagnetMan* respectively. During our experiments, the workspace was a silicon-based fabricated arena or a microscope glass slide, suspended above the robotic manipulator. The workspace is coated with Polydimethylsiloxane (PDMS) to reduce friction using the method in chapter 3.

If multiple microrobots are introduced into the workspace, then each one is placed sequentially in the workspace by simply dropping the microrobot on the workspace near the conical magnet's tip. Microrobots will then self-organize into stable formations. They can also be stacked on top of each other to create a taller microrobot in order to manipulate larger objects. In the case where a double-stack of permanent magnet microrobots are used, they must be assembled beforehand and placed in the workspace as if they were a single microrobot. In the case of a double-stack of spherical chrome-steel microrobots are used, the microrobots are placed in the workspace first and double-stacked as they rest. This step is necessary because they are not permanent magnets and do not have adhesion properties. Moreover, the microrobots do not attract each other laterally because their polarity is self-arranged by the global magnetic field of the conical magnet; instead they repel each other at close proximity. This behavior allows us to control multiple microrobots and gives the ability to double-stack them.

Figure 5-9 illustrates four sets of double-stacked spherical microrobots grasping a 1 mm optical lens during microassembly of lens to a 250 μm optical fiber. The red light on the spherical lens indicates proper alignment between both, lens and optical fiber.

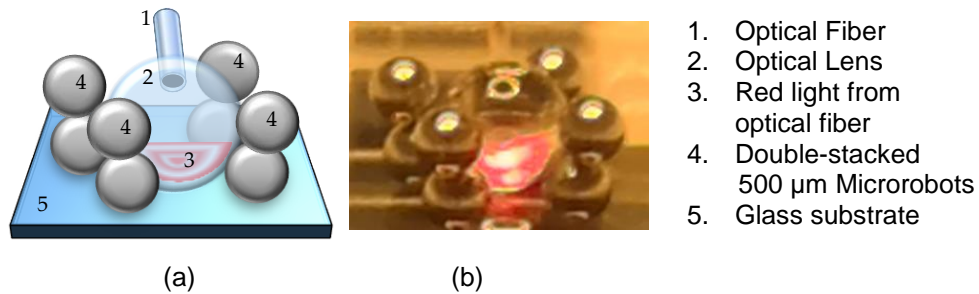


Figure 5-9. Four sets of double-stacked spherical microrobots grasping a 1 mm optical lens a) drawing and b) actual image

5.5 Mobility and Path Planning

In this section we describe microrobot mobility and path planning in order to provide desired system micromanipulation capabilities. In one instance, a single microrobot is itself a component assembled to another structure or simply a part to be sorted from other components. In other applications, multiple microrobots can be used to manipulate non-magnetic material with a grasping behavior.

5.5.1.1 Single Microrobot Mobility

In our application, the actuation of a single microrobot requires a robotic manipulator of at least 3 DOF with prismatic joints in x-axis, y-axis and z-axis. The prismatic joints on x-axis and y-axis provide the planar motion of the microrobot while the prismatic joint in the z-axis allows the user to control the distance of the conical magnet from the workspace to grab and release the microrobot.

In manual mode (teleoperated with joystick) mobility tasks using a single microrobot can be performed through the following sequence:

1. Place the tip of the conical magnet under the microrobot.
2. Using the z-axis stage, raise the conical magnet to approach the workspace.
3. Once the microrobot is attracted to the conical magnet tip. Perform the desired motion or manipulation task.

4. Once the microrobot is at the desired location, release the microrobot by moving the conical magnet away from the workspace.

In automated mode, we make use of the camera microscope feedback to accomplish mobility tasks by navigating in different “arenas”, as illustrated in Figure 5-10. Figure 5-10 (a) shows an example of a task requiring repetition of motion creating a “Figure 8” and Figure 5-10 (b) shows an example of a task with random path sequences. We developed an algorithm for each specific application. For the “Figure 8” task we segment the arena into nine points forming the “Figure 8” and drive the robot to the starting position manually. The user activates the task by clicking a key on the computer’s keyboard. The microrobot then performs the “Figure 8” motion avoiding obstacles. For the random path sequence task (Figure 5-10 b) the user is prompted to enter the desired path in the front panel of the control algorithm by entering a string of numerical characters identifying each gate from 1-9. The gates are formed by the circular pillars on the workspace separated by a distance of 600 μm . On start, the microrobot performs the motion thru the gates for as many repetitions defined by the user. The algorithm to perform the path taken in Figure 5-10 (b) is presented as a pseudocode in Table II.

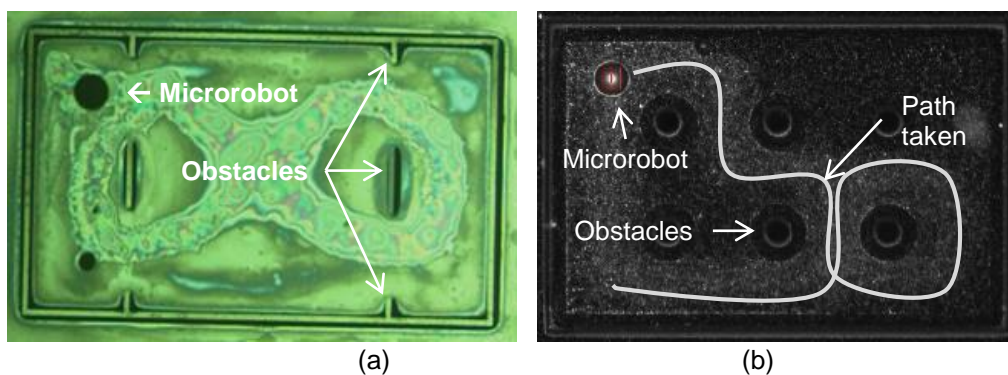


Figure 5-10. 250 μm spherical microrobot performing (a) “Figure 8” mobility task and (b) random path sequence 159863

Table 5-2. Random path sequence algorithm

Random Path Sequence Algorithm	
1.	$S = 159863;$ % Prompt user for sequence
2.	$R = 3;$ % Prompt user for number of repetitions
3.	For $n = 1:R$
4.	$x0 = \text{pixel}(x,y)$ % Vision feedback initial position
5.	Map pixel to μm distance
6.	For $m = 1:\text{length}(S)$
7.	Pass through gate $S(m)$ using increments of $600 \mu\text{m}$ in x-axis and y-axis respectively
8.	End End

5.5.1.2 Single Microrobot Automated Path Detection

Robots and other robotic processes aim to improve production throughput, quality and safety in manufacturing [34, 35]. This is usually done through automation. In this section we present the automation process to determine the path location on the workspace for automated path following. The workspace containing three different paths, circle, rectangle and triangle, illustrated in Figure 5-11 a, where the line is $10 \mu\text{m}$ wide and the rectangle dimensions are $2 \text{ mm} \times 3 \text{ mm}$.

For automated path following we used a $250 \mu\text{m}$ spherical microrobot and a glass slide as the workspace coated with PDMS. The algorithm uses LabVIEW Vision Acquisition (VA) to have the ability to detect objects of interest on the workspace (Figure 5-11 a) and provides the pixel location of the object, for circle it provides the center and for other objects it provides a desired corner pixel location, top-right (TR) and/or bottom-left (BL). In addition, VA allows us to create a color overlay which allows us to discriminate each path as a segment of the workspace (Figure 5-11 b). The user then selects the desired path, C for circle, R for rectangle and T for triangle or a sequence of paths, RTC, and the number of repetitions for each path for the microrobot to follow (Figure 5-11 c). The conical magnet tip is then moved by the P_x and P_y stages to trace the specified path using the algorithm presented in the pseudocode in Table III.

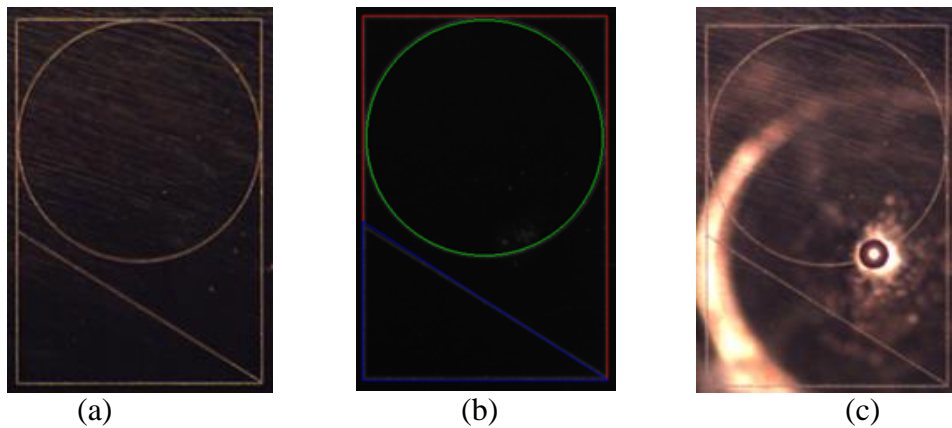


Figure 5-11. Automation process (a) arena with different paths
 (b) path overlay with colors: red-rectangle, green-circle, and blue-triangle
 and (c) 250 μm microrobot following circular path

Table 5-3. Automated path detection algorithm

Automated Path Detection Algorithm	
1.	<i>% draw a line across the microrobot</i> <i>pixel2micron=length of line/size of microrobot;</i>
2.	<i>Path = RC; % Path string</i>
3.	<i>Rep = 21; % 2 rectangle 1 circle motions</i>
4.	<i>VA read path templates from file</i>
5.	<i>circle center (x,y) = VA circle found;</i> <i>rectangle BL corner (x,y)=VA rectangle found;</i> <i>rectangle TR corner (x,y)=VA rectangle found;</i> <i>triangle BL corner (x,y)=VA triangle found;</i> <i>Triangle BR corner (x,Y)=VA triangle found;</i>
6.	<i>Draw overlay by interpolation</i>
7.	For n=1:Length(Path)
8.	<i>Drive=path(n);</i>
9.	For m=1:Rep(n)
10.	<i>IF (Drive=R)</i>
11.	<i>follow trajectory of red pixels;</i>
12.	<i>ELSE IF(Drive=C)</i>
13.	<i>follow trajectory of green pixels;</i>
14.	<i>Else IF(Drive=T)</i>
15.	<i>follow trajectory of blue pixels;</i>
16.	End End

5.5.2 Multiple Microrobot Mobility

A controlled translation of multiple microrobots requires the formation of microrobots to be oriented in the direction of translation in order to maintain a stable formation for micromanipulation of an object. This requirement adds a revolute joint on either x-axis or y-axis to the robot manipulator used for single microrobot control as in Figure 5-8 (a). This allows the translation of the three microrobots to be stable in x-axis or y-axis only. Therefore, a second revolute joint on the z-axis is needed to control the orientation of translation on x-y plane. The micromanipulator robot requires a minimum of 5 DOF to control the mobility of multiple microrobots (Figure 5-8 c).

5.5.2.1 Multiple Microrobot Formation Orientation

Tilting the conical magnet causes two points in x-y plane to experience the same force in the z-axis, therefore two of the microrobots will go to those two positions, microrobot 1 and 2 in Figure 5-12. The third point occurs on the y axis on the plane, microrobot 3, which will trail the leading two microrobots as illustrated in Figure 5-12.

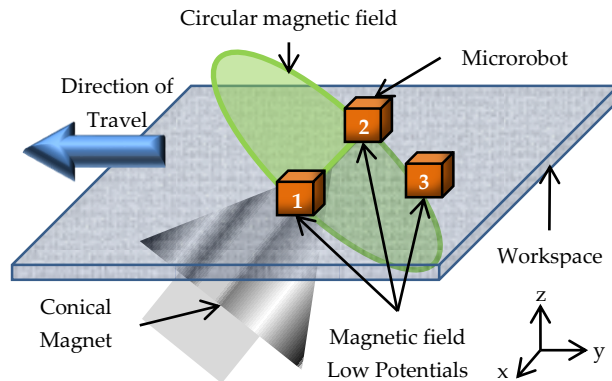


Figure 5-12. Multiple microrobot formation orientation due to tilt

If the conical magnet is not tilted, the microrobots position can shift in a circular manner due to the magnetic field being circular in the x-y plane and friction factors from imperfections of each microrobot or dust particles in their path of travel. Figure 5-13

illustrates the magnetic field gradient as seen on the x-z plane (Figure 5-13 a) and on the y-z plane (Figure 5-13 b). The bending of the force field lines in Figure 5-13 (b) indicate that the microrobots are traveling on the direction of the arrow.

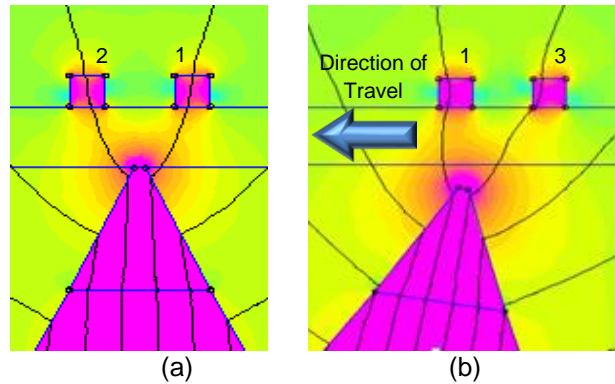


Figure 5-13. FEMM Model of 500 μm microrobots 1 and 2 leading and microrobot 3 trailing formation as seen from (a) x-z plane and (b) y-z plane

5.5.2.2 Multiple Microrobot Mobility Control

Due to the magnetic field of the conical magnet, the magnetic force acting on the microrobots is greater in the z-axis, F_z , perpendicular to the workspace, than the horizontal forces, F_x , on the x-y plane. Figure 5-14 shows the normalized force of attraction that a microrobot experiences as it approaches the tip of the conical magnet. Therefore, due to friction the microrobot formation orientation cannot turn in place by rotating the conical magnet in the z-axis, ϕ . Rotating the conical magnet on the z-axis without translation causes an exchange in the microrobots that are leading, 1 and 2, and the trailing microrobot, 3. In the case where the orientation of the part to be assembled is important, microrobots 1 and 2, must remain in the leading positions. In order to maintain control of the formation, the conical magnet must change the orientation angle, θ , to match the path orientation, ϕ , and translate on x-y plane by a step size, S , that causes

motion on the formation. In this paper the step size, S , is $100\ \mu\text{m}$. This is done until the microrobot orientation matches the direction of the assembly path, P_a (Figure 5-15).

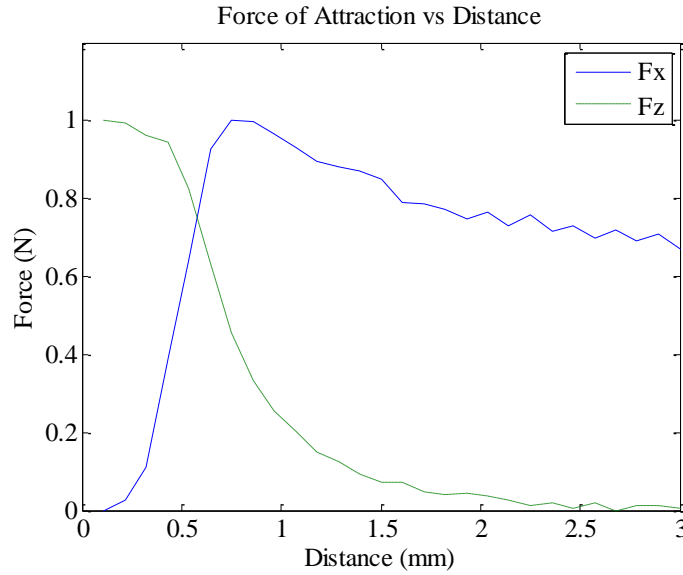


Figure 5-14. Normalized force of attraction vs distance of a $500\ \mu\text{m}$ cubical microrobot in x-axis, F_x , and z-axis, F_z

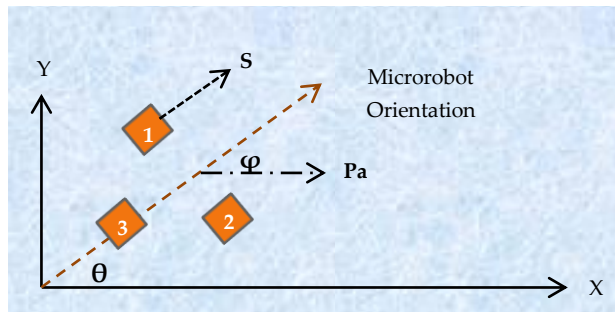


Figure 5-15. Multiple microrobot mobility model (top view)

The microrobot formation dynamics can be modeled using Equations (5.3) and (5.4) where the input to the system is the angle of rotation in the z-axis of the conical magnet.

$$\dot{x} = S \cos(\phi) \tag{5.3}$$

$$\dot{y} = S \sin(\phi) \tag{5.4}$$

5.5.2.3 Cooperative Micromanipulation

Cooperative micromanipulation was performed using three microrobots to move a triangular object from one place to another and a spherical lens using the following micromanipulation primitives which make up an automated assembly sequence:

1. Approach the object for manipulation
2. Open grasp: lower the control magnet to expand the microrobot formation as in Figure 5-16 a.
3. Translate the microrobots to surround the object
4. Close grasp: raise the control magnet to contract the microrobot formation. This creates a grasping motion as in Figure 5-16 c.
5. Translate the object: tilt the conical magnet and translate object to the desired position.
6. Release object: lower the control magnet to expand the microrobot formation once the desired position of the object is achieved.
7. Move away: translate the microrobot away from the object.

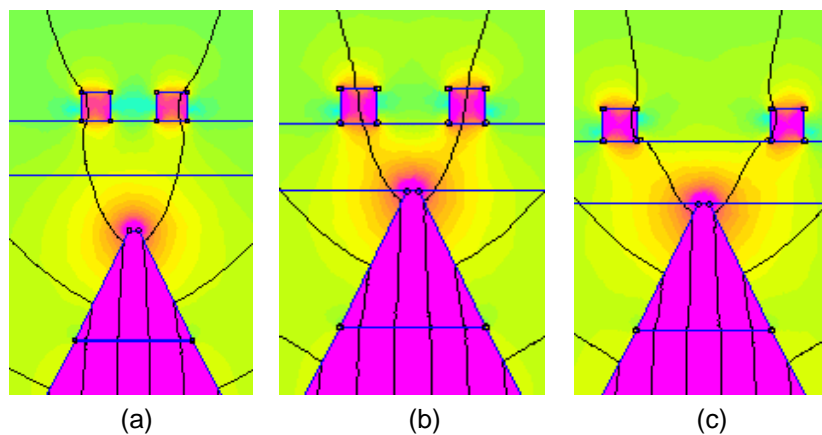


Figure 5-16. Micromanipulation grasp model (a) open grasp
(b) stable grasp and (c) close grasp

5.6 Micromanipulation Experimental Results

Micromanipulation was performed using three microrobots to move a pyramidal object in chapter 4 which demonstrates the manipulation of an object with straight sides. In this chapter we demonstrate micromanipulation of a spherical optical lens using three 500 μm cubical microrobots and four 500 μm spherical, double-stacked, microrobots. The spherical lens is 1 mm in diameter and its material is sapphire weighing approximately 3.98 mg.

One possible application is to serve as a subsystem lens carrier to manufacture microspectrometers [45]. Another application is to manufacture optical circuits that require the alignment of a sapphire lens be aligned to an optical fiber. For this experiment we implemented the later one where a spherical lens, measuring 1 mm in diameter, is transported from an arbitrary location and aligned to an optical fiber with diameter of 250 μm .

5.6.1 Micromanipulation with 3 cubical microrobots

Micromanipulation of the lens was performed using three 500 μm cubical microrobots. The user controls the manipulation using a joystick to transport the lens from a starting position to the assembly point with the optical fiber. Moreover, the sequence illustrated in Figure 5-17 shows that the microrobots' formation maintained its orientation while transporting the lens.

In this chapter, we track the lens by providing a template of the lens and use VA to automatically locate the lens in order to illustrate the trajectory of the lens during manipulation. Figure 5-18 illustrates the lens' (x, y) measured position trajectory during manipulation where the "Start" position is an arbitrary location on the workspace and the "End" position is the location of the assembly target.

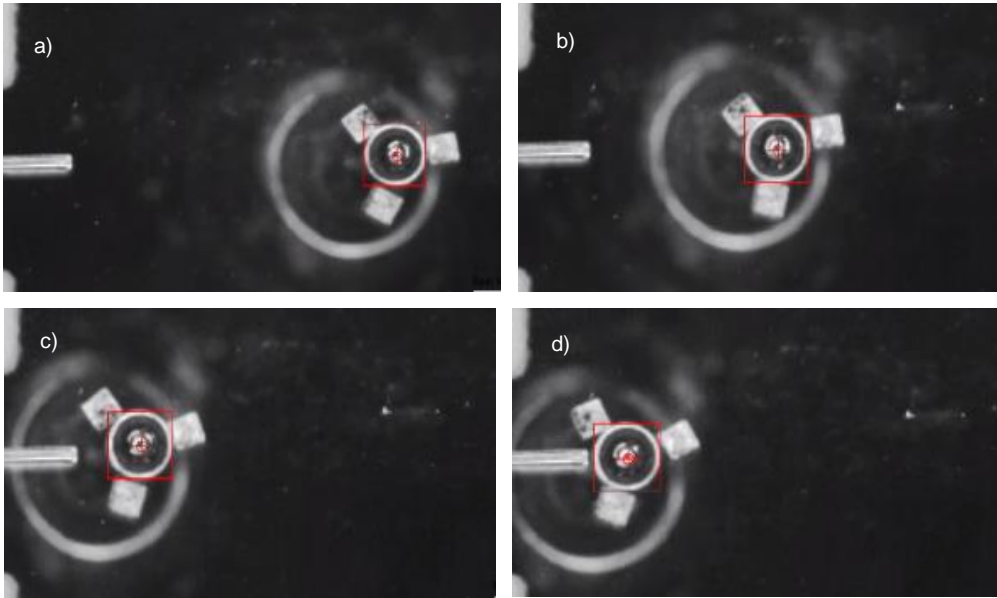


Figure 5-17. Microassembly sequence of a 1mm optical lens with a 250 μm optical fiber using three 500 μm cubical microrobots

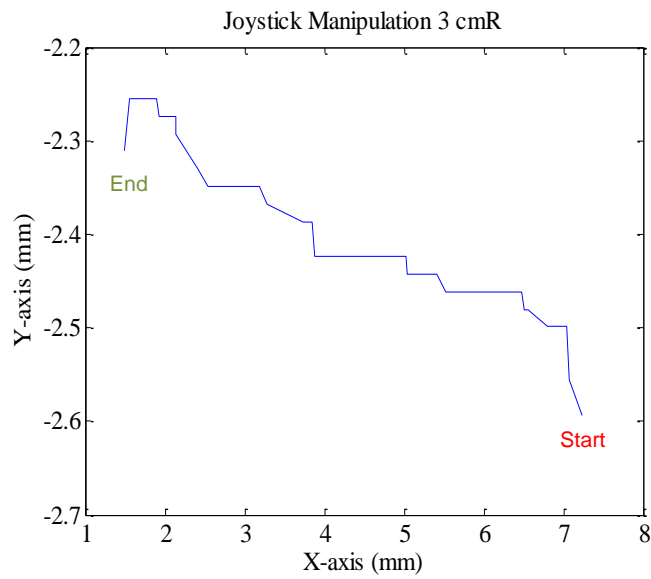


Figure 5-18. Optical lens trajectory during manipulation using three 500 μm cubical microrobots

5.6.2 Micromanipulation with 4 spherical microrobots

Moreover, we performed the same micromanipulation task to assemble the spherical lens to the optical fiber. In this case we used four sets of 500 μm microrobots, in which one set is composed of two microrobots stacked on top of each other as illustrated in Figure 5-19 d. Since the spherical microrobot is smaller than the lens being manipulated, using single-stacked microrobots caused the lens to be pushed out of the grasp. Therefore, it is necessary in this case to use, double-stacked, spherical microrobots. In turn the microrobots will be twice as tall to increase the contact point for better grasp as previously shown in Figure 5-9. Figure 5-20 illustrates the lens' (x, y) position trajectory during manipulation with four spherical, double-stacked, microrobots where the "Start" position is an arbitrary location on the workspace and the "End" position is the location of the assembly target.

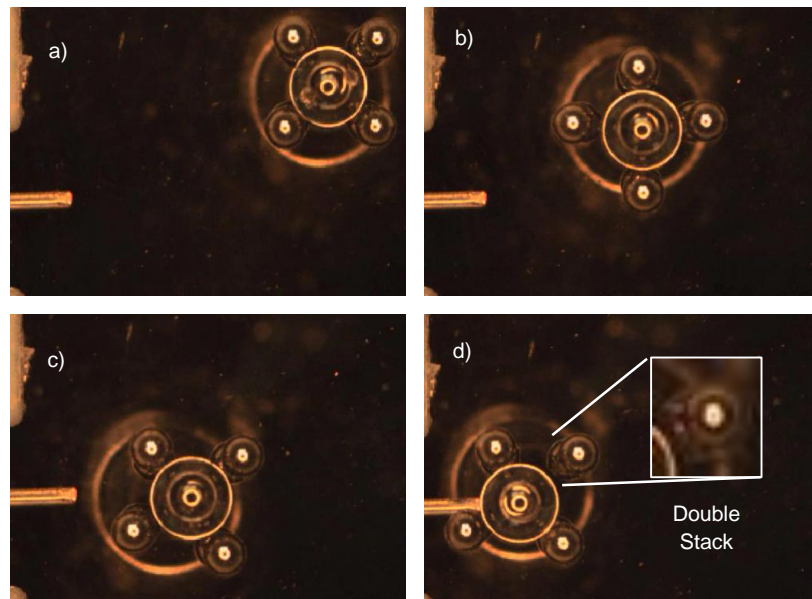


Figure 5-19. Microassembly sequence of a 1mm optical lens with a 250 μm optical fiber using 4 sets of 2 spherical 500 μm microrobots stacked on top of each other

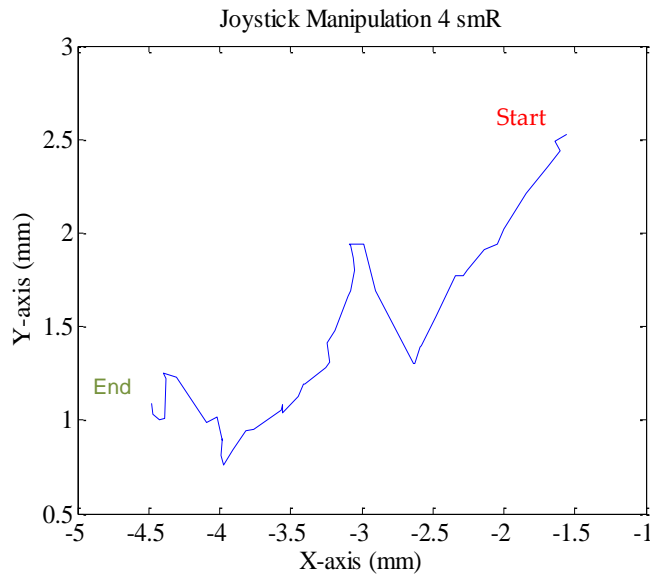


Figure 5-20. Optical lens trajectory during manipulation using four 500 μm spherical, double-stacked microrobots

The results illustrated in Figure 5-18 and Figure 5-20 show the successful microassembly of the lens with the optical fiber. In addition, it demonstrates the flexibility of the system and the modularity capability of the microrobots to adapt to new microassembly requirements. Currently the results are difficult to reproduce due to dust contamination (Figure 5-19 b and c top right) on the workspace causing microrobots to jump sporadically as they encounter such obstacles in their path as seen in Figure 20. We expect that these results will improve if experiments are carried out in liquid environments.

5.7 Conclusion

In this chapter we have presented a unique system to actuate multiple magnetic microrobots with a single magnetic field source mounted as end-effector of a 5-DOF robotic arm. Dynamic simulation models were created and used to anticipate resulting stable microrobot formations that can be achieved by translating and rotating the conical

field source. Experimental results confirm that our driving approach can enable single microrobots to follow apriori-defined paths. Moreover, automation for formation and mobility control of multiple microrobots was presented to demonstrate its potential use in microassembly of optical elements.

Chapter 6

SPATIAL UNCERTAINTY ESTIMATION FOR MODULAR SERIAL LINK ROBOTS

6.1 Introduction

As robots grow smarter, faster and more dexterous, they take on more tasks of human capabilities forcing the manufacturing process and infrastructure to change and to continuously shrink the life span of products [37]. Modular robots give the manufacturing infrastructure the ability to be flexible and reuse the robots in multiple applications of the process [38]. However, robots are inherent to spatial uncertainties due to joint misalignment, link lengths, path of motion to mention a few. These errors become increasingly large when manufacturing at micro and nano scale and can be detrimental for the manufacturing process and or product.

In order to address these shortcomings, we propose a streamlined uncertainty propagation method based on screw theory, which is straightforward to apply to serial link robots, and present our result in Theorem 1. Furthermore, we encapsulate our method into a novel, general purpose software tool to assist in the design and evaluation of serial link modular robots. The proposed computational framework can be used to select modular robot designs that best meet the precision requirements of given assembly tasks. This method is also useful in reducing the need for active feedback during certain robot tasks, leading to high throughput and precision. Moreover, this method is scalable and can be applied multi-scale robots. The contribution of this chapter is the robot pose uncertainty estimate encapsulated in Theorem 1, which applies with a high degree of generality to serial manipulators described using screw kinematics around any operating point in the workspace. The result was illustrated and validated using both simulations as well as experimentally using a 5 degrees of freedom (DOF) microassembly platform.

The chapter is organized as follows: the following sections provides the background information of robot precision, then the description of robot kinematics and uncertainty estimation, followed by the spatial uncertainty estimation software tool, the experimental platform and results and the discussion of results. Lastly, the conclusion and future work are presented.

6.2 Background

Robot precision is generally defined by three metrics: resolution, repeatability and accuracy (RRA) [86]. Resolution is the smallest motion increment that can be detected and/or executed by the robot and depends on the feedback sensor attached to it. Repeatability is the term that describes how a motion is repeated for a certain number of times from the same starting position represented as an average of the error with respect to the actual desired position. Accuracy pertains to the robot's ability to achieve a desire motion or target position [101]. Robots are systems that are composed of individual components, such as joints, links, motors, and sensors with each of these elements introducing an error in the overall manipulation task. In a fixed serial link robot the spatial uncertainty is the overall result of all the components of the robotic system.

Modular robots are systems that allow the user to reconfigure the location of the links, motor actuators, and end-effector. Therefore, in a modular robot, the spatial uncertainty will change as the configuration of the robot changes. In this study we look at the contribution of each module and the effect that it has on the robot's spatial uncertainty and its precision according to its kinematic configuration, type of joint, links and other geometric parameters. Table 6-1 shows some of the commonly used actuation mechanisms and provides their advantages and disadvantages to consider for prototyping the modular robot [102-105]. In addition, Table 6-2 lists some of the common types of joining mechanisms to attach multiple modules used in manipulator robots and

provides the advantage and disadvantage of each mechanism. Similarly, Table 6-3 lists the advantages and disadvantages of three different types of manipulator's kinematic configurations for manipulator robots [106].

Table 6-1. Actuation mechanisms in robotics

Actuator type	Advantage	Disadvantage
Brushless DC servo	Higher efficiency, longer lifespan	Needs closed loop control
Brushed DC servo	Simple speed control	Short lifespan, costly commutator & brush
Stepper motor	High force and repeatability	Low efficiency at higher load, costlier
AC synchronous motor	Synchronous speed, efficient	Higher cost, generally requires high current
Traction motor	High efficiency	High maintenance
Pneumatic	Long life, low cost, high speed	Difficult control, high energy cost, noisy
Hydraulic	High power & stroke, efficient	Bulky, slow, not very precise, fire hazards
Piezo electric	High force and good resolution	Precision affected by hysteresis and creep
Shape memory	high recoverable plastic strain	Nonlinear, response can be unpredictable
Electrothermal	Smaller size for higher stroke	Slow, requires high power, less precise
Electrostatic	Fast, low power	Large size, low force
Magnetic	High force, stroke, contactless	Requires high energy pulse, can be costly

Table 6-2. Types of joining mechanisms used in manipulators

Joining mechanism	Advantage	Disadvantage
Nuts and bolts	Sturdy & reliable, low cost	Only good for fixed configurations
Magnetic locking	Easy to attach /detach	Lower joint strength, more expensive
Cable and pulley	Low cost solution to flexibility	Not reliable for high precision tasks
Mechanical constraints	LEGO® like – easy to install	Deteriorating accuracy over time

Table 6-3. Types of manipulators kinematic configurations

Configuration types	Advantage	Disadvantage
Serial chain	Good for rigid applications	Lower precision due to error accumulation
Parallel	Higher repeatability	Limited workspace, nonlinearity
Hybrid (serial + parallel)	Good for coarse + fine positioning	Higher complexity in design and control

6.3 Robot Kinematics and Spatial Uncertainty Estimation

In this section we present our approach to modeling spatial uncertainties using the product of exponentials and screw kinematics [39].

6.3.1 Robot Kinematics

The robot forward kinematics can be written as a product of exponentials shown in Equations (6.1-6.4), where ${}^0_N T(\theta)$ is the transformation matrix from the base link to the N link due to the translation and rotations, θ , of all robot joints.

$${}^0_N T(\theta) = e^{\hat{\xi}_1 \theta_1} \cdot e^{\hat{\xi}_2 \theta_2} \dots e^{\hat{\xi}_N \theta_N} \cdot [{}^0_N T(0)] \quad (6.1)$$

$$\xi_i(\text{revolute}) = \begin{bmatrix} -w_i \times q_i \\ w_i \end{bmatrix}, \quad \xi_i(\text{prismatic}) = \begin{bmatrix} v_i \\ 0 \end{bmatrix} \quad (6.2)$$

$$e^{\hat{w}\theta} = I + \hat{w} \sin\theta + \hat{w}^2 (1 - \cos\theta) \quad (6.3)$$

$$e^{\hat{\xi}\theta} = \begin{bmatrix} e^{\hat{w}\theta} & (I - e^{\hat{w}\theta})(w \times v) + ww^T v \theta \\ 0 & 1 \end{bmatrix} \quad (6.4)$$

Our notation closely follows the work in [39], and the twist, ξ , represents the instantaneous motion of joint i , revolute and prismatic in Equation (6.2). The net rotation of each joint is represented by Rodrigues formula, Equation (6.3), and is used to solve the screw motion expression in Equation (6.4), which depends on the screw-based link parameters: the directional axis vector of the robot links, \vec{w} , the axis origins for the robot links, \vec{q} , and the joint angle (for revolute joints) or displacement (for prismatic joints), θ .

6.3.2 Spatial Uncertainty Estimation

In a serial robot, each link and joint motion is prone to spatial uncertainty due to static errors such as misalignment of joints, uncertain link lengths, etc., dynamic errors such as resolution of joint actuators, encoders, and controllers, and other errors such as those due to flexibility or the robot, structural vibrations, etc. In this paper, we model the uncertainty of the robot in a quasi-static scenario including static and dynamic errors, which is usually applicable to operation at low speeds in controlled environments. The uncertainty estimate described in this section has a high degree of generality and will apply to any operating points in the workspace.

Introducing the static uncertainty contributed by each link into the screw directional vector, δw , and the axis of its origin position, δq , we can rewrite the robot twist to form Equation (6.5). Moreover, the dynamic uncertainty of motion, $\delta\theta$, is introduced to change the expression of the exponential representation of the joint as Equation (6.6).

$$\xi'_i = \begin{bmatrix} -(w_i + \delta w_i) \times (q_i \times \delta q_i) \\ (w_i + \delta w_i) \end{bmatrix} \cong \xi_i + \delta \xi_i \quad (6.5)$$

$$e^{(\hat{\xi}_i + \delta \hat{\xi}_i)(\theta_i + \delta \theta_i)} \cong e^{(\hat{\xi}_i + \delta \hat{\xi}_i)\theta} \cdot e^{\hat{\xi}_i \delta \theta_i} \quad (6.6)$$

Theorem 1:

The spatial uncertainty of a serial robot, described by POE Equation (6.1) and denoted as a small change in the homogeneous transformation of the end-effector pose

$\delta({}^0_N T(\theta))$, can be estimated using Equation (6.7):

$$\delta({}^0_N T(\theta)) = [\prod_{i=1}^n \delta_i^{P|R}] [{}^0_N T(0)] \quad (7)$$

Where prismatic joints have the uncertainty function δ_i^P in the form of Equation (6.8)

$$\delta_i^P = \left[\left[e^{\hat{\xi}_i \theta_i} + (\delta \hat{\xi}_i \theta_i) \right] \cdot e^{\hat{\xi}_i \delta \theta_i} \right] \quad (8)$$

and revolute joints have the uncertainty function δ_i^R in the form of Equation (6.9).

$$\delta_i^R = \left[\left[e^{\hat{\xi}_i \theta_i} + (\delta \hat{\xi}_i \theta_i) \left[I \frac{\sin \theta_i}{\theta_i} + \hat{\xi}_i \frac{(1 - \cos \theta_i)}{\theta_i} \right] \right] \cdot e^{\hat{\xi}_i \delta \theta_i} \right] \quad (6.9)$$

Proof:

The terms $\hat{\xi}_i$ and $\delta \hat{\xi}_i$ in Equation (6.6) do not commute nor approximate in the scalar technique. Therefore we use Taylor Series expansion (Equation 6.10) to approximate the spatial uncertainty matrix exponential and changed our variables to simplify the illustration as Equation (6.7). By rearranging the terms in Equation (6.10) as shown in Equation (6.11), the derivation provides the exponential form in Equation (6.12).

$$e^{A+\Delta A} = I + \frac{A+\Delta A}{1!} + \frac{(A+\Delta A)^2}{2!} + \dots + \frac{(A+\Delta A)^k}{k!} \quad (6.10)$$

$$\begin{aligned} e^{A+\Delta A} &= I + A + \frac{1}{2}A^2 + \frac{1}{6}A^3 + \dots + \frac{1}{k!}A^k + \Delta A + \frac{1}{2}A\Delta A + \frac{1}{2}\Delta A A + \frac{1}{2}\Delta A^2 \\ &+ \frac{1}{6}A^2\Delta A + \frac{1}{6}A\Delta A c + \frac{1}{6}A\Delta A^2 + \frac{1}{6}\Delta A A^2 + \frac{1}{6}\Delta A A \Delta A + \frac{1}{6}\Delta A^2 A + \frac{1}{6}\Delta A^3 + \dots \end{aligned} \quad (6.11)$$

$$e^{A+\Delta A} = e^A + \sum_{k=0}^{\infty} \left[\frac{1}{k!} \sum_{\alpha=0}^{k-1} (A^\alpha \Delta A A^{(k-1-\alpha)} + \Delta A^\alpha A \Delta A^{(k-1-\alpha)}) \right] \quad (6.12)$$

Substituting our variables with $A = \hat{\xi}_i$ and $\Delta A = \delta \hat{\xi}_i$ we can write the robot pose as a sum in Equation (6.13).

$$\delta({}^0_N T(\theta)) = \left[\prod_{i=1}^n \left[\left[e^{\hat{\xi}_i \theta_i} + \sum_{k=0}^{\infty} \left[\frac{1}{k!} \sum_{\alpha=0}^{k-1} \left((\hat{\xi}_i \theta_i)^\alpha (\delta \hat{\xi}_i \theta_i) (\hat{\xi}_i \theta_i)^{(k-1-\alpha)} \right) \right] \right] \cdot e^{\hat{\xi}_i \delta \theta_i} \right] \right] [{}^0_N T(0)] \quad (6.13)$$

The summation term of Equation (6.13) is further simplified in the following manner as illustrated in Equation (6.14) and by rearranging and eliminating higher order terms as in Equation (6.15) we attain Equation (6.16).

$$\sum_{k=0}^{\infty} \left[\frac{1}{k!} \sum_{\alpha=0}^{k-1} \left((\hat{\xi}_i \theta_i)^\alpha (\delta \hat{\xi}_i \theta_i) (\hat{\xi}_i \theta_i)^{(k-1-\alpha)} \right) \right] = \frac{1}{1!} (\delta \hat{\xi}_i \theta_i)$$

$$\begin{aligned}
& + \frac{1}{2!} [(\delta \hat{\xi}_i \theta_i)(\hat{\xi}_i \theta_i) + (\hat{\xi}_i \theta_i)(\delta \hat{\xi}_i \theta_i)] \\
& + \frac{1}{3!} [(\delta \hat{\xi}_i \theta_i)(\hat{\xi}_i \theta_i)^2 + (\hat{\xi}_i \theta_i)(\delta \hat{\xi}_i \theta_i)(\hat{\xi}_i \theta_i) + (\hat{\xi}_i \theta_i)^2(\delta \hat{\xi}_i \theta_i)] \\
& + \frac{1}{4!} [(\delta \hat{\xi}_i \theta_i)(\hat{\xi}_i \theta_i)^3 + (\hat{\xi}_i \theta_i)(\delta \hat{\xi}_i \theta_i)(\hat{\xi}_i \theta_i)^2 + (\hat{\xi}_i \theta_i)^2(\delta \hat{\xi}_i \theta_i)(\hat{\xi}_i \theta_i) + \\
& \quad (\hat{\xi}_i \theta_i)^3(\delta \hat{\xi}_i \theta_i)] + \dots + \tag{6.14}
\end{aligned}$$

$$(\delta \hat{\xi}_i \theta_i) \left[I + \frac{1}{2!} (\hat{\xi}_i \theta_i) + \frac{1}{3!} (\hat{\xi}_i \theta_i)^2 + \frac{1}{4!} (\hat{\xi}_i \theta_i)^3 + \dots \right] \tag{6.15}$$

$$\begin{aligned}
& = (\delta \hat{\xi}_i \theta_i) \left[I + \frac{1}{2!} (\hat{\xi}_i \theta_i) + \frac{1}{3!} (\hat{\xi}_i \theta_i)^2 + \frac{1}{4!} (\hat{\xi}_i \theta_i)^3 + \dots \right] (\hat{\xi}_i \theta_i) (\hat{\xi}_i \theta_i)^{-1} \\
& = (\delta \hat{\xi}_i \theta_i) \frac{\left[I + \frac{1}{2!} (\hat{\xi}_i \theta_i) + \frac{1}{3!} (\hat{\xi}_i \theta_i)^2 + \frac{1}{4!} (\hat{\xi}_i \theta_i)^3 + \dots \right]}{\theta_i} (\hat{\xi}_i^{-1}) \tag{6.16}
\end{aligned}$$

The following properties of higher order terms of $\hat{\xi}_i$ illustrated in Equation (6.17) and Equation (6.18) allows rewriting by substituting the summation element in Equation (6.13) with Equation (6.18) to obtain Equation (6.9).

$$\begin{aligned}
\hat{\xi}'^2 & = \begin{bmatrix} \hat{w}^2 & 0 \\ 0 & 0 \end{bmatrix}, \quad \hat{\xi}'^3 = \begin{bmatrix} \hat{w}^3 & 0 \\ 0 & 0 \end{bmatrix}, \quad \dots \text{ and} \\
\hat{w}^3 & = -\hat{w}, \quad \hat{w}^4 = -\hat{w}^2, \quad \hat{w}^5 = \hat{w}, \quad \hat{w}^6 = \hat{w}^2, \quad \hat{w}^7 = -\hat{w}, \quad \dots \tag{6.17} \\
\text{sum} & = (\delta \hat{\xi}_i \theta_i) \frac{\left[\left(\theta_i - \frac{\theta_i^3}{3!} + \frac{\theta_i^5}{5!} - \dots \right) \hat{\xi}_i + \left(\frac{\theta_i^2}{2!} - \frac{\theta_i^4}{4!} + \frac{\theta_i^6}{6!} - \dots \right) \hat{\xi}_i^2 \right]}{\theta_i} (\hat{\xi}_i^{-1}) \\
& = (\delta \hat{\xi}_i \theta_i) \frac{\left[\left(\theta_i - \frac{\theta_i^3}{3!} + \frac{\theta_i^5}{5!} - \dots \right) + \left(\frac{\theta_i^2}{2!} - \frac{\theta_i^4}{4!} + \frac{\theta_i^6}{6!} - \dots \right) \hat{\xi}_i \right]}{\theta_i} \\
& = (\delta \hat{\xi}_i \theta_i) \left[I \frac{\sin \theta_i}{\theta_i} + \hat{\xi}_i \frac{(1 - \cos \theta_i)}{\theta_i} \right] \tag{6.18}
\end{aligned}$$

Since the screw for prismatic joints has the form of $\hat{\xi} \theta$ in Equation (6.19) [39], the higher order terms in Equation (6.10) are eliminated reducing to Equation (6.20).

$$\hat{\xi} \theta = \begin{bmatrix} 0 & v \\ 0 & 0 \end{bmatrix} \tag{6.19}$$

$$e^{A + \Delta A} = I + A + \Delta A \tag{6.20}$$

Substituting our variables with $A = \hat{\xi}_i$ and $\Delta A = \delta \hat{\xi}_i$ and using Equation (6.14), the summation simplifies to Equation (6.21). As a result, we obtain the estimate in Equation (6.8).

$$sum = (\delta \hat{\xi}_i \theta_i) \quad (6.21)$$

In both Equation (8) and Equation (9), the additive term is the static uncertainty or error due to link misalignment and the multiplicative term is the dynamic uncertainty or error due to joint motion. The dynamic uncertainty depends on the joint motion range. In other words, the end-effector position becomes increasingly uncertain over larger robot travel distances and repeated motions.

6.4 Spatial Uncertainty Estimation Software Tool

In order to implement Equation (6.7), we developed a software tool to aid in the design and evaluation of modular robots. The tool was programmed using National Instruments Laboratory Virtual Instrument Engineering Workbench (LabVIEW) which provides a user friendly interface. Equation (6.7) is used to estimate the spatial uncertainty of modular robots used for assembly, packaging or manipulation to determine their optimal configuration according to the task's precision requirements. The software tool allows the user to design and evaluate a modular robotic platform by a simulation before it is prototyped. It provides the user with graphical representation of the robot created and its spatial uncertainty estimation, plots give results in 3D as well as displaying numeric data.

6.4.1 Software Features

The spatial uncertainty estimation block diagram is illustrated in Figure 6-1. On start, the spatial uncertainty estimation software allows the user to enter the number of modules, their type and orientation by simply entering a string of letters. For instance,

the robot configuration string containing the letters x, y, z describe prismatic joints with orientation in the x, y and z plane respectively.

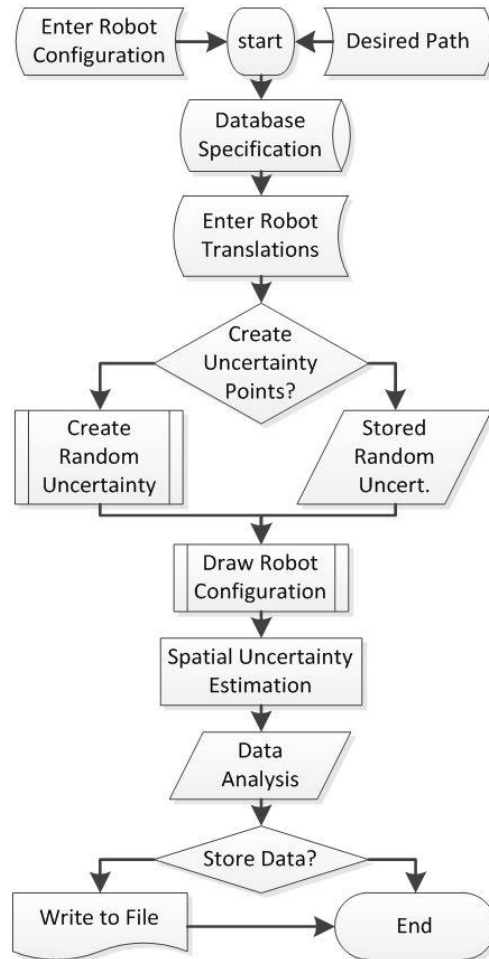


Figure 6-1. Spatial uncertainty estimation block diagram

The letters t, b, g describe revolute joints with axis of rotation x, y, z respectively. The software also allows the user to desired path sequence for the robot platform to take. For example, a letter string containing the following “zxytg” and path “x” indicates that the user desires to run the simulation for a 5 DOF robotic platform with the three prismatic joints and two revolute joints and begin its motion in the x-axis. Moreover, the prismatic joint “z” operating in the z-axis will be joint, θ_1 , “x” is θ_2 , similarly all other joints

connecting to the last revolute joint where “g” is θ_6 pertaining to Equation (6.1), Equation (8) and Equation (6.9). The software then accesses a database that contains the precision specifications for the joints specified in the robot configuration string. The user is prompted to enter the desired translation or rotation of each joint for analysis. In addition, the software provides the option to generate random variables for each of the joints within their specified tolerance values from the database. The random variables are used as spatial uncertainties and can be stored for more iterations of different robot configurations or they can be generated new. The software’s front panel, illustrated in Figure 6-2, provides a graphical representation of the joints used, boxes for prismatic joints and cylinders for revolute joints.

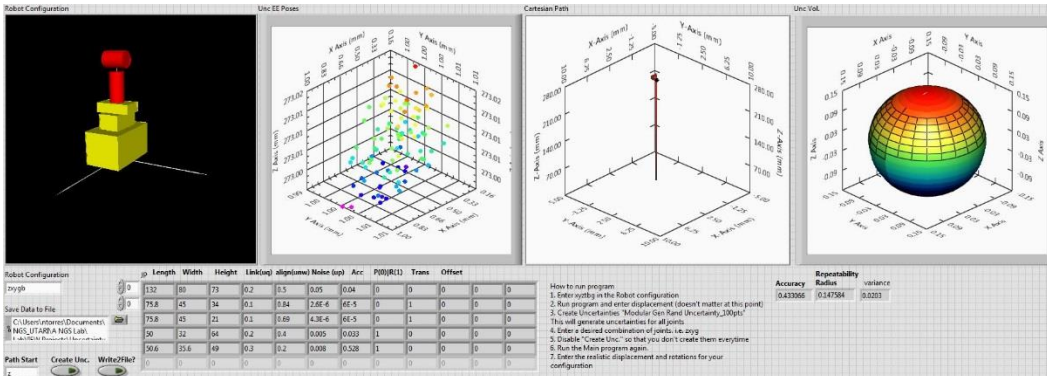


Figure 6-2. Spatial uncertainty estimation software front panel

Then it proceeds to evaluate the robot configuration using Equation (6.7) and provides the results with the following illustrations: 1) the order and number of joints or modules used, 2) the distribution of random uncertainties generated, 3) the path in which the robot performed its motion, and 4) the volume of the spatial uncertainty with the accuracy of the respective robot configuration. Since the random uncertainties are generated in software their variation will be similar for all joints. Therefore, for illustration purposes of this experiment, the spatial uncertainty is represented as a spherical volume

with a radius determined by taking the average spatial uncertainty in x-axis, y-axis and z-axis.

6.4.2 Spatial Uncertainty Estimation Results

The spatial uncertainty estimation simulation was conducted with two sets of robots with different DOFs. The first robot positioner consists of 3 DOF, with prismatic joints $P_x, P_y, P_z = \theta_1, \theta_2, \theta_3$ and the second robot positioner consists of 5 DOF, with prismatic joints and revolute joints $P_x, P_y, P_z, R_y, R_z = \theta_1, \theta_2, \theta_3, \theta_4, \theta_5$ where, P, stands for a prismatic joint and, R, stands for a revolute joint in the axis noted by the subscripts. A database file of six joints was created to simulate the availability of three prismatic joints and three revolute joints or modules all having different precision specifications as listed in Table 6-4.

Table 6-4. Database file of modules' precision specifications (mm & degrees)

Length (mm)	Width (mm)	Height (mm)	Link Unc. (mm)	Align Unc. (°)	Dyn Unc.	Accuracy	Actuator
75.8	45	21	0.1	0.84	2.6 nm	0.008	P
75.8	45	21	0.1	0.69	4.3 nm	0.01	P
132	80	40	0.2	0.5	50 μ m	0.02	P
50.6	35.6	35.5	0.3	0.2	0.12°	0.08	R
50.6	35.6	35.5	0.3	0.2	0.026°	0.29	R
50	32	40	0.5	0.4	0.023°	0.3	R

In the future, the database will contain the information for all available modules that are compatible for assembly of the modular robot. The random points were generated for each joint and saved for all trials of the modular robot in different configurations within the negative “-” to positive “+” range of the modules' uncertainties.

The spatial uncertainty estimation was simulated for three different configurations of the 3 DOF robot with the following robot configurations: (Pz,Px,Py), (Px,Py,Pz), (Py,Px,Pz) and the joints were moved from 0 to 100 mm in increments of 10 mm per

sample. The results of the spatial uncertainty estimation tool for the modules translation of 0 mm, 50 mm and 100 mm are illustrated in Figure 6-3.

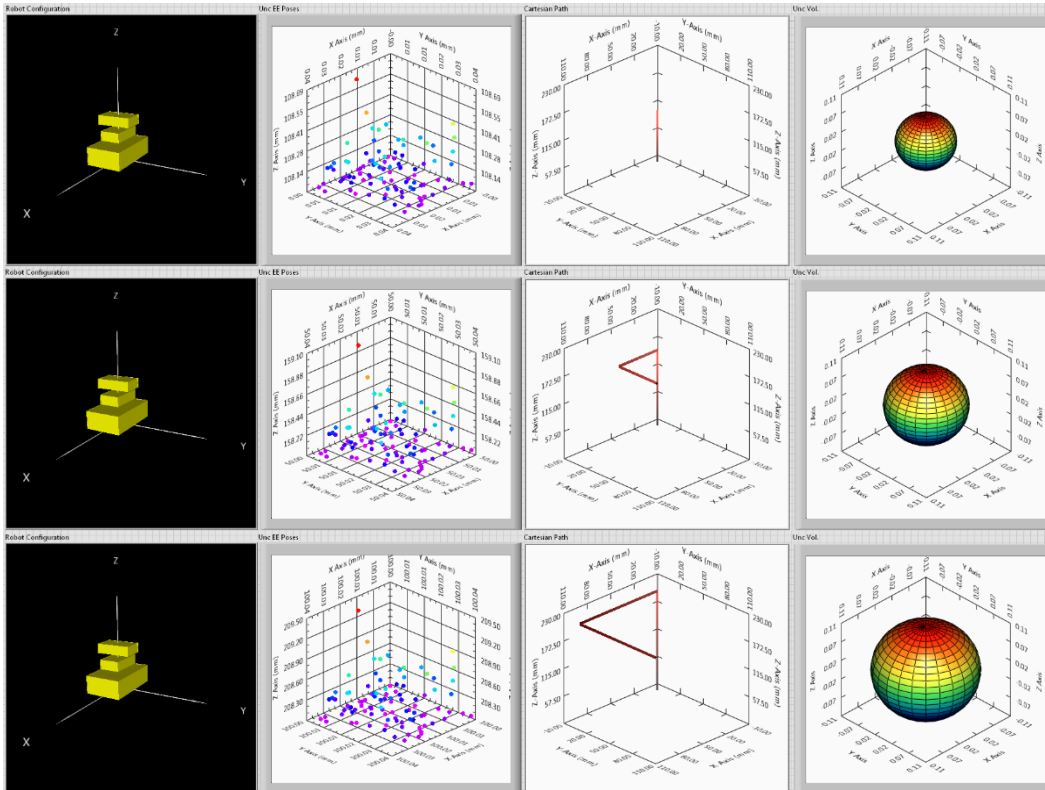


Figure 6-3. 3 DOF robots results for translations 0 mm, 50 mm and 100 mm

The simulation was repeated for the different robot configurations and the results were recorded as in Figure 6-4. Figure 6-4 shows that as the motion increases, repeatability and the spatial uncertainty of the robot degrade. However, it is difficult to determine which robot configuration is more precise by looking at repeatability alone. Therefore, we determine its accuracy as the error or spatial uncertainty compared to the desired position where the lower the accuracy metric, the better the performance precision is for the configuration as illustrated in Figure 6-5. Using the accuracy performance metric it is clear the robot configuration (z,x,y) is the optimal robot configuration. In addition, the desired path to take in 3D should be the same as the robot configuration.

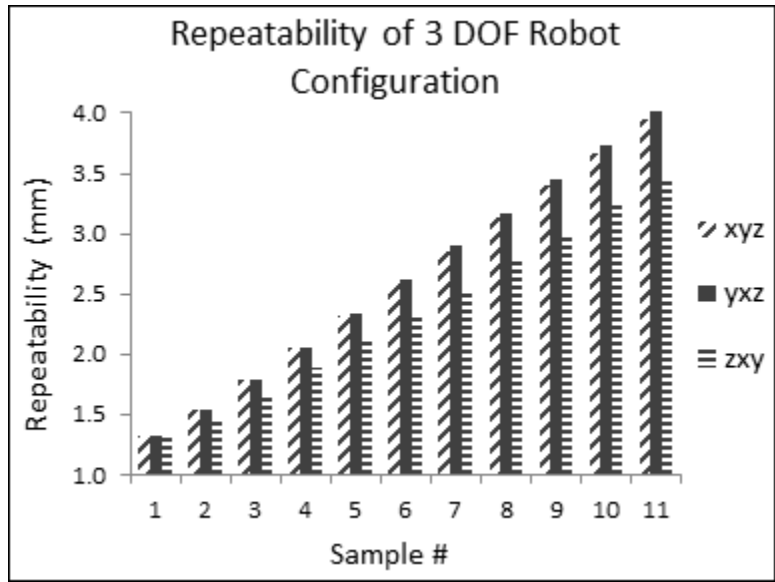


Figure 6-4. Repeatability of a 3 DOF robot configurations vs motion

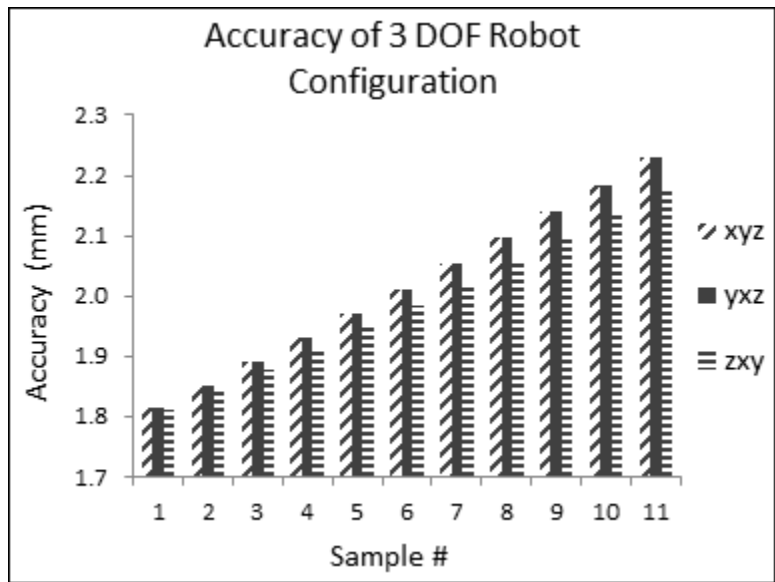


Figure 6-5. Accuracy of a 3 DOF robot configurations vs motion

Next, the spatial uncertainty estimation was simulated for four different configurations of a 5 DOF robot with the following robot configurations (Pz,Px,Py,Rz,Ry),

P_x, P_y, P_z, R_z, R_y), $(P_y, P_x, P_z, R_z, R_y)$ and $(R_z, P_z, P_x, P_y, P_y)$ as illustrated in Figure 6-6. In this part of the simulation, the robot's joints were operated in their different ranges of motion and acquired ten samples within their range. The different ranges of motion simulate a robot performing a task with limited range of motion. The prismatic joint, P_z , operating the z-axis was sampled from 0 mm to 10 mm, the prismatic joints, P_x and P_y , operating the x-axis and y-axis were sampled from 0 mm to 25 mm, the revolute joint, R_z , on the z-axis was sampled from 0 degrees to 45 degrees, the revolute joint, R_y , on the y-axis was sampled from 0 mm to 10 mm.

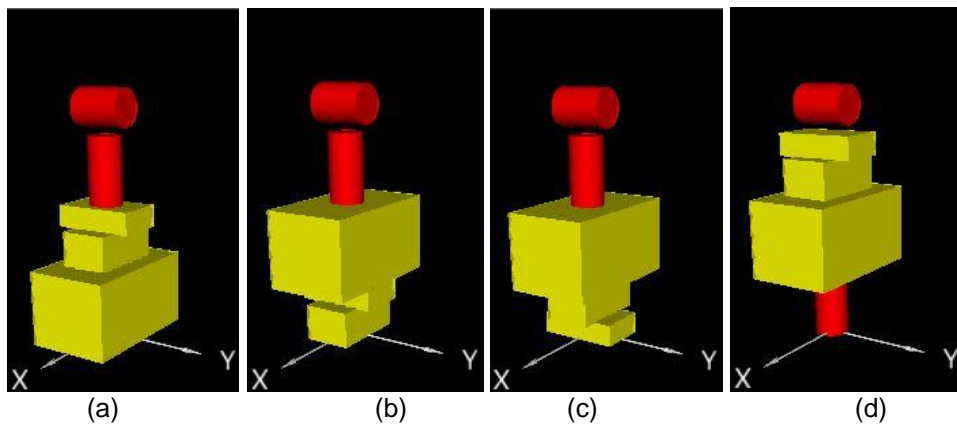


Figure 6-6. Robot configurations: (a) $(P_z, P_x, P_y, R_z, R_y)$,

(b) $(P_x, P_y, P_z, R_z, R_y)$, (c) $(P_y, P_x, P_z, R_z, R_y)$ and (d) $(R_z, P_z, P_x, P_y, R_y)$

The spatial uncertainty repeatability results for all four configurations are illustrated in Figure 6-7 and also shows that as the range of motion increases, so does the spatial uncertainty. Figure 6-8 illustrates the accuracy of each configuration and shows that the 5 DOF robot configuration $(P_z, P_x, P_y, R_z, R_y)$ has the best precision.

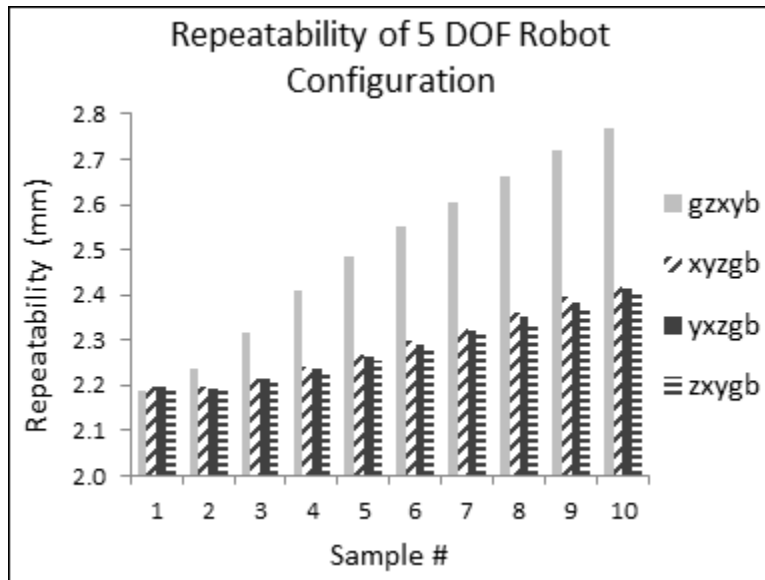


Figure 6-7. Repeatability of a 5 DOF robot configurations vs motion

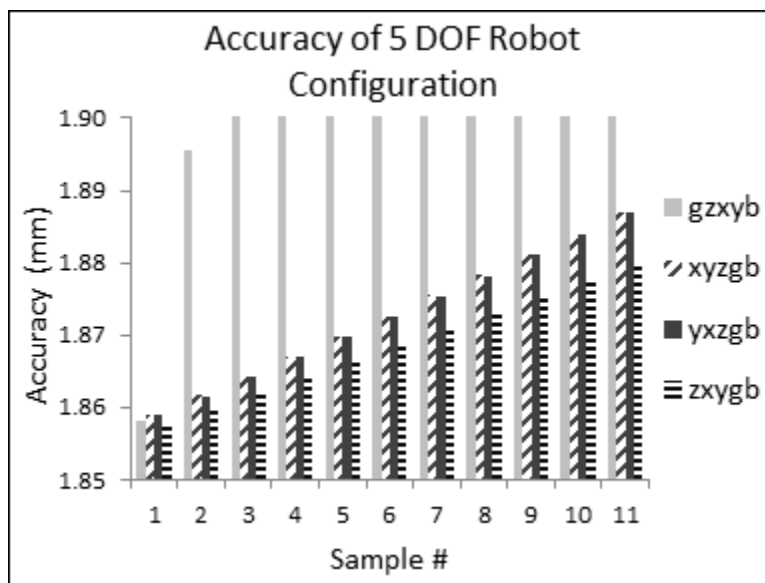


Figure 6-8. Accuracy of a 5 DOF robot configurations vs motion

6.5 Experimental Results

The 5 DOF modular serial link robot manipulator illustrated in Figure 6-9 was used for the experimental evaluation of the spatial uncertainty estimation software. The robotic manipulator is composed of three prismatic joints (x , y , z) and two revolute joints ($th1$, $th2$) with a conical magnet as the end-effector as in Figure 6-9.

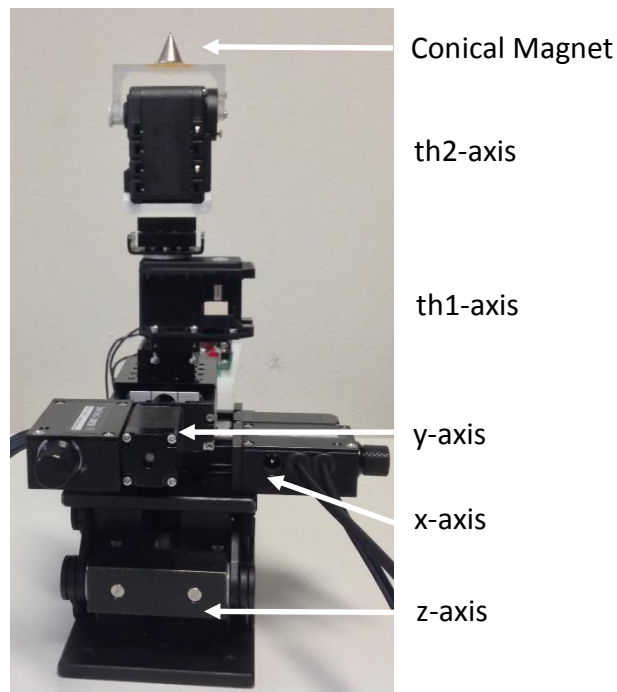


Figure 6-9. 5 DOF robotic manipulation system

The two linear stages, Zaber T-LSM series, provide a 25.4 mm range of motion for (x , y), a custom linear stage is motorized using a Dynamixel MX-28 to provide the motion in the z -axis. This custom stage provides a 10 mm range of motion at 0.5 mm per revolution. The revolute joint, $th1$, is a Dynamixel model MX-28 with PID control and the revolute joint, $th2$, is a Dynamixel model AX-12 with position control. These revolute joints are used to control the orientation of the conical magnet which in turn controls multiple robots' position. The conical magnets used are available commercially in the following

dimensions 1) 12.7 mm height and base diameter and 2) 25.4 mm height and base diameter. The conical shape of the magnet focuses the magnetic field at the tip of the magnet which is used as the actuation force to control magnetic microparts [46].

6.5.1 Description of the Experimental Setup

In order to measure the repeatability of the modules available a vision algorithm was developed in LabVIEW to track a 500 μm cube mounted at the tip of a conical magnet that serves as the end effector of the modular robot manipulator used in this chapter (Figure 6-10 a).

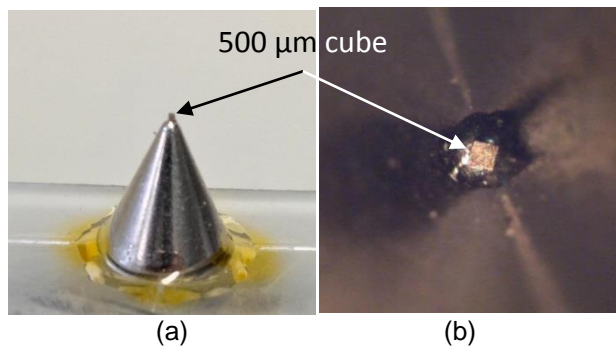


Figure 6-10. 500 μm cube (a) mounted at the tip of a conical end-effector and (b) 500 μm cube top view

The vision algorithm searches for a template image of the cube (Fig. 6-10 b) on the camera feed and determines the translation and rotation of the cube's barycenter in a two dimensional (2D) plane and saves the data on a spreadsheet. The microscope was set to a 0.5x zoom in order to be able to observe the positions and workspace of the two different robot configurations since the end-effector position changes when reconfiguring the robot. The size of the image processed is 740x480 pixels which provide a resolution of 12.5 $\mu\text{m}/\text{pixel}$.

The repeatability of each module was characterized individually by performing ten repeated translations and rotations of each module for different ranges. For prismatic

joints the motion profile was performed with the following ranges: 0 to 250 μm , 0 to 500 μm , 0 to 1000 μm , 0 to 2000 μm and 0 to 4000 μm . For the revolute joints the motion profile was performed under 90 degrees. Due to the shape of the object being a square from the top view, the tracking vision algorithm will determine a 90 degree rotation to be 0 degrees. Therefore, the characterization ranges are: 0° to 10°, 0° to 20°, 0° to 40°, 0° to 60°, 0° to 80°. For our custom stage operating the prismatic joint, on the z-axis, we performed one motion from 0 to 500 μm and observed the projected translation on the x and y axis. Table 6-5 shows the characterization results of the modules used for the application on a 5 DOF robotic manipulator.

Table 6-5. Precision specifics of the assortment of positioners used in the manipulation system

Module	Characterization			
	Repeatability ($\mu\text{m} ^\circ$)	Link Error (mm)	Axis Error ($^\circ$)	Dynamic Error ($\mu\text{m} ^\circ$)
Px	1.0127	0.1	0.84	0.00253
Py	4.0010	0.1	0.69	0.00710
Pz	20.1270	0.2	0.5	0.095
Ry	1.4352	0.3	0.2	0.035
Rz	0.9065	0.5	0.4	0.023

The repeatability of each module was computed as the variance of the samples of motion from the desired position. The accuracy is calculated as a mean of the same pose measurements. Due to the number of samples (100 for simulations, 10 for experiments) to define these statistics, our reported results have at least a 95% confidence interval. The link error was estimated by measuring the link length of each module. The axis error for the prismatic module operating on the z-axis, the revolute joints operating in the y-axis and z-axis were measured using a digital level. The axis error for the prismatic modules operating on the x-axis and y-axis were measured using the camera feedback. The dynamic error was measured over 1000 μm range of motion

performed for characterization. The link error, axis error and the dynamic error results in Table 6-5, were then used in the uncertainty simulation as a database file in order to compare with implemented results.

6.5.2 Experimental Results

Due to size and weight of the prismatic joint and the availability of the modular links, only two robot configurations were possible (Pz, Px, Py, Rz, Ry) and (Pz, Rz, Px, Py, Ry) . These two robot configurations of the 5 DOF a robotic manipulator were simulated (Figure 6-11) maintaining the same random points for each module.

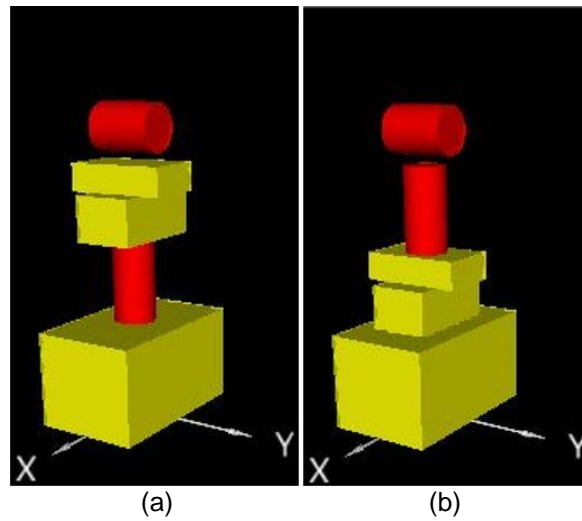


Figure 6-11. Robot configurations used for simulation

(a) (Pz, Rz, Px, Py, Ry) and (b) (Pz, Px, Py, Rz, Ry)

The 3D spatial uncertainty estimation results were averaged and are illustrated in Table 6-6 which show that the robot configuration (Pz, Px, Py, Rz, Ry) has higher precision.

Table 6-6. Repeatability and accuracy of simulated robot

Configuration	Repeatability (mm)	Accuracy (mm)
	Position	Position
(Pz, Px, Py, Rz, Ry)	4.3726	1.8551
(Pz, Rz, Px, Py, Ry)	5.1534	2.7268

Similarly, the two robot configurations were built as in Figure 6-12 and analyzed its performance using the vision tracking algorithm. Both configurations were commanded to move to a position of $\Delta(Pz, Px, Py, Rz, Ry) = (500 \mu\text{m}, 2000 \mu\text{m}, 3000 \mu\text{m}, 30^\circ, 5^\circ)$ from the initial position and repeated the same motion for ten iterations and measured its variance to determine its repeatability.

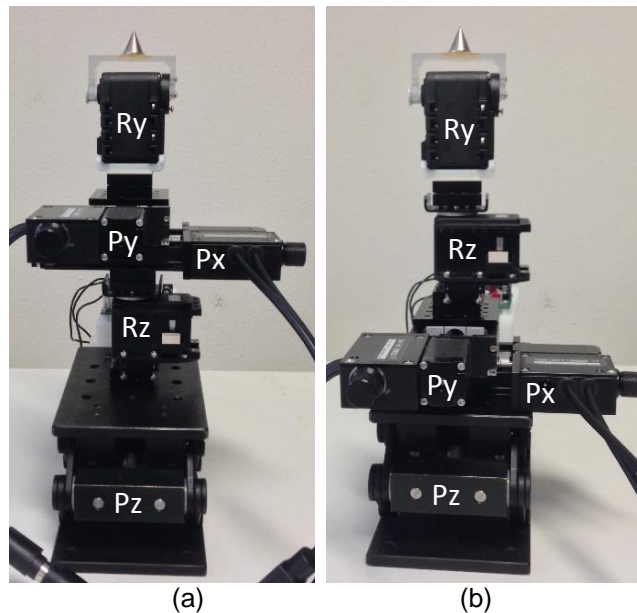


Figure 6-12. Robot configurations used for experiment

(a) (Pz, Rz, Px, Py, Ry) and (b) (Pz, Px, Py, Rz, Ry)

The accuracy was measured as the average of the ten measurements comparing the result with the planar position $(2002.49 \mu\text{m}, 3001.44 \mu\text{m})$ corresponding to the commanded motion. The repeatability here is calculated as the variance of the pose in the x and y axes, and represented as the radius of a circular area of uncertainty. We used a 95% confidence interval to determine the repeatability and accuracy range for each configuration. The 2D spatial uncertainty results of both configurations are shown in Table 6-7, where the lower number signifies better repeatability. Therefore by comparing the repeatability and accuracy results of both robot configurations, it can be determined

that the best configuration is (Pz,Px,Py,Rz,Ry) since it has a more compact repeatability and more accuracy than the robot configuration (Pz,Rz,Px,Py,Ry).

Table 6-7. Repeatability and accuracy of actual robot

Configuration	Repeatability (mm)	Accuracy (mm)	Confidence (mm)
	Position	Position	+ -
(Pz,Px,Py,Rz,Ry)	0.0034	0.2689	0.00143
(Pz,Rz,Px,Py,Ry)	0.0239	3.6348	0.00857

6.6 Discussion of Results

The modular serial link robot platforms analysis shows how these robots are subject to hardware errors, static and dynamic due to uncertainties in link length, misalignment and range of motion. The results show that the mathematical approximation for the spatial uncertainty given by Equation (6.7) is helpful to analyze the precision of modular robots, and study how the precision of the robot changes depending on design. The results from simulation show that you can analyze all possible configurations of the modular robot (Figure 6-3 - Figure 6-8) and show that as the motion of the robot increases, so does its spatial uncertainty. In addition, comparing the repeatability and accuracy results the two configurations of the spatial uncertainty simulation a 5 DOF robot in Table 6-6 and the results of the experiment of the same robot in Table 6-7, both reach the same conclusion that configuration (Pz,Px,Py,Rz,Ry) is the most accurate. Therefore, by using the software tool demonstrated in this chapter, users can design and analyze modular robots leading to rapid design and implementation of such systems.

6.7 Conclusion

A unique spatial uncertainty estimation method was proposed and demonstrated in simulation and experiments. Using this approximation method, a quantified analysis to measure the precision of different robot kinematic configurations and different trajectories in the workspace can be accomplished. The resulting software tool facilitated the analysis

by providing a user friendly environment that allows the user to interact with graphical representations, gathering specifications automatically from a database and responding to the user prompts on the screen. In addition, the visual results provided by the software, allow the user to understand the analysis with the option to save the data acquired during the analysis. The spatial uncertainty simulation results were then validated with experimental results in which both agree in the same result. The spatial uncertainty estimation tool demonstrated can potentially reduce the time that is required to design and analyze the performance of general manufacturing serial link robots for optimal performance for specific processes on-demand.

Chapter 7

CONCLUSION AND FUTURE WORK

7.1 Magnetic actuation of microrobots with focused magnetic field

In this thesis we presented a novel method to increase the actuation precision of magnetic microrobots by focusing the magnetic field via metallic spheres placed on top of a conical permanent magnet. We presented experimental results demonstrating that microrobot motion is linear and repeatable at moderate speeds, and can be exploited in future automation applications. Precision was further enhanced by the use of a simple method to coat the work space of the microrobot with a thin film of PDMS which significantly reduces stiction. 2D microrobot motion are comparable with EM coil actuators, however, the drive system we employ is less complex and more intuitive to operate.

7.2 Cooperative micromanipulation

We introduced a novel method to control multiple microrobots for cooperative micromanipulation using the potential field which is similar to the magnetic field generated by the conical magnet. We have presented different simulation models used to study the behavior of microrobot and predict stable formations. A 5 DOF robotic manipulator was set up to study the optimal tilt angle of the conical magnet to achieve a stable formations for micromanipulation as well as to characterize the size range of the objects that can be manipulated with the system. Results show that it is possible to grasp microscopic objects, move them and release them using a “gripper” composed of three spherical and cubic microrobots. The potential for controlled swarming behavior of microrobots using our system was also validated experimentally. Future work includes the implementation of an intuitive human- robot interface to operate magnetic microgrippers during microassembly applications. The characterization of the microrobot

grasp force, and enhancements to precision by operating the microrobots in aqueous environments. In addition, using a robotic arm to control the conical magnet introduces spatial uncertainties that compound the microrobot spatial uncertainties. Closed loop feedback control of the system is necessary in order to perform automated micromanipulation.

7.3 Spatial Uncertainty Estimation

We proposed a unique spatial uncertainty estimation method and demonstrated it in simulation and experiments. Using this approximation method, a quantified analysis to measure the precision of different robot kinematic configurations and different trajectories in the workspace can be accomplished. The resulting software tool facilitated the analysis by providing a user friendly environment that allows the user to interact with graphical representations, gathering specifications automatically from a database and responding to the user prompts on the screen. In addition, the visual results provided by the software, allow the user to understand the analysis with the option to save the data acquired during the analysis. The spatial uncertainty simulation results were then validated with experimental results in which both agree in the same result. The spatial uncertainty estimation tool demonstrated can potentially reduce the time that is required to design and analyze the performance of general manufacturing serial link robots for optimal performance for specific processes on-demand. Future work includes the de integration of pre-existing CAD drawings to generate an accurate visual description the robot configuration. In addition, the inverse of the spatial uncertainty estimation can be applied to make the tool accept a desired tolerance of spatial uncertainty and the tool will generate a robot that performs within the spatial uncertainty tolerance. In addition, we will investigate extensions of the uncertainty estimation result to parallel robots. In particular,

it will interesting to analyze whether Equation (6.7) in chapter 6, is a useful overestimate of the pose uncertainty in parallel structures, given their kinematic constraints.

7.4 Future Work on Trust Based Multi-Robot Control

Future work includes the development of the Trust-Based Multi-Robot Control to include the experimental set up and characterization. Then implement to micromanipulation to enhance the precision of multiple microrobot control and develop a manufacturing application for the system presented in this thesis.

7.4.1 Introduction

Cooperative localization and control of multiple robots is an important part of industrial automation that has gained much interest in order to be able to adapt to the production demands. The global market continually emphasize on the need for new manufacturing paradigms that can swiftly and inexpensively adapt to the rapidly changing production demands. Therefore, shifting from rule-based automation to trust-based automation is more commercially sustainable in the evolving market making manufacturing processes and robots more flexible, intelligent, and cooperative that can adapt to the varying system dynamics, planned and unplanned. In addition, this will allow an easier transition and quick reconfiguration of the manufacturing framework for on-demand production. Such implementation requires novel distributed control techniques to ensure convergence to consensus among robots with limited or no connectivity with other robots in the workspace.

In this section, a Trust-Based approach is discussed to improve the precision of a robotic manipulation system. The method described uses statistical results from the spatial uncertainty estimation developed in Chapter 6. The spatial uncertainty estimation is done ahead of time for specific motion trajectories. The resulting manipulation/motion error is compensated proactively with an intermittent observer through closed loop. This

approach will allow the system to operate faster than conventional closed-loop control approaches by estimating a trust value and tracking the position of the robotic manipulator intermittently (Figure 7-1).

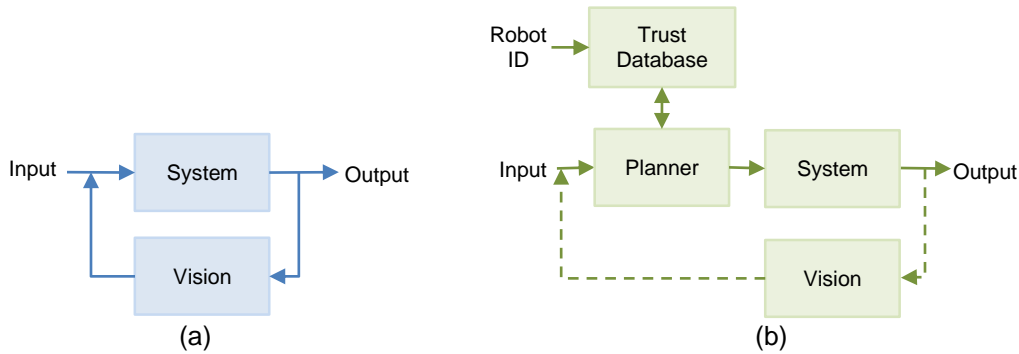


Figure 7-1. Automation method a) conventional and b) trust-based

7.4.2 Multiple Robot Control Background

Game theory has been used in manufacturing engineering using cooperative and competitive strategies to control multiple robots [87]. In [88], game theory is used to design hybrid controllers for complex systems ideally suited for multi-agent systems. Others have used game theory to make their robots smarter due to the similarity between game theory and the independent decisions of multiple robots [89, 90].

Other methods used to control multiple robots related to trust are through the “Auction-bid” method in which each robot attempts to perform a given task, this is termed as bid. The robots that do not participate or contribute to the bid, are alienated from the team and become the untrusted members [91]. This is important since all robots do not have the same reliability or trustworthiness. However, this approach eliminates robots from being implemented. Another trust method, “Trust spreading,” is used in [92, 93]. The method deals with the trust based on the neighboring robots. However all robots are considered equal and trust themselves whereas in the trust-based control method presented in this thesis, each robot has its own spatial uncertainties, or self-trust.

7.4.3 Trust-Based Model for Cooperative Control

The “Trust” term is the reliability of information that can be obtained from a robot. Trust values indicate the trustworthiness of a robot in a cooperative multi-robot system. Cooperative control of multiple robots in traditional applications assumes that all robots are equally trustworthy. However, depending on the application, this assumption can be fatal for manufacturing at micro and nano scale. Hence the need for a solution for the consensus problem with multi-robot control based on trust. The trust for each robot is assigned by the algorithm developed in [65] known as RoboTrust. The RoboTrust algorithm updates each robot’s trust periodically considering the history of each robot and is modified to include a “self-trust” value from the spatial uncertainty estimation algorithm developed in Chapter 6.

The method also implements a Kalman consensus filter [66] for a dynamic state estimation and we use the inverse of the error covariance to evaluate the robot’s confidence to achieve the desired task. Depending on the trust and the confidence of each robot, the vision feedback can intermittently be activated at different periods of time to evaluate the current position of the robot.

7.4.4 Trust Model for Robotic Manipulators

Robotic manipulators contain several sources of uncertainty as discussed in Chapter 6. Therefore it cannot have complete trust on its own as assumed in [65]. The spatial uncertainty of the robots are used to establish self-trust and compound it to the global trust values. Figure 7-2 illustrates two robotic manipulators with multiple DOF. The two manipulators are required to work cooperatively to assemble a part or hand-over the part to a different robotic platform.

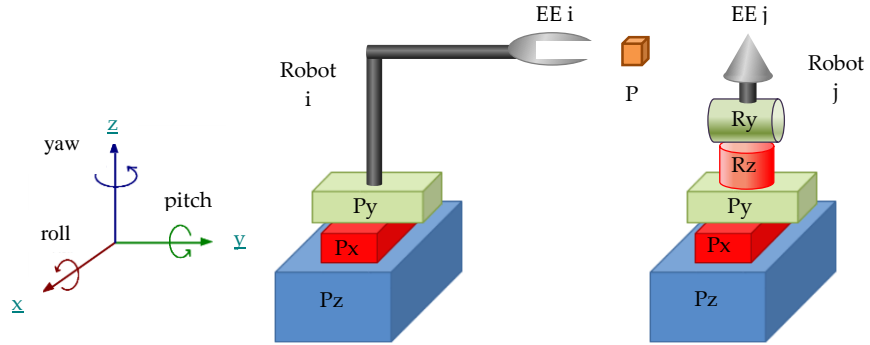


Figure 7-2. Cooperative task of two robotic manipulators
to assemble part “P” with end-effector “EE”

First we determine the self-trust value for each robotic platform assigned by the spatial uncertainty estimation software in chapter 6. Then we build the global trust value between the two robots. A Kalman consensus filter is used to calculate the trust estimates for specific tasks of each robot and used the covariance of the measurement noise to obtain optimal results.

7.4.4.1 Self-Trust Model

The desired robot pose, x_i , is defined as Equation (7.1) where $i=1, \dots, N$ represents the number of robots. The actual pose, \tilde{x} , of the robot are calculated using Equation (7.2) from section 6.3.2

$$x_i = \begin{bmatrix} R & P \\ 0 & 1 \end{bmatrix} \quad (7.1)$$

$$\tilde{x}_i = [\prod_{i=1}^n \delta_i^{P|R}] [{}^0T(0)] \quad (7.2)$$

The self-trust, $T_i(k)$, is generated for each robotic manipulator due to their spatial uncertainty. The self-trust is calculated using Equation (7.3) where $\zeta \geq 0$ is a parameter designed to achieve a desired self-trust.

$$T_i(k) = \exp\left(-\frac{\|\tilde{x}_i - x_i\|}{\|\tilde{x}_i\| + \zeta}\right) \quad (7.3)$$

7.4.4.2 Global Trust Model

Using graph theory from [81], A collection of N nodes are connected with each other using the directed graph interaction topology. $\mathcal{A} = [a_{ij}] \in R^{N \times N}$ is the associated weighted adjacency matrix of the directed graph. The update equation for the global trust between manipulator arms is given as Equation (7.4):

$$T_{ij}(k+1) = T_{ij}(k) + \frac{1}{\sum_{m \in N_i, N_j} a_{im} a_{mj} + 1} * \sum_{m \in N_i, N_j} a_{ij} a_{im} a_{mj} T_i(k) \left(\sqrt{T_{im}(k) T_{mj}(k)} - T_{ij}(k) \right) \quad (7.4)$$

where $T_{ij}(k)$ is the previous global trust value; $m \in \mathcal{N}_i$ is the neighbors of node i and a_{ij} is the weight/adjacency matrix.

7.4.4.3 Confidence Factor Model

A new term $\sigma_{ij}(k)$ is introduced here, which represents the confidence or reputation or accuracy factor in Equation (7.5). This decides if it falls in the range of other trustworthy agents. A pre-defined range of values is calculated by using the normal distribution of the mean and standard deviations. We can alter this value by changing α . This ensures that even though some values do not fall in the desired range but need not be eliminated completely while computing.

$$\sum_{m \in N} |T_{jm}(k) - T_{im}(k)| < \alpha \sigma_{ij}(k) \quad (7.5)$$

7.4.5 Trust Estimation by Kalman Filter

The confidence of successfully performing a particular task depends on the design tolerance, motion profile and operating environmental conditions. In real robot assembly, the actual position of a robot manipulator cannot be obtained due to hardware and sensor limitations of the camera only providing 3 DOF. As a result measurement noise is introduced. The Kalman filter information is used to evaluate the trust about such noise for each robot. Moreover, the process noises are also inevitable in the leader's

dynamics. The information matrices in Kalman filter is used to evaluate the trust about the noise called confidence. N robot arms are considered to achieve consensus to the leader's state with distributed measurements of robot arms' pose.

Each robot platform, i , has the following Kalman filter model [107]:

System Model

$$X_i(k+1) = A(k)X_i(k) + B_i(k)U_i(k) + Q_i(k) \quad (7.6)$$

Measurement model $Z_i(k)$ where $v_i(k)$ is the distributed measurement noise.

$$Z_i(k) = H_i X_i(k) + v_i(k) \quad (7.7)$$

The time update error covariance

$$P_i^-(k+1) = A(k)P_i(k)A^T(k) + G(k)Q_i(k)G^T(k) \quad (7.8)$$

The time update estimate model

$$\hat{X}_i^-(k+1) = A(k)\hat{X}_i(k) + B(k)U(k) \quad (7.9)$$

The measurement update error covariance

$$P_i(k+1) = [(P_i^-(k+1))^{-1} + H_i^T(k+1)R^{-1}(k+1)H_i(k+1)]^{-1} \quad (7.10)$$

The measurement update estimate

$$\begin{aligned} \hat{X}_i(k+1) = & \hat{X}_i^-(k+1) + P_i(k+1)H_i^T(k+1)R^{-1}(k+1)(Z_i(k+1) - \\ & H_i(k+1)\hat{X}_i^-(k+1)) \end{aligned} \quad (7.11)$$

Kalman Gain

$$K_i(k) = P_i(k)H_i^T(k)R^{-1}(k) \quad (7.12)$$

Summarizing, the Kalman consensus filter the leader's state estimate becomes

$$\begin{aligned} \hat{X}_i(k+1) = & X_i(k+1) + P_i(k+1) \sum_{j=1}^N a_{ij} \left(P_j(k+1) \right)^{-1} * \left(\hat{X}_j(k+1) + \right. \\ & \left. v_{ij}(k+1) - \hat{X}_i^-(k+1) \right) \end{aligned} \quad (7.13)$$

Then a trust-based Kalman consensus scheme consists of replacing by introducing the Trust term T_{ij} as in Equation (7.14)

$$\hat{X}_i(k+1) = X_i(k+1) + P_i(k+1) \sum_{j=1}^N a_{ij} (P_j(k+1))^{-1} * T_{ij} (\hat{X}_j(k+1) + v_{ij}(k+1) - \hat{X}_i^-(k+1)) \quad (7.14)$$

7.4.6 Robot Model for Kalman Consensus

In this section we are assuming to have a 5 DOF robotic manipulator described in Section 5.3.1 with a camera observing its end-effector. In order to implement the Kalman filter the robotic manipulator system needs to be modeled to include the robot's model, the measurement model and the measurement update model. Following the Kalman filter convention in Table 2.1 in [107] the discrete time robot model is described as Equation (7.15) where, I , is an identity matrix of size of the robot's DOF and J , is the Jacobian of the end-effector, U , is the systems' input and Q is the variance of the pose from the spatial uncertainty estimation simulation.

$$X_{k+1} = I_{(6 \times 6)} X_k + J_k U_k + Q \quad (7.15)$$

The 5 DOF robotic manipulator is composed of three prismatic joints, x, y, z and two revolute joints on y -axis and z -axis. Therefore the components of the robot model take the form of the following Equation (7.16) and Equation (7.17).

$$X_k = \begin{bmatrix} x \\ y \\ z \\ \phi \\ \theta \end{bmatrix}, \quad U_k = \begin{bmatrix} P_x \\ P_y \\ P_z \\ \theta \\ \varphi \end{bmatrix} \quad (7.16)$$

$$J_k = \begin{bmatrix} 1 & 0 & 0 & 0 & L \cos(\theta) \cos(\varphi) & -L \sin(\theta) \sin(\varphi) \\ 0 & 1 & 0 & 0 & L \cos(\theta) \sin(\varphi) & L \sin(\theta) \cos(\varphi) \\ 0 & 0 & 1 & 0 & -L \sin(\theta) & 0 \\ 0 & 0 & 0 & 1 & 0 & 0 \\ 0 & 0 & 0 & 0 & 1 & 0 \\ 0 & 0 & 0 & 0 & 0 & 1 \end{bmatrix} \quad (7.17)$$

Measurements are taken via a camera that can extract the (x, y) coordinates, in pixels of the end-effector with the shape of a square. Therefore the measurement

model is as in Equation (7.18) where H , is the output of the camera (Equation 7.19) and v_k is the noise from the measurement.

$$Z_k = H_k X_k + v_k \quad (7.18)$$

$$H_k = \begin{bmatrix} x' \\ y' \\ z' \end{bmatrix} \quad (7.19)$$

The parameters (x', y', z') is the translation vector of the feature/object on it's frame using the camera information as a transformation in Equation (7.20) where R is a 3D rotation matrix of the object orientation angles roll, pitch, yaw (ϕ, Θ, φ) where C and S are the trigonometric functions cosine and sine of the subscript angle in Equation (7.21).

$$\begin{bmatrix} x' \\ y' \\ z' \end{bmatrix} = \begin{bmatrix} X \\ Y \\ Z \end{bmatrix} - R \begin{bmatrix} x_0 \\ y_0 \\ z_0 \end{bmatrix} \quad (7.20)$$

$$R(\phi\Theta\varphi) = \begin{bmatrix} C_\phi C_\Theta & C_\phi S_\Theta S_\varphi - S_\phi C_\varphi & C_\phi S_\Theta C_\varphi + S_\phi S_\varphi \\ S_\phi C_\Theta & S_\phi S_\Theta S_\varphi + C_\phi C_\varphi & S_\phi S_\Theta C_\varphi - C_\phi S_\varphi \\ -S_\Theta & C_\Theta S_\varphi & C_\Theta C_\varphi \end{bmatrix} \quad (7.21)$$

The vector (X, Y, Z) is the coordinates of the feature/object on the object's frame, (x_0, y_0, z_0) is a known coordinate vector of the feature/object on the object's frame. The vector (X, Y, Z) is determined using Equation (7.22) where f is the focal length, (Pl_x, Pl_y) is the image coordinates in pixels of the feature/object point on the image plane.

$$\begin{bmatrix} Pl_x \\ Pl_y \\ 1 \end{bmatrix} = \frac{1}{z} \begin{bmatrix} f & 0 & 0 \\ 0 & f & 0 \\ 0 & 0 & 1 \end{bmatrix} \begin{bmatrix} X \\ Y \\ Z \end{bmatrix} \quad (7.22)$$

7.4.7 Conclusion

We presented the description of the system in order to be able to use a Kalman filter to help in the experiment set-up and implementation of the Trust-Based multi-robot control. The work is still in progress and thus forms part of the future work.

APPENDIX A
IEEE RAS MOBILE MICRO/NANO-ROBOTICS CHALLENGE

A.1 Introduction

The Mobile Micro/nano-robotics Challenge (MMC) was initially sponsored by the U.S. National Institute of Standards and Technology (NIST) starting in 2007 under the name of Robocop Nanogram [76]. In 2013, NIST delegated responsibility for the organization of the MMC to the IEEE Robotics and Automation Society [94]. The MMC event currently takes place in the International Conference on Robotics and Automation (ICRA) and consists of three events: the autonomous mobility and accuracy challenge, the microassembly challenge and the MMC Showcase & Poster Session. The events simulate common tasks that are found in medical applications, involving high speed closed-loop positioning, and in microassembly applications, involving precision motion control. Teams must furnish their own microrobots, which must fit within a virtual cube that is 500 μm on a side, and bring their own millimeter sized competition arenas and equipment to operate microrobots.

A.2 MMC 2013 Requirements

The MMC 2013 Autonomous Mobility Challenge required an arena with a 3.5 mm x 2 mm region (Figure A.1) in which the robot will pass through four gates performing a “Figure 8” motion trajectory passing through gates [1, 2, 3, 4, 1]. Each team performed three trials in which each trial started when the referee instructed each team and the time was recorded when the microrobot started moving and the trial ended when the microrobot stopped its motion. In this event the fastest microrobot wins. In the Microassembly Challenge the arena consisted of a 1.5 mm x 2 mm starting region connected to a 2 mm x 0.75 mm channel (Figure A.2). Upon a referee signal, the microrobot begins to assemble each components into the narrow channel. The triangles are to be assembled with gap no larger than 50 μm . The trial ends after 2 minutes and the score is the number of triangles assembled. The team with more triangles assembled wins the challenge.

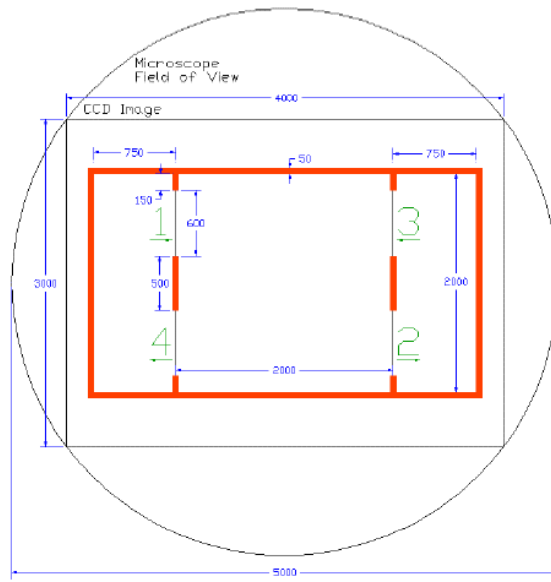


Figure A.1. Autonomous mobility challenge arena dimensions

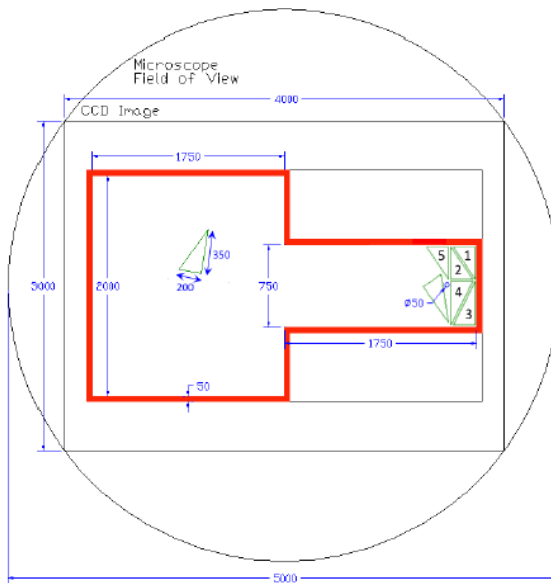


Figure A.2. Microassembly challenge arena dimensions

A.2.1 LabVIEW Interface

The LabVIEW Interface used is illustrated in Figure A.3. The interface allowed the user to operate in different modes, Joystick and Kinect mode for the assembly challenge and Automated mode for the autonomous mobility challenge.

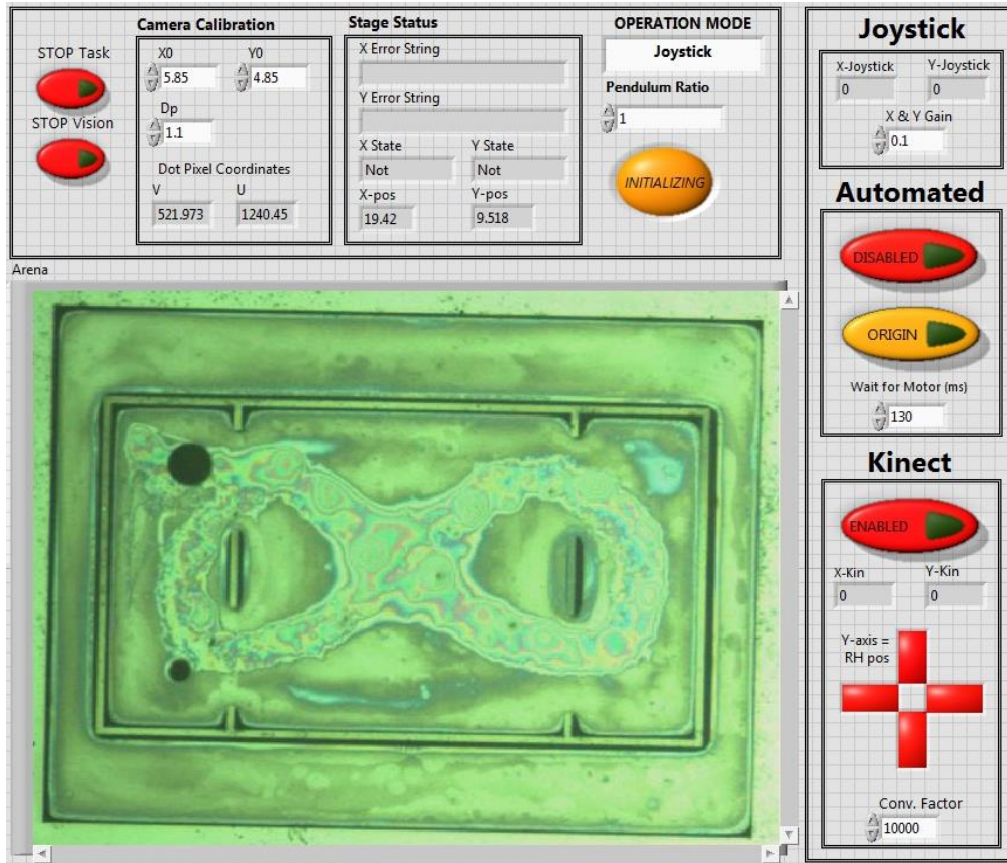


Figure A.3. MMC 2013 LabVIEW Interface

A.3 MMC 2014 Requirements

The MMC 2014 Autonomous Mobility Challenge required an arena measuring 3.1 mm x 2.2 mm with obstacles in the center creating a series of gates (Figure A.4a). The microrobot had to pass through a random sequence of gates given to the participant team at the time of trial (Figure A.4b). The event consisted of three trials with three different sequences. The microrobot's score for the event combined the total time to navigate all three paths and the

dimension of the microrobot to encourage teams to minimize the size of their microrobot. The microassembly challenge remained the same as in MMC 2013.

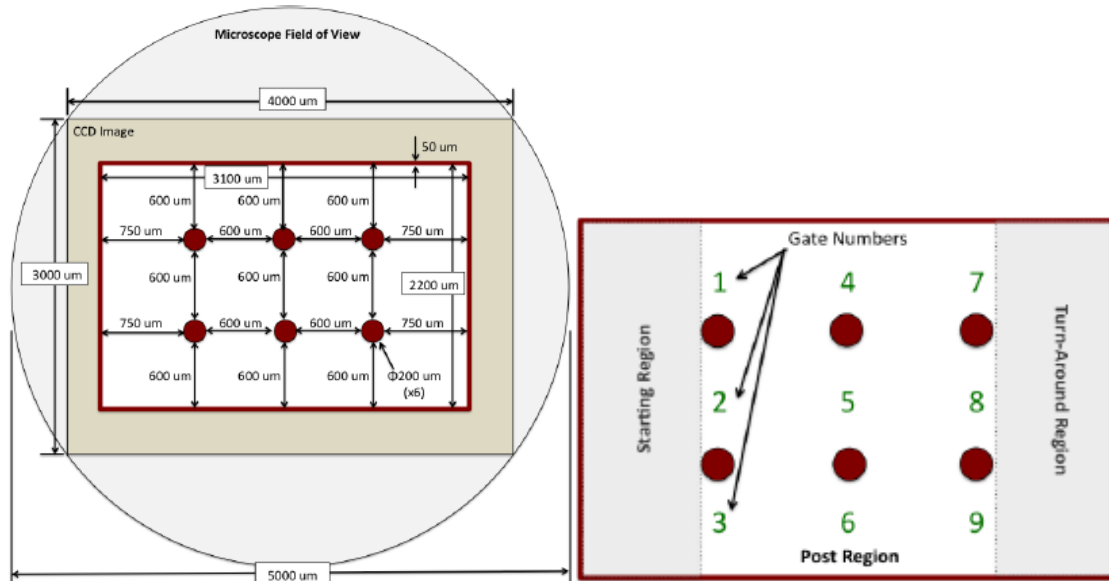


Figure A.4. Autonomous mobility challenge arena a) dimensions and b) gate description

A.3.1 LabVIEW Interface

The random path sequence simulation is illustrated in Figure A.5 showing the path taken going forward and the returning path. Figure A.6 illustrates the interface of Leapmotion sensor to control x-y axis and enable autonomous mobility with hand gestures.

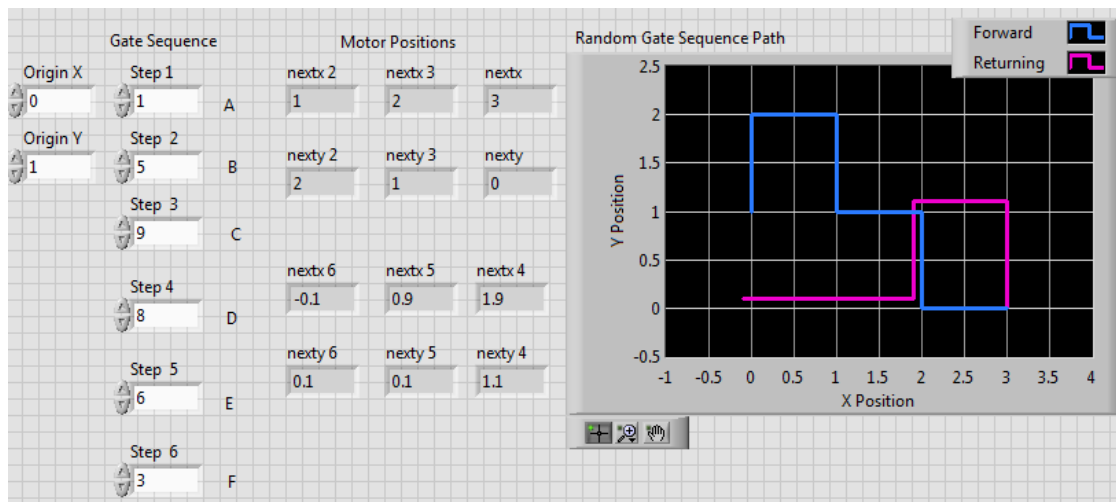


Figure A.5. Autonomous mobility challenge LabVIEW interface

The Microassembly Challenge remained the same as previous years with an additional requirement that the assembly must occur in the far end of the channel and not the sidewalls.

A.4.1 LabVIEW Interface

The shape path planning interface is illustrated in Figure A.8

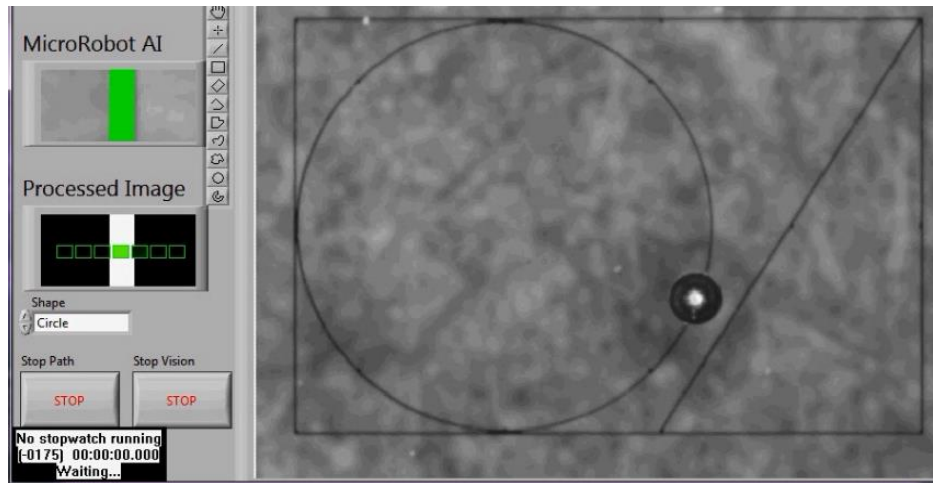


Figure A. 8. MMC 2015 LabVIEW Interface by line scanning method

APPENDIX B
MAGNETIC FIELD ANALYSIS WITH FEMM AND MATLAB

B.1 Introduction

Finite Element Method Magnetics (FEMM) is an analysis toolbox to solve electromagnetics, magneto-statics, linear/nonlinear time harmonic magnetic, linear electrostatic and steady-state heat flow problems on a two axis domain [100]. It is an open source software that can also be interfaced with MATLAB® to perform recursive calculations.

B.2 Modeling Process within FEMM

The software manual specifies all necessary steps that the user needs to know as well as practical examples and sample files developed by other users. To begin the modeling the magnetic field effect, the materials have to be drawn to scale, then the material properties are assigned and saved as a .FEM file. Figure B.1 depicts an example of a one inch conical magnet used to control a 250 μm spherical microrobot over a glass slide used as the workspace.

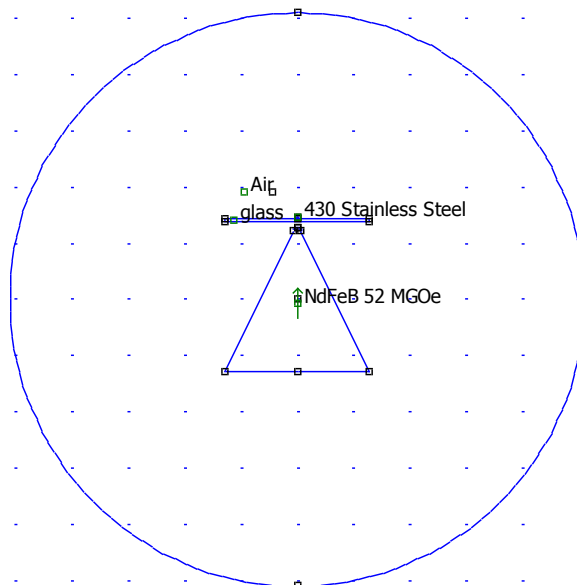

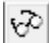



Figure B.1. FEMM Model of conical magnet and spherical microrobot

Once all the components have been drawn. The model, run the simulation by clicking the run button, . Once the software stops running, click the answer button, . The answer toolbar allows you to see the type of results that are needed by the user. In this thesis, I am interested in the magnetic field gradient and density, therefore I click on the gradient field button,  and select, show density plot and legend to display the results as shown in Figure B.2 which indicates the magnetic field density values.

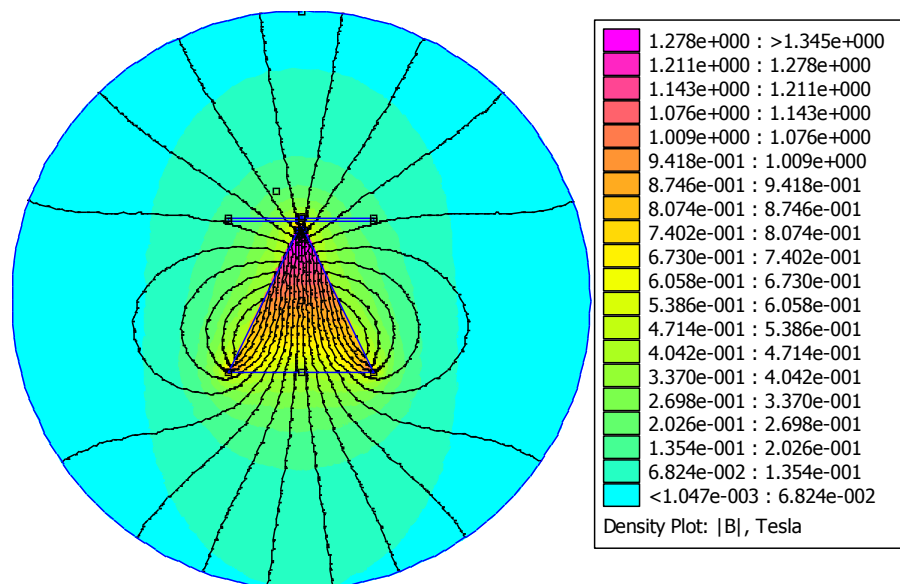




Figure B.2. FEMM Answer file .ans of magnetic field density of the conical magnet

In order to determine the force experienced by the microrobot, the user needs to zoom into the area of interest (Figure B.3 a), click the analysis button, , select the area of the object and it will turn green (Figure B.3 b). Select the integral button, , to select the Force vi Stress Tensor from the drop down menu. The result provides the force experienced by the microrobot with x and y components (Figure B.3 c).

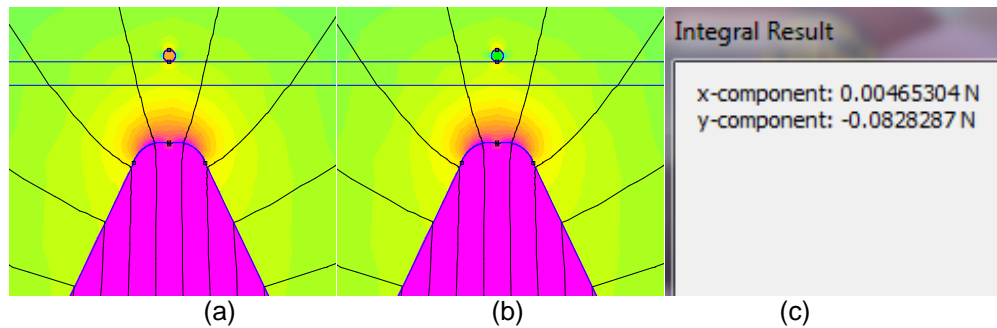


Figure B.3 FEMM Force analysis of a 250 μm spherical microrobot

B.3 Dynamic model MATLAB/FEMM

In order to develop a dynamic model of microrobots, a state space model was formed to solve for the position and velocity of the microrobot in time with respect to the force experienced at each interval. Similar to previous section, the MATLAB script is written to follow the sequence: draw, analyze, extract force, read force into the dynamic equation, solve for new position and new velocity of microrobot and the process is repeated over a number of samples or iterations desired. However, some modifications may be helpful:

1. Draw the initial FEMM file and open it in MATLAB.
2. Once open in MATLAB, draw the microrobots in their initial position, in this case is 3 mm from the tip of the conical magnet.
3. Save as new file in a temporary folder and use such file for analysis.

Moreover, using the appropriate commands, the user can feed back the information to MATLAB and generate plots of the desired information. Figure B.4 illustrates the position of the microrobots L and R per iteration/sample and Figure B.5 illustrates the force experienced by the microrobots during the motion.

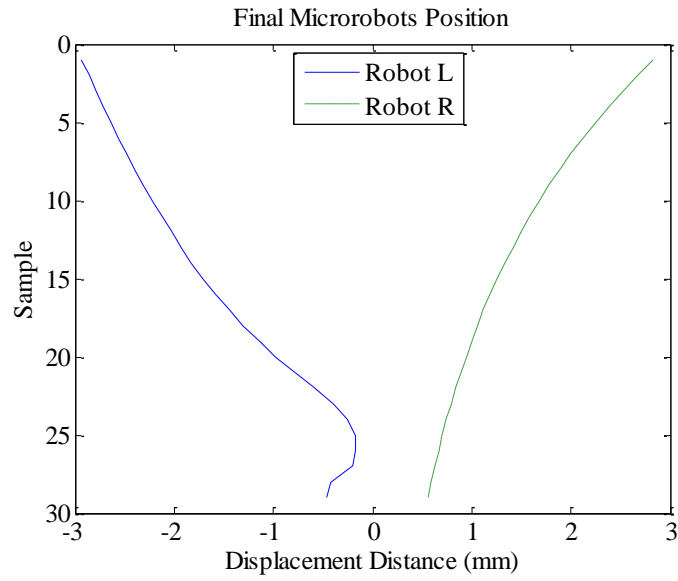


Figure B.4 Microrobots' position per sample

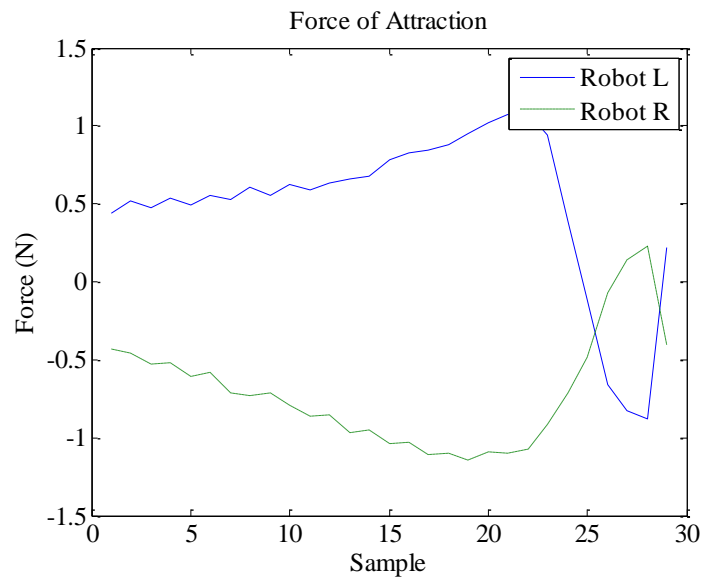


Figure B.5 Force of attraction experienced by the microrobots in the x-axis

B.4 MATLAB Code for Dynamic Model

Table B.1 contains the MATLAB scrip that I developed to interact with FEMM for the dynamic analysis of two 500 μm cubical microrobots. The FEMM commands are explained in the FEMM user's manual found in [100].

Table B.1 MATLAB script developed to interact with FEMM

```
% Nahum A. Torres
% Matlab/Femm interface
% Dynamic model of microrobots

clear all; close all;

% addpath('C:\Users\ntorres\Documents\MATLAB\mfiles')
openfemm;

% The file to open needs to be in the current folder of Matlab
% C:\Program Files\MATLAB\R2011a\bin
opendocument('cone_magnet_slide.FEM'); %Opens a file made in
FEMM

% Microrobot dimensions
w = 0.5; % width
px = w/2; % position of bottom left corner in x-axis
py = 13.6; % position of bottom left corner in y-axis
frc = 0.3; % friction coefficient of cube
frs = 0.03; % friction coefficient of sphere
i=0; % counter index for Force arrays Fx & Fy
xl0 = -3; xr0 = 3; % Init. x pos. of microrobots xl0 left, xr0
right
vl0 = 0; vr0 = 0; % Initial velocities
t=zeros(16,20);
samples=29;

for n=1:1:samples;
i=i+1;
% robot position
RobL(i)=xl0; RobR(i)=xr0;

%Draw a rectangle for the small magnets;
mi_drawrectangle([(xl0-px) py; (xl0+px) py+w]); %left side
mi_drawrectangle([(xr0-px) py; (xr0+px) py+w]); %right side

% Add block labels to magnets
mi_addblocklabel(xl0, py+0.25); % Left Small Magnet
mi_addblocklabel(xr0, py+0.25); % Right Small Magnet
```

```

% Apply the materials to the appropriate block labels
mi_selectlabel(xl0, py+0.25); % Left
mi_selectlabel(xr0, py+0.25); % Right
mi_setblockprop('NdFeB 52 MGOe', 0, 1, '<None>', 90, 0, 0);

% We have to give the geometry a name before we can analyze it.
mi_saveas('C:\\femm42\\temp\\dyn_cone_two_robots.FEM'); %Saves new
file

% Analyze and load the solution when the analysis is finished
mi_analyze;
mi_loadsolution;

% Analyze output file
mo_zoom(-10,7,10,20);

mo_seteditmode('area'); % solution analysis mode
mo_selectblock(xl0,py+0.1); % selects left microrobot area
Fxl(i) = mo_blockintegral(18); % returns Fxl stress tensor
Fyl(i) = mo_blockintegral(19); % returns Fyl stress tensor
mo_clearblock;

mo_selectblock(xr0,py+0.1); % selects right microrobot
area
Fxr(i) = mo_blockintegral(18); % returns Fxl stress tensor
Fyr(i) = mo_blockintegral(19); % returns Fyl stress tensor
mo_clearblock;

% Selects previous label and block to delete & create a
different pose
% Robot on the Left
mi_selectnode(xl0-px,py);mi_selectnode(xl0+px,py);% bottom L|R
nodes
mi_selectnode(xl0-px,py+w); mi_selectnode(xl0+px,py+w);% Top L|R
nodes
% Robot on the Right
mi_selectnode(xr0-px,py);mi_selectnode(xr0+px,py);% bottom L|R
nodes
mi_selectnode(xr0-px,py+w); mi_selectnode(xr0+px,py+w);% Top L|R
nodes

mi_deleteselectednodes
mi_clearselected

mi_selectlabel(xl0, py+0.25); % Material label Left
mi_selectlabel(xr0, py+0.25); % Material label Right
mi_deleteselectedlabels

```

```

% Dynamic code -----

Fxlt = Fxl(i)+sign(vl0)*abs(frc*Fyl(i)); % L Total force in x-
direction
Fxrt = Fxr(i)+sign(vr0)*abs(frc*Fyr(i)); % L Total force in x-
direction

IC = [xl0,vl0,Fxlt,xr0,vr0,Fxrt];% Init. Cond. [pos in mm, vel,
F]
[T,X]=ode23(@Magdyn_two_robots,[0,0.058],IC);% Dynamic solution

ind=length(X(:,2)); % finds the length of the column generated
by ode
xl0=X(ind,1);  xr0=X(ind,4);    % New position from dynamic model
vl0=X(ind,2);  vr0=X(ind,5);    % new initial velocity

% robot position
RobL(i)=xl0; RobR(i)=xr0;
end
mo_showdensityplot(0, 0, 1.5, 0, 'bmag'); % shows color as
density

set(gca,'fontsize', 14);
set(0,'DefaultAxesFontName', 'Times New Roman');
i=1:1:samples;
axis([0 30 -4 4]);
plot(i,RobL,'-',i,RobR,'--')% plots the state space solution
legend('Robot L','Robot R');
title('Final Microrobots Position');
xlabel('Sample');
ylabel('Displacement Distance (mm)');

figure(2)
set(gca,'fontsize', 14);
set(0,'DefaultAxesFontName', 'Times New Roman');
plot(i,Fyl,i,Fyr)% Perpendicular force or robots
legend('Robot L','Robot R');
title('Force of Attraction');
xlabel('Sample');
ylabel('Force (N)');

```

APPENDIX C
SPATIAL UNCERTAINTY ESTIMATION LabVIEW INTERFACE

C.1 Block Diagram

The modular robot spatial uncertainty estimation tool was developed in the following sequence under the main VI labeled as “Modular Robot Analysis Unc Main.vi” in the LabVIEW project labeled “Modular Robot Analysis.lvproj” (Figure C.1).

1. Global variables: These variables are used throughout the main VI and their size adjust automatically to match the number of modules used to build your robot.
2. Robot Configuration
 - a. The “determine joint order.vi” reads the user input of characters and uses x,y,z to select prismatic joints in their respective axis and t, b, g, to select revolute joints in x, y, z axis respectively. The VI handles lower case or upper case characters.
 - b. The “joint parameters extraction_6DOF.vi” extracts the specifications of each module from a spreadsheet (.csv file) that the user must provide.
 - c. The “joint translation.vi” is interactive with the user and asks the user to enter the translation and offset for each module in the order in which the “Robot Configuration” string was entered.
3. Create Uncertainty data
 - a. The “Modular gen rand uncertainty_100pts.vi” generates 100 points of uncertainties for each module of the robot. The uncertainties can be generated with each iteration if desired but its may not be necessary, hence the on/off button in the front panel.
4. Draw Robot
 - a. The “Modular draw robot configuration.vi” displays the modular robot created with 3D images of boxes for prismatic joints and cylinders for

revolute joints. The size of these objects is extracted from the specification file.

5. Robot Transformation

- a. The “Modular Robot POE Transformation.vi” uses screw theory and POE to determine the robot’s transformation

6. Data Analysis

- a. Accuracy and repeatability are computed and illustrated in 3D plots

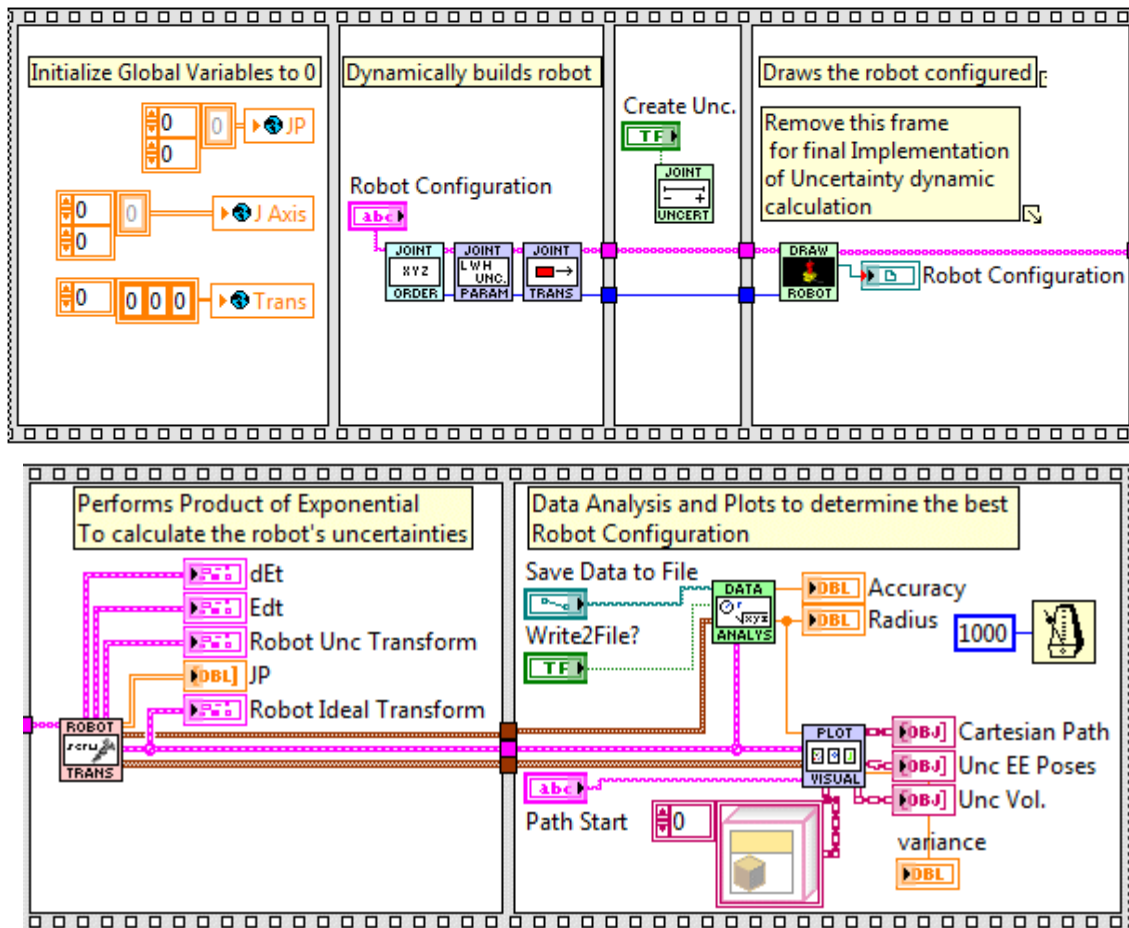


Figure C.1. Main VI block diagram for modular robot analysis

C.2 Front Panel

The front panel is interactive with the user and allows to see several aspects of the robot analysis such as the modular robot, the uncertainty points generated, the Cartesian path taken by the robot and the accuracy and repeatability results as well as instructions (Figure C.2).

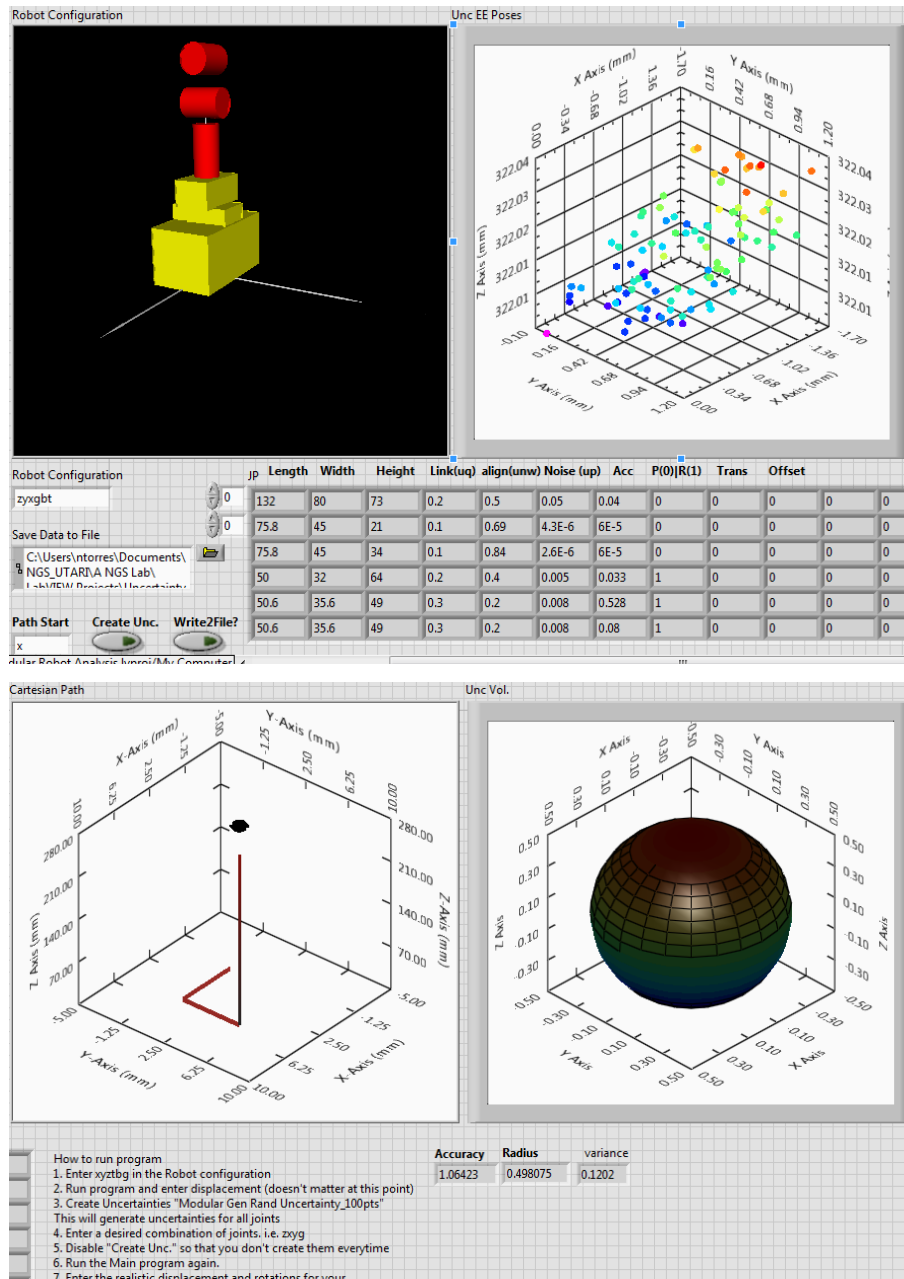


Figure C. 2. Main VI front panel for modular robot analysis

References

- [1] J. Edd et al., "Biomimetic propulsion for a swimming surgical micro-robot," in *IEEE/RSJ Conference on Intelligent Robots and Systems*, IROS. 2003, pp. 2583-2588.
- [2] D. Oleynikov et al., "Microrobot for surgical applications," U.S. Patent No. 7,042,184, May 9, 2006.
- [3] M. P. Kummer et al., "OctoMag: An electromagnetic system for 5-DOF wireless micromanipulation," *IEEE Trans. on Robotics*, vol. 26, no. 6, pp. 1006-1017, Dec. 2010.
- [4] R. Murthy and D. O. Popa, "Millimeter-scale microrobots for wafer-level factories," in *IEEE Int. Conference on Robotics and Automation*, ICRA. 2010, pp. 488-493.
- [5] T. Inoue et al., "Micromanipulation Using Magnetic Field," in *IEEE Int. Conference on Robotics and Automation*, ICRA. 1995, pp. 679 - 684.
- [6] T. Kawahara et al., "On-Chip Microrobot for Investigation of Stimulant Property of Aquatic Microorganisms," in *IEEE Int. Symposium on Micro-NanoMechatronics and Human Science*, MHS. 2013, pp. 1-3.
- [7] S. N. Tabatabaei et al., "Towards MR-navigable Nanorobotic Carriers for Drug Delivery into the Brain," in *IEEE Int. Conference on Robotics and Automation*, ICRA. 2012, pp. 727-732.
- [8] F. Afkhami et al., "Encapsulation of Magnetotactic Bacteria for Targeted and Controlled Delivery of Anticancer Agents for Tumor Therapy," in *IEEE Annual Int. Conference of Engineering in Medicine and Biology Society*, EMBC. 2011, pp. 6668-6671.
- [9] Z. Ye and M. Sitti, "Dynamic Trapping and Two-Dimensional Transport of Swimming Microorganisms Using a Rotating Magnetic Micro-Robot," *Lab on a Chip*, vol. 14, no. 13, pp. 2177-2182, Jul. 2014.
- [10] T. Fukuda, T. Niimi and G. Obinata, *Micro-Nano Mechatronics - new Trends in Material, Measurement, Control, Manufacturing and Their Applications in Biomedical Engineering*. Rijeka : InTech., 2013.
- [11] H. Chen and D. Sun, "Moving Groups of Microparticles into Array with a Robot-Tweezers Manipulation System," *IEEE Trans. on Robotics*, vol. 28, no. 5, pp. 2069-1080, Oct. 2012.
- [12] H. Chen and D. Sun, "Pairing and Moving Swarm of Micro Particles into Array with a Robot-Tweezer manipulation System," in *IEEE/RSJ Int. Conference on Intelligent Robots and Systems*, IROS. 2011, pp. 451 - 456.
- [13] A. G. Banerjee et al., "Real-Time Path Planning for Coordinated Transport of Multiple Particles Using Optical Tweezers," *IEEE Trans. on*

- Automation Science and Engineering*, vol. 9, no. 4, pp. 669-678, Oct. 2012.
- [14] W. Hu, K. S. Ishii and A. T. Ohta, "Micro-assembly using optically controlled bubble microrobots," *Applied Physics Letters*, vol. 99, no. 9, 2011.
 - [15] G. Hwang and et al., "Mobile Microrobotic manipulator in microfluidics," *Sensors and Actuators A: Physical*, vol. 215, pp. 56-64, 2014.
 - [16] E. Diller et al., "Control of Multiple Heterogeneous Magnetic Microrobots in Two Dimensions on Nonspecialized Surfaces," *IEEE Trans. on Robotics*, vol. 28, no. 1, pp. 172-182, Feb. 2012.
 - [17] C. Pawashe, S. Floyd and M. Sitti, "Multiple magnetic microrobot control using electrostatic anchoring," *Applied Physics Letters*, vol. 94, no. 16, 164108, 2009.
 - [18] J. Kim and S.-J. Kim, "A Novel Two-dimensional Locomotion Scheme of a Micro-robot with Only a Uniform Magnetic Field," in *IEEE Int. Conference on Robotics and Automation, ICRA*. 2014, pp. 2071-2076.
 - [19] J. Giltinan et al., "Three-Dimensional Robotic Manipulation and Transport of Micro-Scale Objects by a Magnetically Driven Capillary Micro-Gripper," in *IEEE Int. Conference on Robotics and Automation, ICRA*. 2014, pp. 2077-2082.
 - [20] S. Floyd, C. Pawashe and M. Sitti, "An Untethered Magnetically Actuated Micro-Robot Capable of Motion on Arbitrary Surfaces," in *IEEE Int. Conference on Robotics and Automation, ICRA*. 2008, pp. 419-424.
 - [21] W. Jing et al., "A Magnetic Thin Film Microrobot with Two Operating Modes," in *IEEE Int. Conference on Robotics and Automation, ICRA*. 2011, pp. 96-101.
 - [22] N. A. Torres, S. Ruggeri and D. O. Popa, "Untethered Microrobots Actuated with Focused Permanent Magnet Field," in *ASME 2014 Int. Conference Design Engineering Technical Conferences and Computers and Information in Engineering Conference, DETC/CIE*. 2014, pp. V004T09A024.
 - [23] A. Ichikawa et al., "Untethered Micro-Robot with Gripping Mechanism for On-Chip Cell Surgery Utilizing Outer Magnetic Force," in *IEEE Int. Conference on Robotics and Automation, ICRA*. 2014, pp. 3795-3800.
 - [24] M. Takeuchi et al., "Handling of micro objects using phase transition of thermoresponsive polymer," *J. of Micro-Bio Robotics*, vol. 8, no. 2, pp. 53-64, April 2013.

- [25] D. J. Cappelleri, Z. Fu and M. Fatovic, "Caging for 2D and 3D Micromanipulation," *J. of Micro-Nano Mechatronics*, vol. 7, no. 4, pp. 115-129, Dec. 2012.
- [26] X. Xu, J. Agnus and M. Rakotondrabe, "Development and characterization of a new silicone/platine based 2-DoF sensorized end-effector for micromanipulation," in *SPIE 9116, Next Generation Robots and Systems*, 2014, pp. 911608.
- [27] J. Agnus et al., "Robotic Microassembly and Micromanipulation at FEMTO-ST," *J. of Micro-Bio Robotics*, vol. 8, no. 2, pp. 91-106, Feb. 2013.
- [28] S. Fatikow et al., "Microrobot System for Automatic Nanohandling Inside a Scanning Electron Microscope," *IEEE/ASME Trans. on Mechatronics*, vol. 12, no. 3, pp. 244-252, June 2007.
- [29] M. Boudaoud and S. Regnier, "An Overview on Gripping Force Measurement at the Micro and Nano-scales Using Two-fingered Microrobotic Systems," *Int. J. of Advanced Robotic Systems*, vol. 11, no. 45, Dec. 2014.
- [30] B. Komati, C. Cleve and P. Lutz, "Force Tracking Impedance Control with Unknown Environment at Microscale," in *IEEE Int. Conference on robotics and Automation, ICRA*. 2014.
- [31] M. Sakar et al., "Biosensing and actuation for microbiorobots," in *IEEE Int. Conference on Robotics and Automation, ICRA*. 2010, pp. 3141-3146.
- [32] R. Maboudian, W. R. Ashurst and C. Carraro, "Self-assembled monolayers as anti-stiction coatings for MEMS: characteristics and recent developments," *Sensors and Actuators A: physical*, vol. 82, no. 1-3, pp. 219-223, May 2000.
- [33] Y. Zhuang et al., "Vapor-phase self-assembled monolayers for anti-stiction applications in MEMS," *J. of Microelectromechanical Systems*, vol. 16, no. 6, pp. 1451-1460, Dec. 2007.
- [34] D. S. Thomas, "The Current State and Recent Trends of The U.S. Manufacturing Industry," *NIST Special Publication 1142*, 2012.
- [35] F. L. Lewis, D. M. Dawson and C. T. Abdallah, *Robot Manipulator Control*, New York: Marcel Dekker, 2004.
- [36] E. Diller and S. Metin, "Three-Dimensional Programmable Assembly by Untethered Magnetic Robotic Micro-Grippers," *Advanced Functional Materials*, vol. 24, no. 28, pp. 4397-4404, Apr. 2014.

- [37] B. L. Bayus, "An Analysis of Product Lifetimes in a Technologically Dynamic Industry," *J. of Management Science*, vol. 44, no. 6, pp. 763-775, June 1998.
- [38] A. N. Das, N. A. Torres and D. O. Popa, "A flexible Manufacturing System Architecture for On-Demand, Rate-Independent Production," in *Proc. of the ASME 2015 Int. Mechanical Engineering Congress & Exposition*, IMECE. 2015.
- [39] R. M. Murray, Z. Li and S. S. Sastry, *A Mathematical Introduction to Robotic manipulation*, FL:CRC Press, 1994.
- [40] I.-M. Chen and G. Yang, "Kinematic Calibration of Modular Reconfigurable Robots Using Product-of-Exponentials Formula," *J. of Robotics Systems*, vol. 14, no. 11, pp. 807-821, Nov. 1997.
- [41] DOE, "Additive Manufacturing Technology Assessment (Draft)," 2015.
- [42] M. S. Moses et al., "An Architecture for Universal Construction via Modular Robotic Components," *Robotics and Autonomous Systems*, vol. 62, no. 7, pp. 945-965, July 2014.
- [43] S. Fahlbusch and S. Fatikow, "Force Sensing in Microrobotic Systems - an overview," in *IEEE Int. Conference on Electronics, Circuits and Systems*, ICECS. 1998, pp. 259-262.
- [44] R. S. Fearing, "Survey of Sticking Effects for Micro Parts Handling," in *IEEE/RSJ Int. Conference on Intelligent Robots and Systems*, IROS. 1995, pp. 212-217.
- [45] A. N. Das, D. O. Popa and H. E. Stephanou, "Automated Microassembly with Precision Based Hybrid Control," in *Int. Conference on Robotics and Automation*, ICRA. 2010, pp. 4106-4112.
- [46] N. A. Torres and D. O. Popa, "Cooperative Control of Multiple Untethered Magnetic Microrobots Using a Single Magnetic Field Source," in *IEEE Int. Conference on Automation Science and Engineering*, CASE. 2015, pp.1608-1613.
- [47] R. Alterovitz, M. Branicky and K. Goldberg, "Motion Planning Under Uncertainty for Image-guided Medical Needle Steering," *J. of Robotics Research*, vol. 27, no. 11-12, pp. 1361-1374, Dec. 2008.
- [48] R. C. Smith and P. Cheeseman, "On the Representation and Estimation of Spatial Uncertainty," *The Int. J. of Robotics Research*, vol. 5, no. 4, 1986.
- [49] S.-F. Su and S. G. Lee, "Manipulation and Propagation of Uncertainty and Verification of Applicability of Actions in Assembly Tasks," *IEEE Trans. on Systems, Man and Cybernetics*, vol. 22, no. 6, pp. 1376, 1389, Dec. 1992.

- [50] Y. Wang and G. S. Chirikjian, "Nonparametric Second-order Theory of Error Propagation on Motion Groups," *Int. J. of Robotics Research*, vol. 27, no. 11-12, pp. 1258-1273, 2008.
- [51] Y. Wang and G. S. Chirikjian, "Error Propagation on the Euclidean Group with Applications to Manipulator Kinematics," *IEEE Trans. on Robotics*, vol. 22, no. 4, pp. 591–602, Aug. 2006.
- [52] A. H. Slocum, *Precision Machine Design*, Dearborn, MI: Society of Manufacturing Engineers, 1992.
- [53] C. B. Patil, S. V. Sreenivasan and R. G. Longoria, "Analytical and Experimental Characterization of Parasitic Motion in Flexure-Based Selectively Compliant Precision Mechanisms," in *ASME 2008 Int. Design Engineering Technical Conferences and Computers and Information in Engineering Conference, 32nd Mechanisms and Robotics Conference, DETC/CIE*. 2008, pp. 393-404.
- [54] N. Binaud and et al., "The Kinematic Sensitivity of Robotic Manipulators to Joint Clearances," in *ASME Int. Design Engineering Technical Conferences and Computers and Information in Engineering Conference, DETC/CIE*. 2010, pp. 1371-1380.
- [55] Z. Zhiwei et al, "Characterization of Spatial Parasitic Motions of Compliant Mechanisms Induced by Manufacturing Errors," *J. of Mechanisms and Robotics*, vol. 8, no. 1, pp. 011018, Aug. 2015.
- [56] M. R. Pac and D. O. Popa, "Interval Analysis for Robot Precision Evaluation," in *IEEE Int. Conference on Robotics and Automation, ICRA*. 2012, pp. 1087 - 1092.
- [57] V. Nazari and L. Notash, "Motion Analysis of Manipulators with Uncertainty in Kinematic Parameters," *J. of Mechanisms and Robotics*, vol. 22, pp. 9-17, June 2014.
- [58] H. A. Hagaras, "A Hierarchical Type-2 Fuzzy Logic control Architecture for Autonomous Mobile Robots," *IEEE Trans. on Fuzzy Systems*, vol. 12, no. 4, pp. 524-539, Aug. 2004.
- [59] A. N. Das and D. O. Popa, "Precision-Based Robot Kinematic Design for Microassembly Applications," in *ASME Int. Design Engineering Technical Conferences and Computers and Information in Engineering Conference, DETC/CIE*. 2010, pp. 857-862
- [60] J. Van Den Berg, P. Abbeel and K. Goldberg, "LQG-MP: Optimized Path Planning for Robots with Motion Uncertainty and Imperfect State Information," *The Int. J. of Robotics Research*, vol. 30, no. 7, pp. 895-913, June 2011.

- [61] X. W. Chen and S. Y. Nof, "Error Detection and Prediction Algorithms: Application in Robotics," *J. of Intelligent and Robotic Systems*, vol. 48, no. 2, pp. 225-252, Jan. 2007.
- [62] H. P. Jawale and H. T. Thorat, "Investigation of Positional Error in Two Degree of Freedom Mechanism with Joint Clearance," *J. of Mechanisms and Robotics*, vol. 4, no. 1, pp. 011002-011009, Feb. 2012.
- [63] G. Wu and et al., "Error Modeling and Experimental Validation of a Planar 3-P PR Parallel Manipulator with Joint Clearances," *J. of Mechanisms and Robotics*, vol. 4, no. 4, pp. 041008-041020, 2012.
- [64] D. Corradi et al., "Assembly Conditions of Parallel Manipulators Considering Geometric Errors, Joint Clearances, Link Flexibility and Joint Elasticity," in *IEEE Int. Conference on Robotics and Automation, ICRA*. 2014, pp. 4067-4072.
- [65] D. G. Mikulski et al., "Trust method for multi-agent consensus," in *Proc. of SPIE Conference Series 8387, Unmanned Systems Technology XIV*, 83870E, 2012.
- [66] W. Ren, R. W. Beard and D. B. Kingston, "Multi-agent Kalman consensus with relative uncertainty," in *Proc. of the 2005, American Control Conference, ACC*. 2005, pp. 1865-1870
- [67] S. Tasoglu et al., "Untethered micro-robotic coding of three-dimensional material composition," *Nature Communications*, vol. 5, 3124, Jan. 2014.
- [68] D. Cappelleri et al., "Towards Mobile Microrobot Swarms for Additive Micromanufacturing," *Int. J. of Advanced Robotic Systems*, vol. 11, no. 150, Aug. 2014.
- [69] H. Wang et al., "Micro-assembly of a Vascular-like Micro-channel with Railed Micro-robot Team-coordinated Manipulation," *Int. J. of Advanced Robotic and Systems*, vol. 11, no. 15, June 2014.
- [70] S. Martel and M. Mohammadi, "A Robotic Micro-assembly Process Inspired by the Construction of the Ancient Pyramids and Relying on Several Thousand Flagellated Bacteria Acting as Micro-workers," in *IEEE/RSJ Int. Conference on Intelligent Robots and Systems, IROS*. 2009, pp. 426-427.
- [71] B. E. Kratochvil et al., "OctoMag: An Electromagnetic System for 5-DOF Wireless Micromanipulation," in *IEEE Int. Conference on Robotics and Automation, ICRA*. 2010, pp. 1006-1017.
- [72] C. Pawashe et al., "Two-Dimensional Autonomous Microparticle manipulation Strategies for Magnetic Microrobots in Fluidic Environments," *IEEE Trans. on Robotics*, vol. 28, no. 2, pp. 467-477, April 2012.

- [73] W. Jing and D. J. Cappelleri, "Incorporating in-situ Force Sensing Capabilities in a Magnetic Microrobot," in *IEEE/RSJ Int. Conference on Intelligent Robots and Systems*, IROS. 2014, pp. 4704-4709.
- [74] B. R. Donald et al., "An untethered, electrostatic, globally controllable MEMS micro-robot," *J. of Microelectromechanical Systems*, vol. 15, no. 1, pp. 1-15, Feb. 2006.
- [75] T. M. Shea, "Durable hydrophobic surface coatings using silicone resins," U.S. Patent No. 7,344,783, March 18, 2008.
- [76] M. Newman, (2011, June 7). *NIST Contests in China put Next-Gen Robot Technologies to the test* [online]. Available: <http://www.nist.gov/el/isd/mmc/>
- [77] I. A. Ivan et al., "First Experiment on MagPieR: a Planar Wireless Magnetic and Piezoelectric microrobot," in *IEEE Int. Conference on Robotics and Automation*, ICRA. 2011, pp. 102-108.
- [78] K. Vollmers and et al., "Wireless Resonant Magnetic Microactuator for Untethered Mobile Microrobots," *Applied Physics Letter*, vol. 92, p. 144103, 2008.
- [79] M. R. Pac and D. O. Popa, "3-DOF Untethered Microrobot Powered by a Single laser Beam Based on Differential Thermal Dynamics," in *IEEE Int. Conference on Robotics and Automation*, ICRA. 2011, pp. 121-127.
- [80] S. Chowdhury, W. Jing and D. J. Cappelleri, "Controlling multiple microrobots: recent progress and future challenges," *J. of Micro-Bio Robotics*, vol. 10, no. 1, pp. 1-11, Oct. 2015.
- [81] F. L. Lewis, H. Zhang, K. Hengster-Movric and A. Das, *Cooperative Control of Multi-Agent systems: Optimal and Adaptive Design Approaches*, Springer, 2013.
- [82] J.-M. Breguet et al., "Applications of piezo-actuated micro-robots in micro-biology and material science," in *IEEE Int. Conference on Mechatronics and Automation*, ICRA. 2007, pp. 57-62.
- [83] J. Angus et al., "Robotic Microassembly and Micromanipulation at FEMTO-ST," *J. of Micro-Bio Robotics*, vol. 8, no. 2, pp. 91-106, April 2013.
- [84] S. Fatikow et al., "Microrobot System for Automatic Nanohandling Inside a Scanning Electron Microscope," *IEEE/ASME Trans. on Mechatronics*, vol. 12, no. 3, June 2007.
- [85] D. J. Cappelleri, Z. Fu and M. Fatovic, "Caging for 2D and 3D Micromanipulation," *J. of Micro-Nano Mechatronics*, vol. 7, no. 4, pp. 115-129, Nov. 2012.

- [86] B. Greenway, "Robot accuracy," *Industrial Robot: An Int. J.*, vol. 27, pp. 257-265, 2000.
- [87] P. A. Golden and M. Dollinger, "Cooperative alliances and competitive strategies in small manufacturing firms," *J. of Entrepreneurship: Theory and Practice*, vol. 17, no. 4, pp. 43-57, 1993.
- [88] Z. Huang and S. X. Li, "Co-op advertising models in manufacturer-retailer supply chains: A game theory approach," *European J. of Operational Research*, vol. 3, no. 135, pp. 527-544, Dec. 2001.
- [89] Z. Guan et al., "Application of decentralized cooperative problem solving in dynamic flexible scheduling," in *Int. Conference on Intelligent Manufacturing*, pp. 179-183, Aug. 1995
- [90] W. M. Shen, "Distributed manufacturing scheduling using intelligent agents," in *IEEE Intelligent Systems*, pp. 88-94, Jan/Feb 2002.
- [91] C. Pippin and H. Christensen, "Cooperation based dynamic team formation in multi-agent auctions," in *Proc. SPIE 8389, Ground/Air Multisensor Interoperability, Integration, and Networking for Persistent ISR III, 838919*, May 2012.
- [92] T. Jiang and J. S. Baras, "Graph algebraic interpretation of trust establishment in autonomic networks," *Wiley Journal of Networks*, 2009.
- [93] J. S. Baras and P. Hovareshti, "Effect of graph topology on performance of distributed algorithms for networked control and sensing," in *Workshop on Networked Distributed Systems for Intelligent Sensing and Control*, 2007.
- [94] R. A. Society. (2013, October 2). *IEEE RAS Micro/Nano Robotics & Automation: Mobile Microrobotics Challenge* [online]. Available: <http://www.uta.edu/ee/ngs/mmc/>
- [95] G. Yu and K. G. Kornev, "Attachment/detachment hysteresis of fiber-based magnetic grabbers," *Soft matter*, vol. 10, no. 16, pp. 2816-2824, April 2014.
- [96] D. E. Turcotte et al., "Water repellent glass treatment for automotive applications," U.S. Patent 6,461,537 B1, October 8 2002.
- [97] F. Fontana et al., "Flexible vision based control for micro-factories," in *ASME 2013 Int. Design Engineering Technical Conference and Computers and Information in Engineering Conference, DETC/CIE. 2013*, pp. V001T09A029.
- [98] S. Pak and O. TaeHo, "Correlation and Simple Linear Regressions," *J. of Veterinary Clinics*, vol. 27, no. 4, pp. 427-434, 2010.
- [99] H. Choset and et al, *Principles of robot motion: theory, algorithms, and implementations*, MIT Press, 2005.

- [100] D. C. Meeker. (2014, April 6). *Finite element Method magnetics* (V4.2)[online]. Available: <http://www.femm.info/wiki/HomePage>
- [101] M. P. Groover, *Automation, Production Systems, and Computer-Integrated Manufacturing*, 3rd ed, Prentice Hall Press, 2007.
- [102] C. Mavroidis, C. Pfeiffer and M. Mosley, *Conventional Actuator, Shape Memory Alloys, and Electrorheological Fluids*, Bar-Cohen, 1999.
- [103] M. Lemire, L. Boni and . B. Furnish, "The Straight Story on Linear Actuators," 2007.
- [104] H. Ulbrich, "Comparison of Different Actuator Concepts for Applications in Rotating machinery," *Int. J. of Rotating Machinery*, vol. 1, no. 1, pp. 61-71, 1994.
- [105] A. Parr, *Hydraulics and Pneumatics - A technician's and Engineer's Guide*, Oxford: Butterworth-Heinemann, 2006.
- [106] R.-M. A. Nzue et al., "Comparison of serial and parallel robot repeatability based on different performance criteria," *Mechanism and Machine Theory*, vol. 61, pp. 136-155, March 2013.
- [107] F. L. Lewis, L. Xie and D. O. Popa, *Optimal and Robust Estimation*, Boca Raton: CRC Press, 2008.

Biographical Information

Nahum A. Torres proudly served eight years in the U.S. Army and received his B.S. degree in 2009 and Ph.D. degree in 2016, both in Electrical Engineering from the University of Texas at Arlington (UTA). He served as a teaching assistant in the Electrical Engineering Department from 2010 until 2015. In 2011 he also joined the University of Texas at Arlington Research Institute (UTARI) as a research assistant in the Next Generation Systems group where he worked on multiscale robotics to include Zeno, a robot used for Autism therapy made by RoboKind, Phillip K. Dick and Dmitri Itskov, humanoid robots by Hanson Robotics, DR20, a military grade mobile robot by Quinetiq North America, YouBot, a mobile robot by KUKA, Assembly robots funded by Walmart, and lastly Microrobotics, his thesis work, which his team used to participated in the IEEE Mobile Micro/nano-robotics Challenge (MMC) and placed in the top three places for three consecutive years, 2013-2015. His current interest is to implement his knowledge and leadership skills in national defense projects, healthcare, automated manufacturing, and robotics R&D.